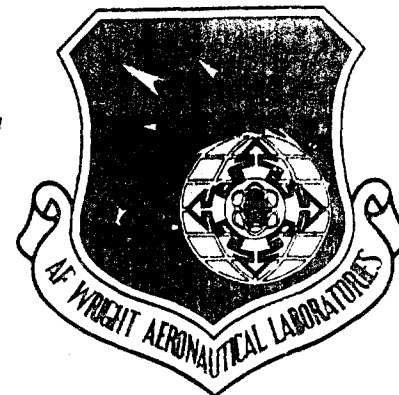


AFWAL-TR-87-4134

DTIC FILE COPY



**A-D-A194 223**

PLASTIC FLOW AND FAILURE MODELING  
UNDER HIGH STRAIN RATE LOADING

A. M. Rajendran  
S. J. Bless

University of Dayton  
Research Institute  
Dayton, Ohio 45469

February 1988

Final Report for period August 1984 - April 1987.

Approved for public release; distribution unlimited

MATERIALS LABORATORY  
AIR FORCE WRIGHT AERONAUTICAL LABORATORIES  
AIR FORCE SYSTEMS COMMAND  
WRIGHT-PATTERSON AIR FORCE BASE, OH 45433

DTIC  
ELECTE  
APR 26 1988  
S H D

88 4 26 052

## NOTICE


When Government drawings, specifications, or other data are used for any purpose other than in connection with a definitely Government-related procurement, the United States Government incurs no responsibility or any obligation whatsoever. The fact that the Government may have formulated or in any way supplied the said drawings, specifications, or other data, is not to be regarded by implication, or otherwise in any manner construed, as licensing the holder, or any other person or corporation; or as conveying any rights or permission to manufacture, use, or sell any patented invention that may in any way be related thereto.

This report has been reviewed by the Office of Public Affairs (ASD/PA) and is releasable to the National Technical Information Service (NTIS). At NTIS, it will be available to the general public, including foreign nations.

This technical report has been reviewed and is approved for publication.

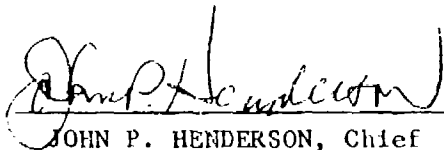


THEODORE NICHOLAS  
Metals Behavior Branch  
Metals and Ceramics Division



ALLAN W. GUNDERSON  
Tech Area Manager  
Metals Behavior Branch  
Metals and Ceramics Division

FOR THE COMMANDER



JOHN P. HENDERSON, Chief  
Metals Behavior Branch  
Metals and Ceramics Division

If your address has changed, if you wish to be removed from our mailing list, or if the addressee is no longer employed by your organization please notify AFWAL/MLLN, Wright-Patterson AFB, OH 45433-6533 to help us maintain a current mailing list.

Copies of this report should not be returned unless return is required by security considerations, contractual obligations, or notice on a specific document.

Unclassified

SECURITY CLASSIFICATION OF THIS PAGE

# REPORT DOCUMENTATION PAGE

|   |  |   |                       |
|---|--|---|-----------------------|
| REPORT SECURITY CLASSIFICATION<br>Unclassified                                      |  | 1b. RESTRICTIVE MARKINGS  |                       |
| SECURITY CLASSIFICATION AUTHORITY   |  | 3. DISTRIBUTION/AVAILABILITY OF REPORT<br>Approved for public release;<br>distribution unlimited                |                       |
| DECLASSIFICATION/DOWNGRADING SCHEDULE   |  | 5. MONITORING ORGANIZATION REPORT NUMBER(S)<br>AFWAL-TR-87-4134   |                       |
| PERFORMING ORGANIZATION REPORT NUMBER(S)<br>JDR-TR-87-71                            |  | 7a. NAME OF MONITORING ORGANIZATION<br>Air Force Wright Aeronautical Laboratories<br>Materials Lab (AFWAL/MLLN) |                       |
| NAME OF PERFORMING ORGANIZATION<br>University of Dayton<br>Research Institute       | 6b. OFFICE SYMBOL<br>(If applicable)       | 7b. ADDRESS (City, State and ZIP Code)<br>Wright-Patterson Air Force Base<br>Ohio 45433-6533                    |                       |
| ADDRESS (City, State and ZIP Code)<br>300 College Park Avenue<br>Dayton, Ohio 45469 |  | 9. PROCUREMENT INSTRUMENT IDENTIFICATION NUMBER<br>F33615-84-C-5045   |                       |
| NAME OF FUNDING/SPONSORING ORGANIZATION   | 8b. OFFICE SYMBOL<br>(If applicable)       | 10. SOURCE OF FUNDING NOS   |                       |
| ADDRESS (City, State and ZIP Code)  |  | PROGRAM ELEMENT NO.<br>62102F   | PROJECT NO.<br>2422   |
| TITLE (Include Security Classification)<br>Plastic Flow and Failure (see reverse)   |  | TASK NO.<br>05  | WORK UNIT NO.<br>04   |
| PERSONAL AUTHOR(S)<br>A.M. Rajendran, S.J. Bless                                    |  |   |                       |
| 1. TYPE OF REPORT<br>Final  | 13b. TIME COVERED<br>FROM AUG 84 TO APR 87 | 14. DATE OF REPORT (Yr., Mo., Day)<br>February 1988   | 15. PAGE COUNT<br>134 |
| 2. SUPPLEMENTARY NOTATION   |  |   |                       |

| COSATI CODES |       |          | 18. SUBJECT TERMS (Continue on reverse if necessary and identify by block number)<br>strain rate, spall, Hopkinson bar, impact response, shock waves, Bodner-Partom model, dynamic failure, plastic flow |
|--------------|-------|----------|--|
| FIELD        | GROUP | SUB. GR. |  |
| 20           | 11    |          |  |
| 20           | 14    |          |  |

1. ABSTRACT (Continue on reverse if necessary and identify by block number)

High strain rate properties were determined for several metals at room and high temperatures. Split Hopkinson bar (SHB) tests under both tension and compression were performed for obtaining stress-strain curves at different strain rates. Quasi-static tests were also conducted and were compared with the SHB test results. High speed photographs of the necking process in tensile SHB samples were taken and the stress-strain curves beyond necking for 1020 and HY 100 steels, and 6061-T6 aluminum were determined. Technique to heat SHB tensile samples using an induction coil technique was successfully developed. An experimental configuration in which a flyer plate impacts a long rod was used to determine the initial yield stress for three steels. Manganin gage stress measurement technique was used in this experiment. Plate impact tests were also conducted to determine precursor decay, steady state

(see reverse)

|   |  |  |                                  |
|---|--|--|----------------------------------|
| 9. DISTRIBUTION/AVAILABILITY OF ABSTRACT<br>UNCLASSIFIED/UNLIMITED <input checked="" type="checkbox"/> SAME AS RPT <input type="checkbox"/> DTIC USERS <input type="checkbox"/> |  | 21. ABSTRACT SECURITY CLASSIFICATION<br>Unclassified           |                                  |
| 12a. NAME OF RESPONSIBLE INDIVIDUAL<br>Theodore Nicholas  |  | 22b. TELEPHONE NUMBER<br>(Include Area Code)<br>(513) 255-2689 | 22c. OFFICE SYMBOL<br>AFWAL/MLLN |

Unclassified

URITY CLASSIFICATION OF THIS PAGE

11. (continued)

Modeling Under High Strain Rate Loading

19. (continued)

value for HEL, and spall strength. It was also demonstrated that the use of the manganin gage can be extended to determine transverse stresses in a plate impact test. A methodology to determine shock velocity at very high pressures using manganin gages is also presented.

Under the analytical modeling efforts, data from the various experimental configurations were used to calibrate the Bodner-Partom viscoplastic constitutive model parameters. Model parameters for several metals were successfully determined. A void nucleation and growth based dynamic failure model for ductile metals was formulated and model parameters were determined for a steel and copper.



|                    |                                     |
|--------------------|-------------------------------------|
| Accession For      |                                     |
| NTIS GRA&I         | <input checked="" type="checkbox"/> |
| DTIC TAB           | <input type="checkbox"/>            |
| Unannounced        | <input type="checkbox"/>            |
| Justification      |                                     |
| By                 |                                     |
| Distribution/      |                                     |
| Availability Codes |                                     |
| Dist               | Avail and/or<br>Special             |
| A-1                |                                     |

## PREFACE

This work was conducted under Contract No. F33615-84-C-5045 for AFWAL/MLLN. The contract monitor was Dr. Theodore Nicholas. His many helpful comments and his contribution to the precursor decay analysis during the execution of the program were greatly appreciated. Mr. William Cook of AFATL/MNW supplied partial funding for dynamic failure model development. His encouragements and helpful comments were greatly appreciated. Dr. Datta Dandekar of AMTL/Watertown supplied partial funding and technical guidance for investigation of W-2 tungsten, 1215 steel, and 5083-0 aluminum. Mr. George Roth, Supervisor, Experimental and Applied Mechanics Division, served as the Project Manager. His many helpful comments and directions were greatly appreciated.

The principal investigators of this contract were Dr. A. M. Rajendran, Research Engineer in Structural Integrity Division and Dr. S. J. Bless, Senior Research Physicist in Experimental and Applied Mechanics Division. Success of this program would not have been possible without the participation of many additional staff members of both divisions.

Mr. Grove developed the special purpose routines to describe dynamic failure model in STEALTH. Dr. Rosenberg conducted the long rod and plate impact experiments. He also developed the induction coil technique for the split Hopkinson bar and the manganin gage technique for the plate and long rod experiments. The work performed by Dr. Rosenberg under this contract is reported in Section 2.5. This section contains the concise version of many of Dr. Zvi Rosenberg's publications. Ms. Glaser, an undergraduate student, conducted the split Hopkinson bar tests. Mr. Geers performed the OFHC copper modeling. Several improvements in the expanding ring experiments were made by the visiting consultant, Dr. Gideon Rosenberg. Dr. N. S. Brar conducted a few plate impact tests on C1008 steel and 1215 steel.

Ms. Joanda D'Antuono was responsible for the typing of the manuscripts and her efforts are greatly appreciated.

# TABLE OF CONTENTS

| <u>SECTION</u> |  | <u>PAGE</u> |
|----------------|--|-------------|
| I              | INTRODUCTION                             | 1           |
| II             | EXPERIMENTS                              | 2           |
| 2.1            | SPLIT HOPKINSON BAR                      | 2           |
| 2.1.1          | <u>Basic Configuration</u>               | 2           |
| 2.1.2          | <u>High Speed Photographic Technique</u> | 4           |
| 2.1.3          | <u>Induction Coil Heating Technique</u>  | 4           |
| 2.1.4          | <u>Results</u>                           | 8           |
|                | a. <u>Armco Iron</u>                     | 8           |
|                | b. <u>Nickel 200</u>                     | 8           |
|                | c. <u>W-2 Tungsten</u>                   | 18          |
|                | d. <u>C1008 Steel</u>                    | 18          |
|                | e. <u>6061-T6 Aluminum</u>               | 18          |
|                | f. <u>Additional Results</u>             | 22          |
| 2.2            | LONG ROD IMPACT EXPERIMENTS              | 24          |
| 2.2.1          | <u>Technique</u>                         | 24          |
| 2.2.2          | <u>Results</u>                           | 33          |
| 2.2.3          | <u>Gage-Signal Analysis</u>              | 35          |
| 2.3            | EXPANDING RING EXPERIMENTS               | 38          |
| 2.4            | PLATE IMPACT EXPERIMENTS                 | 39          |
| 2.4.1          | <u>Results</u>                           | 41          |
| 2.5            | NEW EXPERIMENTAL TECHNIQUES              | 41          |
| 2.5.1          | <u>Manganin Gauge Technique</u>          | 43          |
| 2.5.2          | <u>Transverse Gauge Technique</u>        | 47          |
| 2.5.3          | <u>High Pressure Measurements</u>        | 51          |
| 2.5.4          | <u>Shear Wave Measurements</u>           | 57          |
| III            | ANAYTICAL MODELING                       | 64          |
| 3.1            | BODNER-PARTOM MODEL                      | 64          |
| 3.2            | IMPLEMENTATION INTO STEALTH CODE         | 67          |
| 3.3            | ESTIMATION OF B-P PARAMETERS             | 67          |
| 3.4            | BODNER MODEL FOR DIRECTIONAL HARDENING   | 68          |
| 3.5            | MODEL PARAMETERS                         | 69          |
| 3.5.1          | <u>Improved Model for OFHC Copper</u>    | 71          |
| 3.6            | PRECURSOR DECAY ANALYSIS                 | 91          |

# TABLE OF CONTENTS (concluded)

| <u>SECTION</u>  | <u>PAGE</u> |
|---|-------------|
| IV DYNAMIC FAILURE MODEL                              | 95          |
| 4.1 MODEL FORMULATION                                 | 97          |
| 4.1.1 <u>Phase I - Modeling of Matrix Material</u>    | 97          |
| 4.1.2 <u>Phase II - Modeling of Aggregate</u>         | 98          |
| 4.1.3 <u>PHASE III - Nucleation and Growth Models</u> | 100         |
| 4.2 ANALYSES  | 102         |
| V CONCLUSIONS   | 115         |
| 5.1 SUMMARY   | 115         |
| 5.2 RECOMMENDATIONS                                   | 116         |
| 5.2.1 <u>Experiments</u>                              | 116         |
| 5.2.2 <u>Modeling</u>                                 | 116         |
| REFERENCES  | 117         |

# LIST OF ILLUSTRATIONS

| <u>FIGURE</u> |  | <u>PAGE</u> |
|---------------|--|-------------|
| 1             | Schematic Sketch of the SHB Setup.   | 3           |
| 2             | Schematic Diagram of the Induction Coil Heating Technique Used in SHB.   | 6           |
| 3             | Variation of Flow Stress at $\epsilon = 0.1$ Against Temperature for Different Metals from Tension Split Hopkinson Bar Tests.  | 9           |
| 4             | True Stress vs. Log $\dot{\epsilon}$ Plot for Armco Iron at Different Strain Levels.   | 14          |
| 5             | True Stress vs. True Strain Data from Quasi-Static and SHB Tests for Armco Iron.   | 15          |
| 6             | True Stress vs. True Strain Plots for Nickel 200 at Room Temperature under Quasi-static ( $\dot{\epsilon} = 0.001$ and $1s^{-1}$ ) and SHB ( $\dot{\epsilon} = 800$ and $1100s^{-1}$ ) Levels. | 16          |
| 7             | True Stress vs. True Strain Plots at Elevated Temperatures for Nickel 200.   | 17          |
| 8a            | Quasi-static Test Results for W-2 Tungsten.  | 19          |
| 8b            | SHB Tension Test Data at $\dot{\epsilon} = 925 s^{-1}$ for W-2 Tungsten.   | 20          |
| 9             | True Stress-True Strain Plots at Elevated Temperatures for (a) 6061-T6 Aluminum, (b) Nickel 200, (c) W-2 Tungsten, and (d) C1008 Steel.  | 21          |
| 10            | True Stress-True Strain Plots Obtained from High Speed Photographs of Necking Specimens.   | 23          |
| 11            | True Stress-True Strain Plots for Vanadium Under Compression.  | 25          |
| 12            | True Stress-True Strain Plots for 52125 Steel Under Tension.   | 26          |
| 13            | True Stress-True Strain Plots for Maraging Steel (a) Mar-M 200; (b) Mar-M 300.   | 28          |
| 14            | True Stress-True Strain Plots for 1044 Steel under Tension Rolling Direction.  | 29          |



# LIST OF ILLUSTRATIONS (continued)

| <u>FIGURE</u> |  | <u>PAGE</u> |
|---------------|--|-------------|
| 15            | True Stress-True Strain Plots for Pure Tantalum Under Tension.   | 30          |
| 16            | True Stress-True Strain Plots for Cast 4140 Steel at $\epsilon = 1200s$ .                                  | 31          |
| 17            | A Schematic Diagram of Long Rod Experiment.  | 32          |
| 18            | A Typical Stress Gauge Record from a Long Rod Experiment.  | 34          |
| 19            | Lagrangian x-t Diagram for the Long Rod Experiment.  | 37          |
| 20            | A Sample Streak Record From An Expanding Ring Experiment.  | 40          |
| 21            | The Principal Axes for a Longitudinal Stress Gauge.  | 45          |
| 22            | The Principal Stresses for a Transverse Stress Gauge.  | 48          |
| 23            | Schematic Representation of the Impact Configuration.  | 53          |
| 24            | Linear Extrapolation to Find the Catch-up Distance.  | 55          |
| 25            | A Schematic Representation of an Oblique-Impact Experiment with a Piezoresistance Gage.                    | 58          |
| 26            | Manganin Gage Record from the Oblique-Impact Experiment.   | 62          |
| 27            | Comparisons of B-P Model Simulations with SHB Room and High Temperature Tests Results for C1008 Steel.     | 72          |
| 28            | Comparison of B-P Model Simulation with Plate Impact VISAR Data for C1008 Steel.                           | 74          |
| 29            | Comparison of B-P Model Simulations with SHB Room and High Temperature Tests Results for 6061-T6 Aluminum. | 75          |
| 30            | Comparison of Quasi-static Tensile Test Results with B-P Model Simulations for W-2 Tungsten.               | 76          |
| 31            | Comparison of B-P Model Simulations with SHB Room and High Temperature Test Results for W-2 Tungsten.      | 77          |

# LIST OF ILLUSTRATIONS (continued)

| <u>FIGURE</u> |  | <u>PAGE</u> |
|---------------|--|-------------|
| 32            | Comparison of B-P Model Simulation with Manganin Gauge Stress History in PMMA W-2 Tungsten.                            | 79          |
| 33            | Comparison of B-P Model Simulations with SHB Tension Test Data for Nickel.   | 80          |
| 34            | Comparison of B-P Model Simulations with SHB Tensile Tests Data for Armco Iron.  | 81          |
| 35            | Comparison of B-P Model Simulations with Plate Impact Test Plot for Armco Iron.  | 83          |
| 36            | Comparison of B-P Model Simulation with SHB Test Data for OFHC Copper.   | 84          |
| 37            | Comparison Between B-P Model, New Bodner Model, and SHB Test Data for OFHC Copper at $\dot{\epsilon}=875s^{-1}$ .      | 85          |
| 38            | Comparison Between B-P Model, New Bodner Model, and SHB Test Data for OFHC Copper at $\dot{\epsilon}=1100s^{-1}$ .     | 86          |
| 39            | Comparison Between B-P Model, New Bodner Model, and SHB Test Data for OFHC Copper at $\dot{\epsilon}=1300s^{-1}$ .     | 87          |
| 40            | Comparison of Modified B-P Model (Effective Plastic Strain Rate Based) with SHB Test Data for OFHC Copper.             | 89          |
| 41            | Comparison Between Effective Plastic Strain Rate Based Model and Plastic Work Based B-P Model.                         | 90          |
| 42            | Precursor Decay along the Target Thickness Using $\epsilon_{eff}$ Criterion.   | 93          |
| 43            | Comparison of the Experimental Data with the Model Prediction.   | 94          |
| 44            | STEALTH Simulation of Test # 678 (a) Velocity vs. Time at the Free Surface and (b) Stress vs. Time at the Spall Plane. | 104         |
| 45            | Effect of the Parameter B on the Yield Surfaces.   | 106         |
| 46            | A Typical Spall Signal.  | 107         |

LIST OF ILLUSTRATIONS (concluded)

| <u>FIGURE</u> |   | <u>PAGE</u> |
|---------------|---|-------------|
| 47            | Simulation of Test # 678 C1008 Steel Using the Failure Model with New Function for $\delta(\rho)$ . | 109         |
| 48            | Comparison of Model Simulation with the Experimental Velocity vs. Time Plot for OFHC Copper.        | 110         |
| 49            | Calculated Stress History at the Spall Plane for Different Impact Velocities.                       | 112         |
| 50            | Void Volume Fraction ( $f$ ) Distribution in the Target Plate at Different Impact Velocities.       | 113         |

# LIST OF TABLES

| <u>TABLE</u> |   | <u>PAGE</u> |
|--------------|---|-------------|
| 1            | SUMMARY OF SHB TESTS                                  | 10          |
| 2            | RESULTS FROM LONG-ROD EXPERIMENTS                     | 35          |
| 3            | YIELD STRENGTHS (IN GPa) FROM DIFFERENT TESTS         | 35          |
| 4            | OBSERVED HEL AND SPALL THRESHOLDS FOR CRACK FORMATION | 42          |
| 5            | SUMMARY OF THE RESULTS ON 1215 STEEL                  | 56          |
| 6            | BODNER-PARTOM PARAMETERS                              | 70          |
| 7            | BODNER MODEL PARAMETERS                               | 71          |
| 8            | DYNAMIC FAILURE MODEL PARAMETERS                      | 108         |

## SECTION I

### INTRODUCTION

High strain rate characterization of several materials has been described in an earlier report [1]. The results in this report include: (1) the use of induction coil technique to perform high temperature split Hopkinson bar tests, (2) the use of manganin stress gauge technique to measure the stress history in impact experiments, (3) an experimental technique involving a flyer plate impacting a long rod to measure initial yield stress, (4) the measurement of shear strength using transverse and longitudinal manganin gauges, (5) an improved experimental setup for expanding ring experiments, (6) the high strain rate modeling of several metals using the Bodner-Partom model under both room and high temperatures, (7) the precursor decay analysis based on a new offset yield criterion, and (8) a new dynamic failure model based on an improved void growth model approach.

The various high strain rate experimental techniques and results for several metals are reported in Section II. Analytical modeling of the high strain rate data is reported in Section III and IV. Summary of the results and several recommendations are described in Section V.

## SECTION II

### EXPERIMENTS

For high strain rate material characterization, we employed the split Hopkinson bar (SHB) technique to deform specimen under uniaxial stress in both tension and compression at strain rates of  $10^2$ - $10^3$ /sec, the expanding ring technique to measure the average stress obtained at strain rates of above 5000/sec and at large strains, the plate impact tests to measure the initial yield stress in uniaxial strain at very high strain rates, and the flyer plate on long rod impact experiments to obtain initial yield stress at strain rates of 100-500/sec. Manganin gauge techniques to measure stresses in the plate and long rod impact tests are discussed. The use of the induction coil heating method in SHB experiments is also reported. These techniques have been described in detail in References 1-4. For completeness, a brief description of each technique and data are presented in this section.

#### 2.1 SPLIT HOPKINSON BAR

##### 2.1.1 Basic Configuration

The SHB apparatus consists of a striker bar that is made to impact end-to-end onto the pressure bar. The impact produces a stress wave in the pressure bar whose duration is twice the acoustic transit time of the striker bar. The specimen is placed at the other end of the pressure bar as shown in Figure 1. The specimen is also connected to the transmission bar. The striker, pressure, and transmission bars are all the same material and diameter (12.7 mm diameter Inconel 718). The stress wave that travels down the pressure bar is partially transmitted and partially reflected by the specimen. The reflected and transmitted waves in the bars are detected by strain gages. Analysis of the strain-gage signals yields the load and displacement history of the specimen. Detailed discussions on the strain-gage analysis can be found in Refs. 5 and 6.

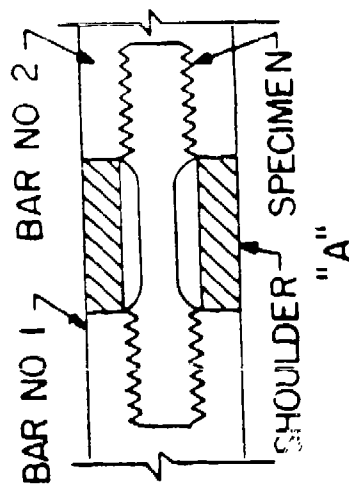
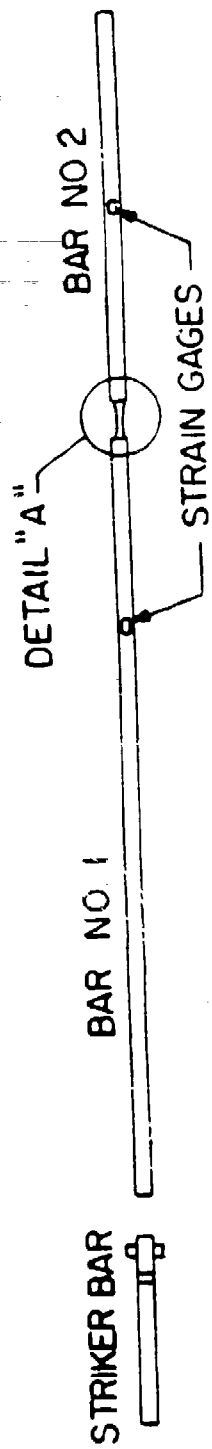


Figure 1. Schematic Sketch of the SHB Setup.

For tensile measurements, a collar is placed around the threaded-end specimen, and the specimen is screwed into the pressure and transmission bars. The initial compression wave is transmitted through the collar, and reflects as a tensile wave. When the tensile wave returns to the specimen, the collar falls away and only the specimen sustains the tensile load. The data from the Hopkinson bar strain gages are used to calculate engineering stress and strain in the sample, which is converted to true stress and strain until the onset of localized deformation (necking) by using the conventional relationships.

#### 2.1.2 High Speed Photographic Technique

A photographic system was used to record images of the specimen profile throughout the test. The system is described in detail in Ref. 7. Light-emitting-diodes (LED) back illuminate the specimen which is viewed by a 35 mm rotating drum camera. One photograph of the necking specimen could be obtained in every 20 microseconds with a framing rate of 50 kHz. The Bridgman parameters  $a$  and  $R$  were determined from the various photographs at different time intervals of the specimen (see Reference 8). Bridgman equations were then used to calculate the stress-strain relations beyond the onset of necking.

#### 2.1.3 Induction Coil Heating Technique

To obtain SHB data under high temperature, an induction coil heating technique was developed. During the past 20 years many workers designed various heating systems in order to perform high-temperature tests in the SHB system. Heating of the specimen was achieved by placing various kinds of heaters near it. There are two major difficulties with those techniques: (1) the time needed to heat the specimen is relatively long; and (2) the heating is not localized and a large volume (including bar tips) is heated. Thus, a temperature gradient is established along the loading bars to either side of the specimen. Such gradients produce variations in the elastic modulus of the bars and hence variations in the elastic velocity. As a result, elastic pulses propagating along the bar suffer from partial reflections and from



change of amplitude. Several techniques to reduce these temperature gradients and methods to account for them in the data reduction process are described in Ref. 9. The need to heat the specimen at high rates also emerges when one wants to avoid microstructural changes (like grain growth and recrystallization) which can occur at elevated temperatures. Rosenberg et al. [4] developed a simple heating technique which is both fast and localized.

The specimen to be heated is surrounded by an induction coil which carries a high-frequency current as shown in Figure 2. The specimens were heated by a radio frequency generator manufactured by Lindberg/Cycle Dyne (Model No. A-50). This generator uses the 240-V line power, which is stepped up via a transformer to about 5000 Vac. This high voltage is rectified and the resulting dc is supplied to an RF power oscillator operating at approximately 450 kHz. The output of this oscillator is about 5 kW and this is coupled to the sample by using 0.25-in. copper tubing coils, which surround the sample. The output power is usually set to maximum in order to make the heating process as short as possible.

Since the magnetic field varies inversely with the square of the distance between the specimen and the coil, one wishes to work with the smallest possible coil if the heating time is a limiting factor. The coils used in the present study were larger than the Hopkinson bar diameter (12.7 mm) by only about 3 mm. In order to avoid heating the collar, we replaced the metallic collar by a ceramic one. Alumina AD-995 (manufactured by Coors) was used because it has an acoustic impedance which is very close to that of the Inconel 718 bars. This matching of impedance results in a smooth passage of the stress wave from the first bar to the second through the ceramic collar.

The temperature of the specimen just prior to loading was measured by use of a thermocouple inserted through a hole drilled in the ceramic collar. The thermocouple touched the specimen so that the temperature was monitored continuously during

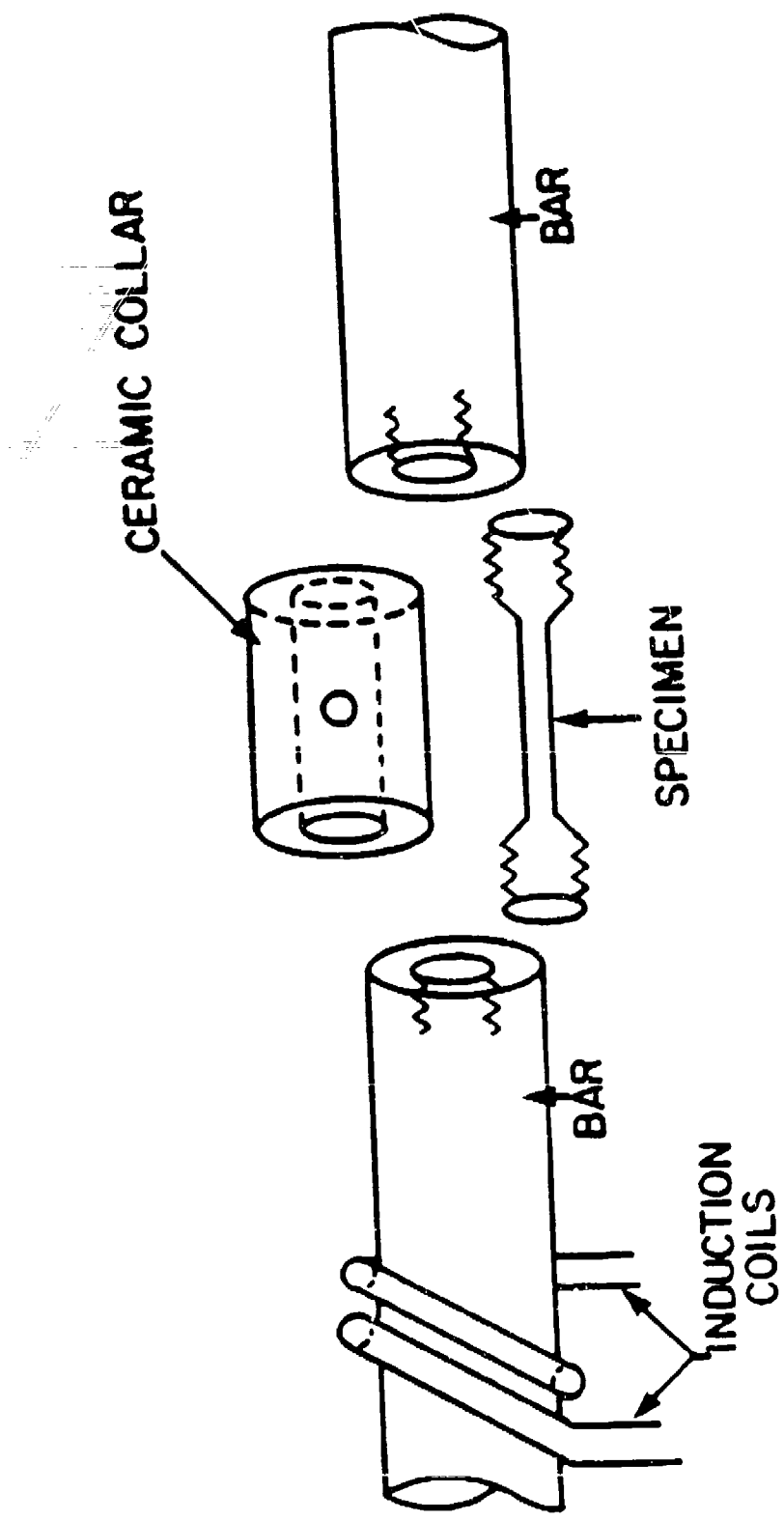


Figure 2. Schematic Diagram of the Induction Coil Heating Technique Used in SHB.

the heating process. When the temperature reached the desired value, the striker bar was fired. In order not to heat the bars too much, we heated the specimens for about one to two minutes in all the experiments described here. We could heat steel specimens to 700°C in about one minute with the double wound arrangement. We also tried a single-coil configuration, but this was not as efficient as the double coil probably because of worse matching between specimen and field. In some of the experiments, the ends of the bars were heated but their temperature was much less than that of the specimens and the heated portion of the bar extended to only about 10 mm. To determine the effect of such heating on the wave propagation characteristics, we conducted two experiments in which the tips of the bars touched each other and were heated to 200°C and 400°C. The transmitted and reflected pulses were compared with those obtained at room temperature and the difference in the measured strain pulses were less than one percent. Since the SHB is made of Inconel, its elastic modulus is relatively insensitive to temperature - decreasing by only 20 percent when heated to 700°C.

The thermocouple to measure the temperature in the specimen was an ungrounded probe (manufactured by Omega, Probe No. SCASS-03236). This probe is especially suited because it can touch the specimen without causing triggering of the scope. Other probes, which were grounded, caused trigger problems because the specimen and the bar are part of the triggering circuit. The maximum reliable temperature with this probe is 927°C, according to the manufacturer. Also, due to the very small dimensions of the probe tip (diameter of 0.9 mm) temperature equilibrium with the specimen was fast. In order to estimate the uniformity of the temperature along the specimen during heating, a few test were run in which the temperature was checked at a few points along the specimen. At an average temperature of 500°C the maximum difference between the points was less than 10°C. A value of  $\pm 2$  percent correction may be needed for the temperature determination. We conducted high temperature SHB tests in tension on several

metals. Figure 3 summarizes the results for W-2 tungsten, 52125 steel, C1008 steel, Nickel 200, and 6061-T6 aluminum.

#### 2.1.4 Results

Using the SHB experimental techniques, compression, tension, and necking tests under room temperatures and tension tests at elevated temperatures were conducted on several metals. Table 1 described the various tests that were conducted under the present study. Quasi-static tests were also conducted for evaluating the rate dependency in these materials by comparison with SHB data.

##### a. Armco Iron

Several tension and compression tests were conducted at room temperature. This material exhibited a fair amount of rate dependency as can be seen from the true-stress vs.  $\log \dot{\epsilon}$  plot in Figure 4. The true stress vs. true strain curves at various strain rates are also shown in Figure 5. The flow stress under SHB strain rate levels varied between 6 and 7 kbars. The strain hardening was almost negligible. Due to the strain rate sensitivity in this material, the SHB flow stresses are more than double those of the quasi-static tests.

##### b. Nickel 200

Two quasi-static tests at strain rates of  $0.001$  and  $1.0s^{-1}$  and several SHB tests under tension were conducted at room temperature. The results are shown in Figure 6. The stress-strain curves at these strain levels were very similar as can be seen from this figure. This indicates that the material is not strain-rate dependent, although it exhibited a significant amount of hardening. The flow stress (5.5 kbars) at 15 percent strain was more than twice the initial yield stress (around 2 kbars). The high temperature SHB test results are shown in Figure 7. The stress-strain curves at various temperatures show the reduction in flow stress due to increase in temperatures.

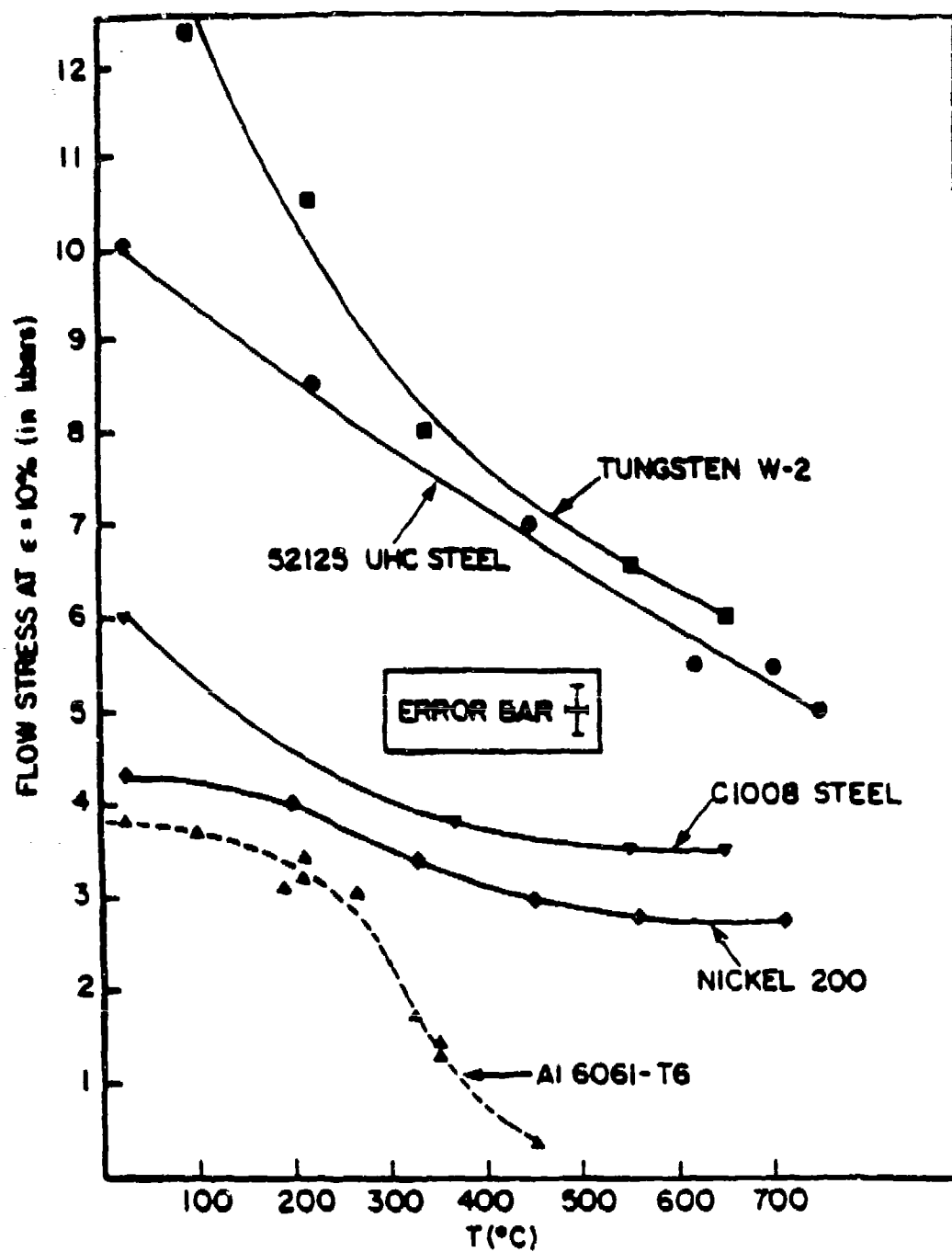


Figure 3. Variation of Flow Stress at  $\epsilon = 0.1$  Against Temperature for Different Metals from Tension Split Hopkinson Bar Tests. (Average Strain Rate - 900/sec.)

TABLE 1  
SUMMARY OF SHB TESTS

| TEST   | TEMPERATURE | TYPE    | MATERIAL   | STRAIN RATE (1/s) |
|--------|-------------|---------|------------|-------------------|
| HB-396 | ROOM        | TENSION | 1044 STEEL | 1200              |
| HB-397 | ROOM        | TENSION | 1044 STEEL | 1225              |
| HB-398 | ROOM        | TENSION | 1044 STEEL |                   |
| HB-399 | ROOM        | TENSION | 1044 STEEL | 700               |
| HB-403 | ROOM        | TENSION | 1044 STEEL | 1150              |
| HB-392 | ROOM        | TENSION | CAST 4140  |                   |
| HB-393 | ROOM        | TENSION | CAST 4140  |                   |
| HB-394 | ROOM        | TENSION | CAST 4140  |                   |
| HB-395 | ROOM        | TENSION | CAST 4140  |                   |
| HB-400 | ROOM        | TENSION | ARMCO IRON | 875               |
| HB-401 | ROOM        | TENSION | ARMCO IRON | 250               |
| HB-402 | ROOM        | TENSION | ARMCO IRON | 1025              |
| HB-404 | ROOM        | TENSION | ARMCO IRON | 1025              |
| HB-405 | ROOM        | TENSION | ARMCO IRON | 800               |
| HB-406 | ROOM        | TENSION | ARMCO IRON | 775               |
| HB-407 | ROOM        | TENSION | ARMCO IRON | 475               |
| HB-408 | ROOM        | TENSION | ARMCO IRON | 475               |
| HB-409 | ROOM        | TENSION | ARMCO IRON | 1300              |
| HB-410 | ROOM        | TENSION | ARMCO IRON | 1300              |
| HB-411 | ROOM        | TENSION | ARMCO IRON | 1300              |
| HB-413 | ROOM        | COMP    | ARMCO IRON |                   |
| HB-414 | ROOM        | COMP    | ARMCO IRON | 150               |
| HB-415 | ROOM        | COMP    | ARMCO IRON | 1600              |
| HB-374 | ROOM        | TENSION | Mar M200   | 240               |
| HB-375 | ROOM        | TENSION | Mar-M200   | 1020              |

TABLE 1 (continued)  
SUMMARY OF SHB TESTS

| TEST   | TEMPERATURE  | TYPE    | MATERIAL    | STRAIN RATE (1/s) |
|--------|--------------|---------|-------------|-------------------|
| HB-376 | ROOM         | TENSION | Mar-M200    | 780               |
| HB-390 | ROOM         | TENSION | Mar-M300    | 800               |
| HB-391 | ROOM         | TENSION | Mar-M300    | 700               |
| HB-296 | ROOM         | TENSION | 52125 STEEL | 660               |
| HB-297 | ROOM         | TENSION | 52125 STEEL | 680               |
| HB-302 | 700 C        | TENSION | 52125 STEEL | 840               |
| HB-303 | 620 C        | TENSION | 52125 STEEL | 800               |
| HB-314 | ROOM         | TENSION | 52125 STEEL | 525               |
| HB-315 | ROOM         | TENSION | 52125 STEEL | 575               |
| HB-316 | ROOM         | TENSION | 52125 STEEL | 1150              |
| HB-317 | ROOM         | TENSION | 52125 STEEL | 1050              |
| HB-318 | ROOM         | COMP.   | 52125 STEEL | 200               |
| HB-319 | ROOM         | COMP.   | 52125 STEEL | 300               |
| HB-320 | ROOM         | COMP.   | 52125 STEEL | 300               |
| HB-321 | ROOM         | COMP.   | 52125 STEEL | 200               |
| HB-326 | ROOM         | COMP.   | 52125 STEEL | 400               |
| HB-327 | ROOM         | COMP.   | 52125 STEEL | 400               |
| HB-334 | 227 C        | TENSION | 52125 STEEL | 725               |
| HB-343 | 445 C        | TENSION | 52125 STEEL | 800               |
| HB-346 | 700-750 C    | TENSION | 52125 STEEL | 775               |
| HB-350 | HIGH UNKNOWN | TENSION | 52125 STEEL | 550               |
| HB-362 | ROOM NECKING | TENSION | 52125 STEEL |                   |
| HB-363 | 445 C        | TENSION | 52125 STEEL | 725               |
| HB-298 | ROOM         | TENSION | NICKEL      | 840               |
| HB-299 | ROOM         | TENSION | NICKEL      | 840               |

TABLE 1 (continued)  
SUMMARY OF SHB TESTS

| TEST   | TEMPERATURE | TYPE    | MATERIAL | STRAIN RATE (1/s) |
|--------|-------------|---------|----------|-------------------|
| HB-300 | 455 C       | TENSION | NICKEL   | 1120              |
| HB-301 | 560 C       | TENSION | NICKEL   | 1150              |
| HB-322 | ROOM        | COMP.   | NICKEL   | 800               |
| HB-323 | ROOM        | COMP.   | NICKEL   | 800               |
| HB-324 | ROOM        | COMP.   | NICKEL   | 1000              |
| HB-325 | ROOM        | COMP.   | NICKEL   | 1000              |
| HB-328 | ROOM        | COMP.   | NICKEL   | 800               |
| HB-329 | ROOM        | COMP.   | NICKEL   | 400               |
| HB-333 | 210 C       | TENSION | NICKEL   | 775               |
| HB-342 | 328 C       | TENSION | NICKEL   | 575               |
| HB-345 | 713 C       | TENSION | NICKEL   | 850               |
| HB-365 | 252 C       | TENSION | NICKEL   | 525               |
| HB-366 | 505 C       | TENSION | NICKEL   | 525               |
| HB-367 | 675 C       | TENSION | NICKEL   | 575               |
| HB-368 | 244 C       | TENSION | NICKEL   | 1625              |
| HB-369 | 502 C       | TENSION | NICKEL   | 1625              |
| HB-370 | 700 C       | TENSION | NICKEL   | 1600              |
| HB-371 | ROOM        | TENSION | NICKEL   |                   |
| HB-372 | ROOM        | TENSION | NICKEL   |                   |
| HB-380 | ROOM        | COMP.   | VANADIUM | 100               |
| HB-381 | ROOM        | COMP.   | VANADIUM | 120               |
| HB-382 | ROOM        | COMP.   | VANADIUM | 1400              |
| HB-383 | ROOM        | COMP.   | VANADIUM | 1300              |
| HB-388 | ROOM        | COMP.   | VANADIUM | 1200              |
| HB-389 | ROOM        | COMP.   | VANADIUM | 700               |



TABLE 1 (concluded)  
SUMMARY OF SHB TESTS

| TEST   | TEMPERATURE | TYPE    | MATERIAL | STRAIN RATE (1/s) |
|--------|-------------|---------|----------|-------------------|
| HB-335 | ROOM        | TENSION | TUNGSTEN | 925               |
| HB-336 | ROOM        | TENSION | TUNGSTEN | 675               |
| HB-337 | 550 C       | TENSION | TUNGSTEN | 450               |
| HB-338 | 650 C       | TENSION | TUNGSTEN | 500               |
| HB-339 | 335 C       | TENSION | TUNGSTEN | 400               |
| HB-347 | 320 C       | TENSION | TUNGSTEN |                   |
| HB-348 | 195 C       | TENSION | TUNGSTEN | 625               |
| HB-349 | 95 C        | TENSION | TUNGSTEN | 500               |
| HB-282 | 120 C       | TENSION | 6061-T6  | 850               |
| HB-283 | 120 C       | TENSION | 6061-T6  |                   |
| HB-284 | 150 C       | TENSION | 6061-T6  | 920               |
| HB-288 | 210 C       | TENSION | 6061-T6  | 775               |
| HB-289 | 210 C       | TENSION | 6061-T6  | 750               |
| HB-290 | 345 C       | TENSION | 6061-T6  | 800               |
| HB-291 | 347 C       | TENSION | 6061-T6  | 800               |
| HB-304 | 190 C       | TENSION | 6061-T6  | 880               |
| HB-305 | ROOM        | COMP.   | 6061-T6  | 800               |
| HB-353 | 458 C       | TENSION | 6061-T6  | 975               |
| HB-353 | 458 C       | TENSION | ALUMINUM | 975               |

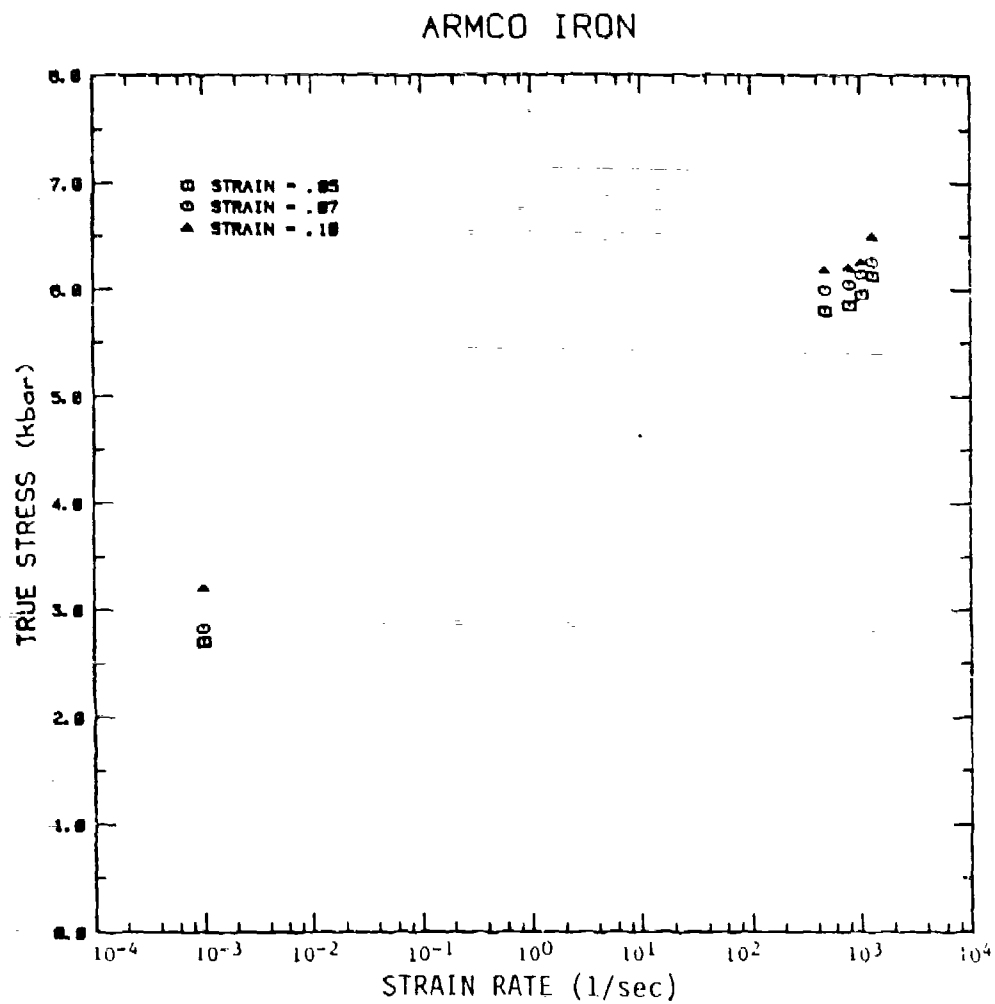


Figure 4. True Stress vs. Log  $\dot{\epsilon}$  Plot for Armco Iron at Different Strain Levels.

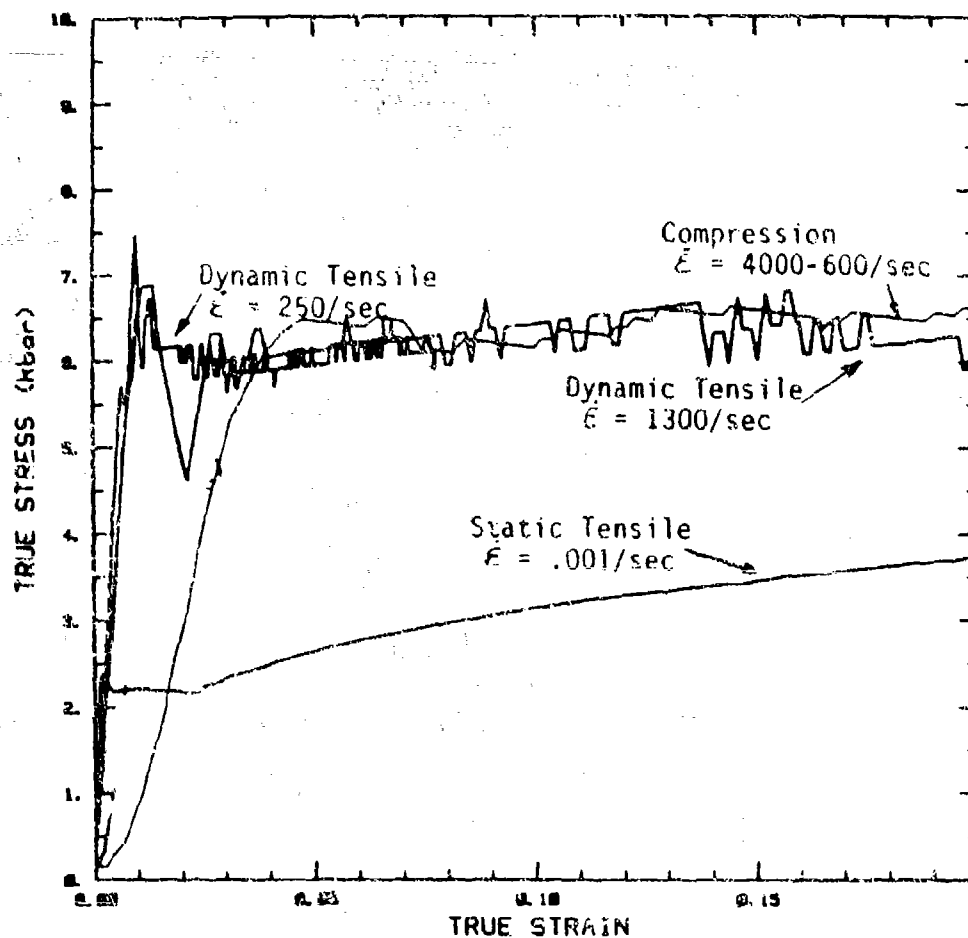


Figure 5. True Stress vs. True Strain Data from Quasi-static and SHR Tests for Armco Iron.

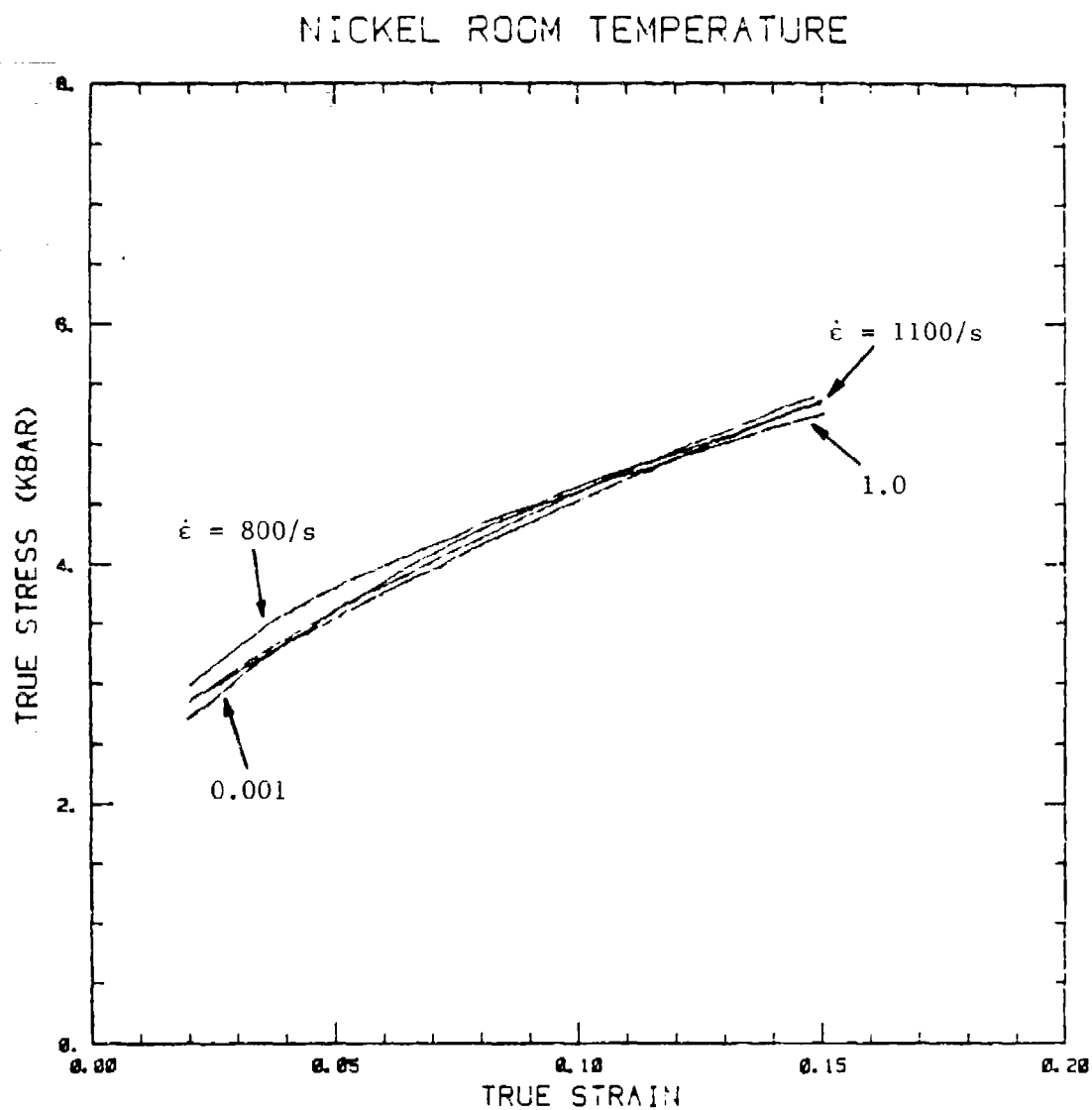


Figure 6. True Stress vs. True Strain Plots for Nickel 200 at Room Temperature under Quasi-static ( $\dot{\epsilon} = 0.001$  and  $1s^{-1}$ ) and SHB ( $\dot{\epsilon} = 800$  and  $1100s^{-1}$ ) Levels.

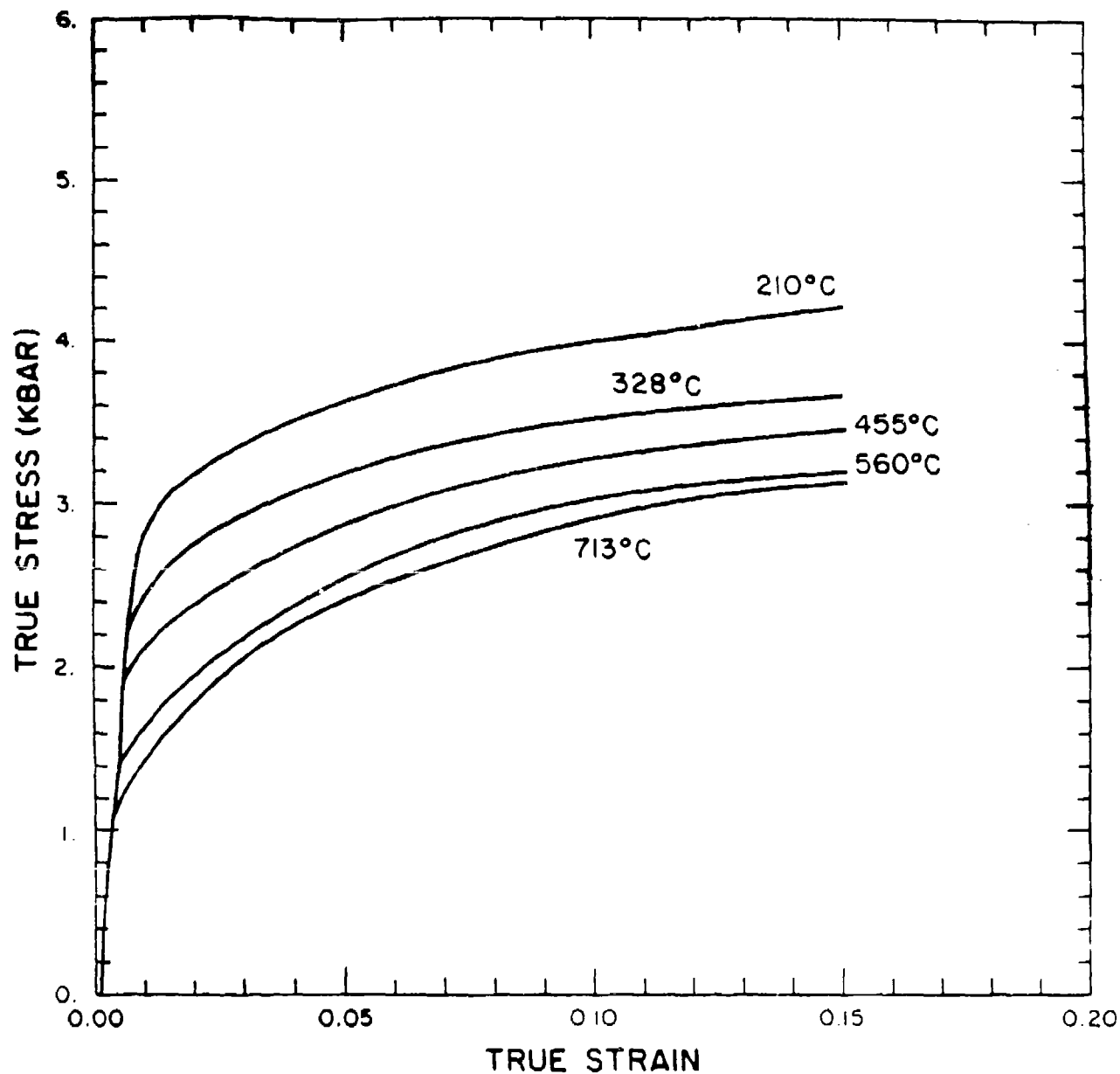


Figure 7. True Stress vs. True Strain Plots at Elevated Temperatures for Nickel 200. (Results are for Tension SHB Tests at Average Strain Rates of 600 to 1200  $\text{sec}^{-1}$ .)

c. W-2 Tungsten

Both room and high temperature SHB tests were conducted. The test temperatures ranged from room to 650°C. The elevated temperature results were obtained at strain rates of  $400\text{s}^{-1}$  to  $600\text{s}^{-1}$ . The tension tests at room temperature were performed at strain rates which ranged between  $250\text{s}^{-1}$  to  $1250\text{s}^{-1}$ . In addition to these SHB tests, two quasi-static tests at strain rates of  $0.001\text{s}^{-1}$  and  $1.0\text{s}^{-1}$  were conducted. The results, shown in Figure 8a, indicate that the flow stresses at  $1.0\text{s}^{-1}$  are higher than at  $0.001\text{s}^{-1}$ . Thus, the flow stresses at SHB strain rates are expected to be much higher than under quasi-static tests because of the rate sensitivity of the material. However, because this material failed at very low strains ( $\sim 0.04$ ), the SHB stress-strain curves could not be resolved due to the mechanical noises associated with the SHB test setup at low strain values as can be seen in Figure 8b. Based on the several tests, we estimated an approximate stress value of 12-13 kbar at strain rates between  $500\text{s}^{-1}$  to  $1000\text{s}^{-1}$ .

The high temperature test results are shown in Figure 9c. The flow stress dropped significantly at elevated temperatures while the strain at failure increased significantly.

d. C1008 Steel

We reported the quasi-static and SHB room temperature results earlier in Reference 1. Several high temperature SHB tensile tests were conducted. The stress-strain curves at room temperature and at 670°C are shown in Figure 9d. The strain rates in these tests were around  $900\text{s}^{-1}$ .

e. 6061-T6 Aluminum

This aluminum is a strain rate independent material. It is known to exhibit slight rate dependency above a strain rate of  $1000\text{s}^{-1}$ . The SHB and quasi-static test results for 6061-T6 have been reported earlier in Reference 10. We conducted SHB tests at elevated temperatures using the induction coil heating

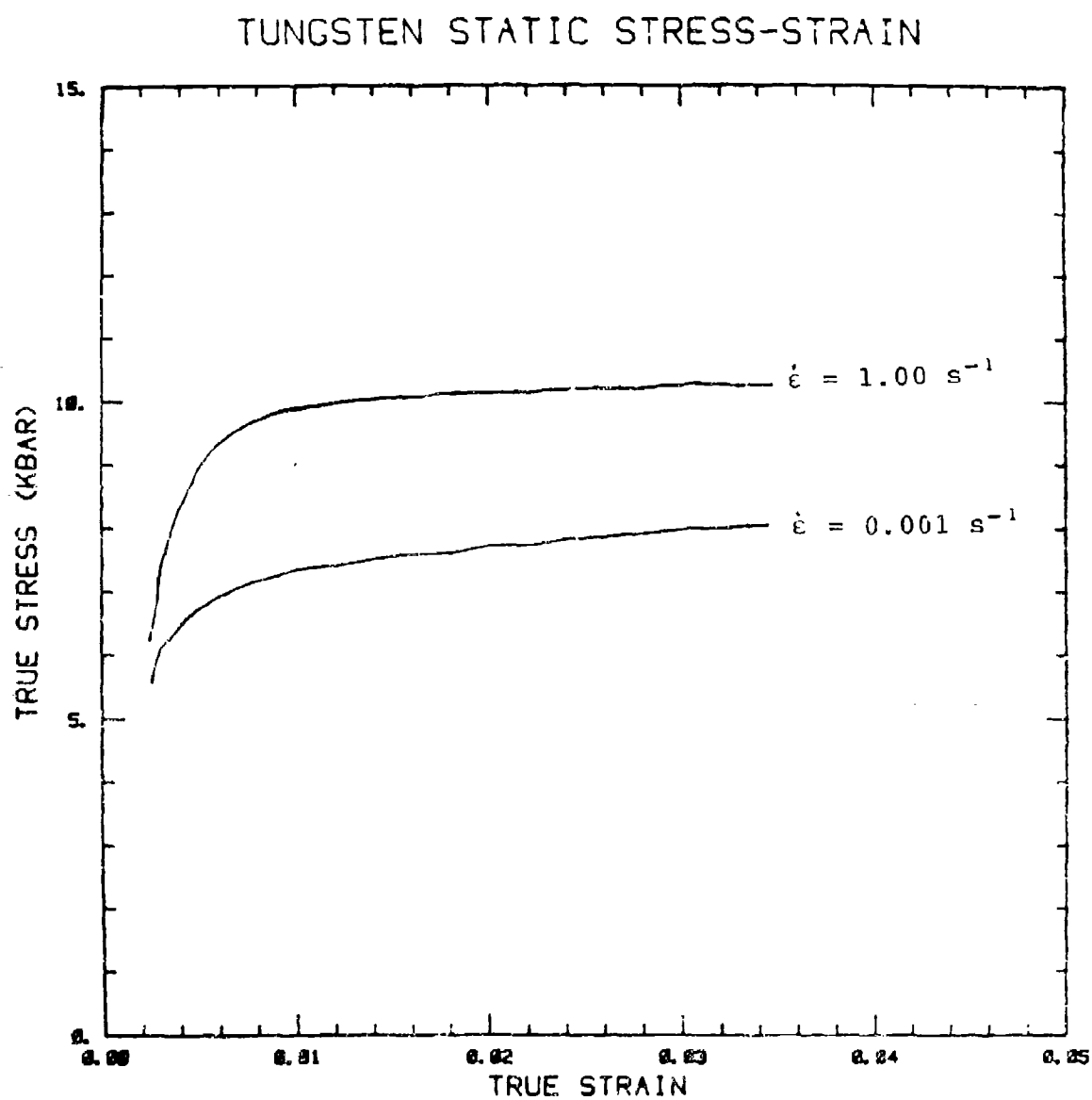


Figure 8a. Quasi-static Test Results for W-2 Tungsten.

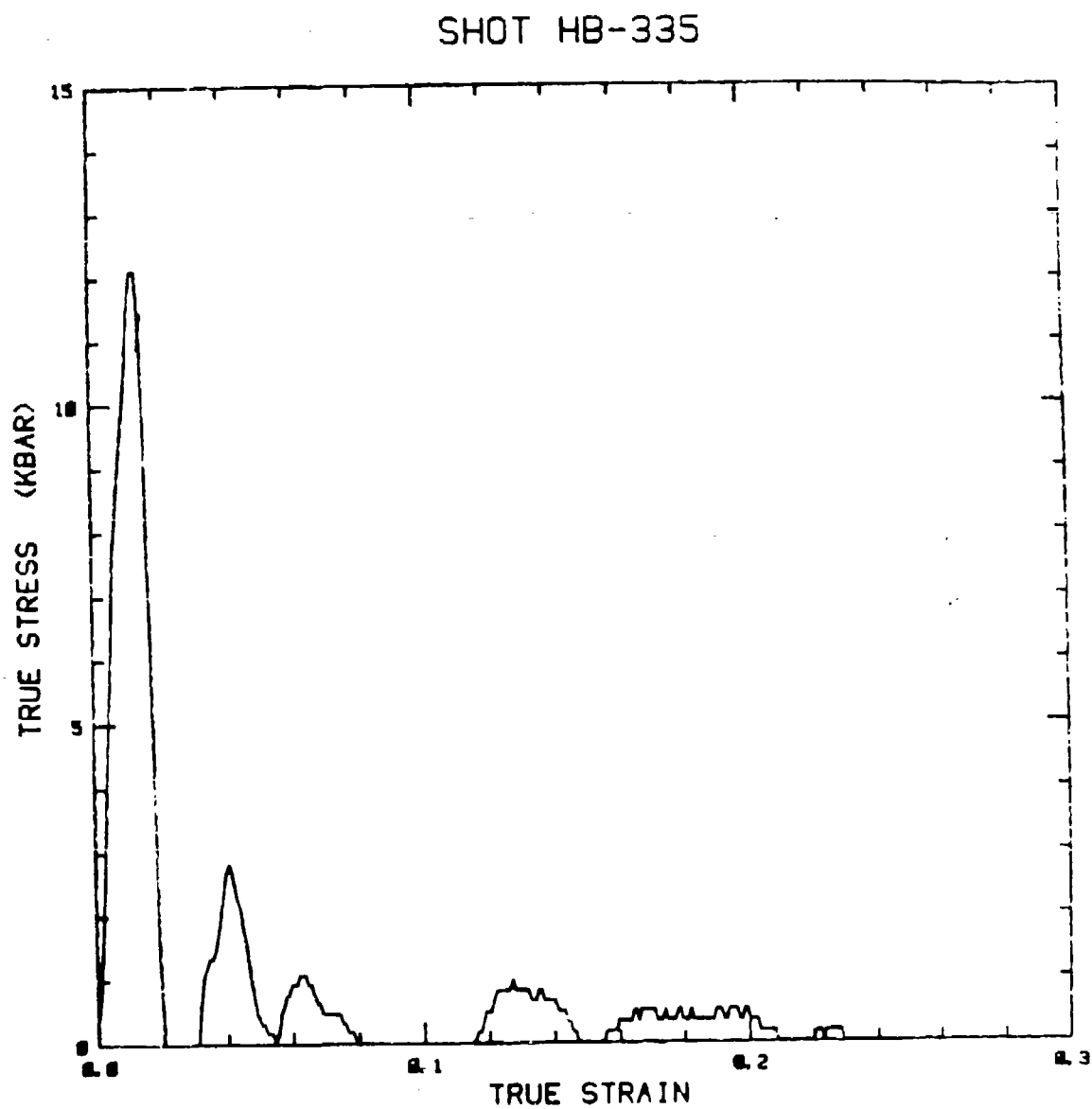
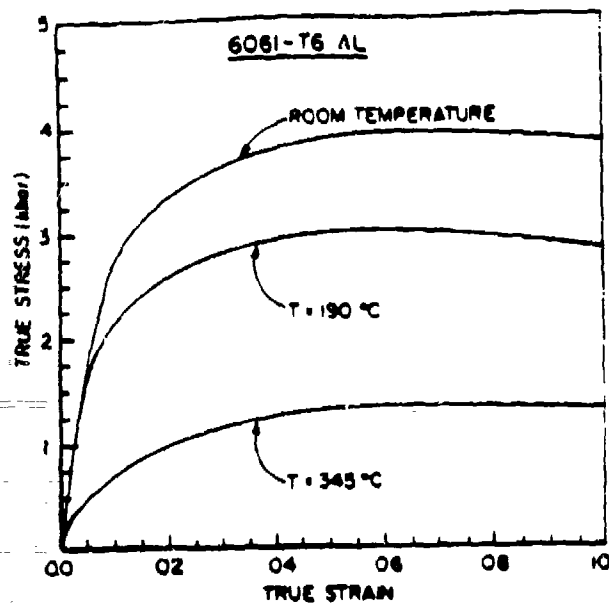
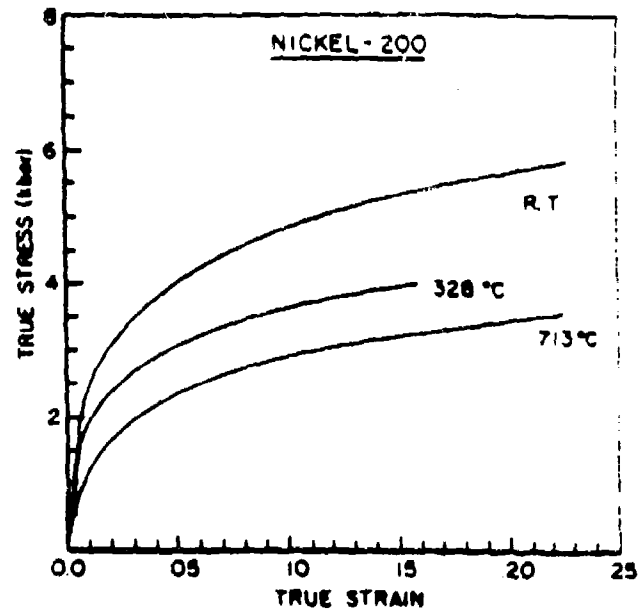


Figure 8b. SHB Tension Test Data at  $\dot{\epsilon} = 925 \text{ s}^{-1}$  for W-2 Tungsten.

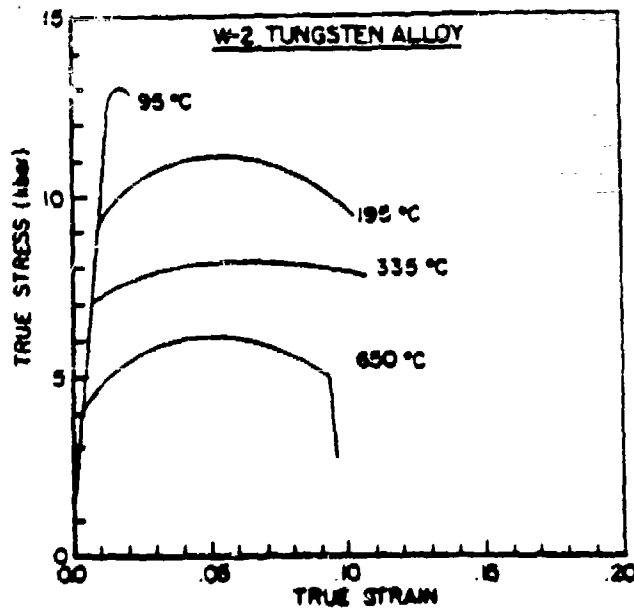




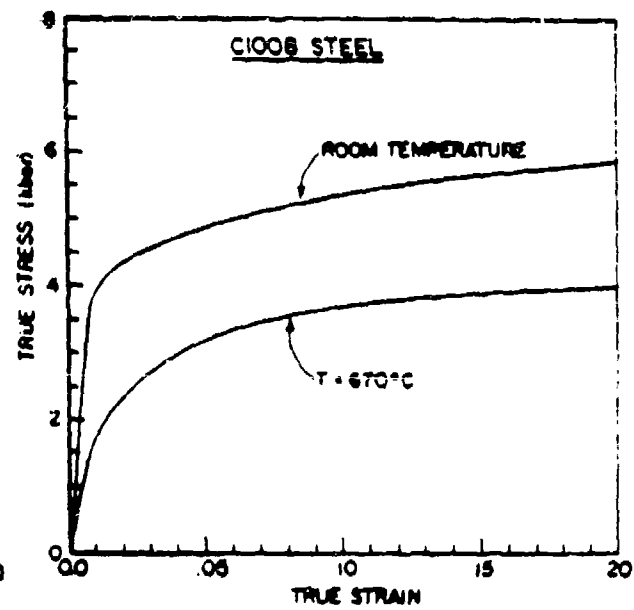
(a)



(b)



(c)



(d)

Figure 9. True Stress-True Strain Plots at Elevated Temperatures for (a) 6061-T6 Aluminum, (b) Nickel 200, (c) W-2 Tungsten, and (d) C1008 Steel.

technique. The results are shown in Figure 9a. The reduction in strength (flow stress) between the room temperature and 150°C is not significant. Above 150°C, the flow stress reduced rapidly for increasing temperatures. This feature can be seen from the earlier Figure 3.

#### f. Additional Results

We conducted necking SHB tests on 1020 steel, 6061-T6 aluminum, HY100 steel, C1008 steel, W-2 tungsten, and 52125 steel. In Figure 10, the stress-strain curves beyond the onset of necking for HY100, 1020 steel, and 6061-T6 aluminum are shown. The data for other materials were not useful due to preceding failures of the specimen before any significant necking. Detailed descriptions of the data reduction scheme and its validity can be found in Reference 8. Based on our earlier reported results for these three materials [1], HY100 steel is the most rate-dependent, 1020 steel is less rate dependent, and 6061-T6 aluminum is the least rate dependent of the three. Consideration of relative rate dependency aids interpretation of the stress-strain curves. In Figure 10, the strain rate is indicated at various points along the curves. The strain rate beyond the onset of necking increased continually as the neck-formation progressed. The increase in flow stress beyond the onset of necking is most significant in the most strain-rate dependent materials. The dotted portions of the curves indicate the estimated strain-hardening behavior based on a simple power-law model ( $\sigma = K\epsilon^n$ ). The additional stress above the dotted line indicates the level of strain-rate sensitivity in the metals. Since 6061-T6 aluminum was the least rate-dependent material, there is relatively little increase in the stress due to strain rate. The additional stress in 1020 steel was higher than in aluminum. HY100 was the most rate dependent, and the increase in flow stress is the most significant. When the strain rate increased most rapidly, the flow stress also showed the steepest increase.

We also acquired SHB tensile and compression data for several other metals. The stress-strain curves for vanadium (compression only), 52125 steel, Mar-M200 steel, Mar-M300 steel,

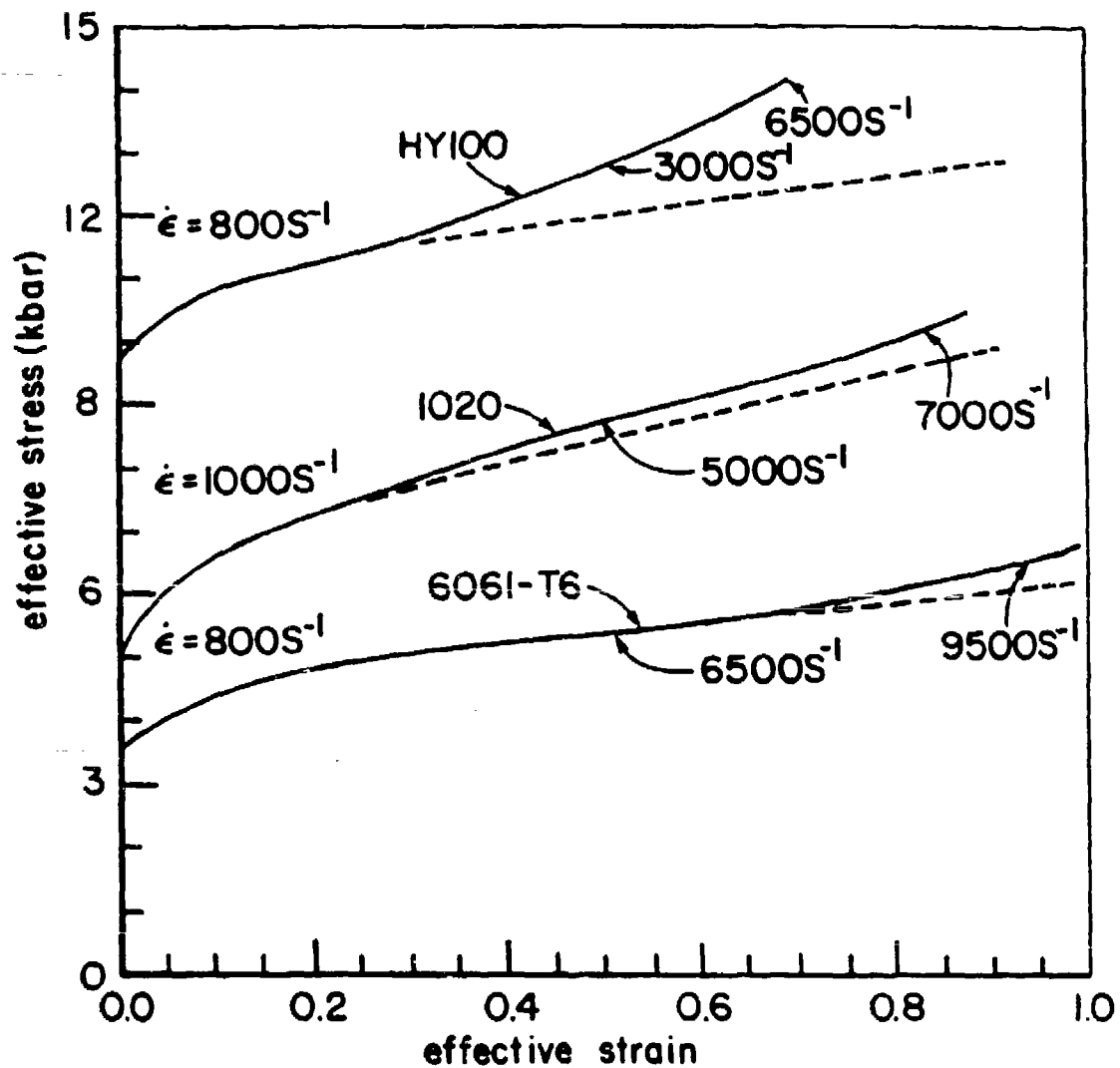


Figure 10. True Stress-True Strain Plots Obtained from High Speed Photographs of Necking Specimens.

cast 4140 steel, tantalum, and 1044 steel are given in Figures 11-16. No reference quasi-static data were obtained for these materials.

## 2.2 LONG ROD IMPACT EXPERIMENTS

The need for developing the long rod experimental technique in which a flyer plate impacts a long rod, was due to the inadequacy of SHB test technique in determining the initial yield stress. The SHB technique is very useful for determining flow stresses at plastic strains beyond three to five percent. The plate-impact technique, on the other hand, is very useful for the determination of dynamic yield strength (at low strains), at very high strain rate. Thus, it is very difficult, if not impossible, to directly compare SHB and plate impact results, especially for rate-dependent materials.

### 2.2.1 Technique

A new technique has been used at the University of Dayton Research Institute which is based on the long-rod impact experiments described in Ref. 11. These experiments give accurate values for the yield strength of the specimen at strain rates of above  $10^2 \text{s}^{-1}$ , thus bridging the gap between static experiments and the plate-impact experiments.

A schematic representation of a long-rod experiment is shown in Figure 17. A 50 mm diameter steel disk is used for a heavy flyer plate. The rod is 12.7 mm in diameter. The gage is inserted at a distance of ten diameters away from the impacted end. Upon impact, both elastic and plastic waves are generated in the rod and propagate towards the gage station. Various calculations show that far enough from the impact face (some ten diameters or so) a state of uniaxial-stress exists in the rod. Thus, at the gage location we expect an elastic uniaxial-stress wave to appear some time after impact. This time is determined by the longitudinal sound speed,  $C_0 = \sqrt{E/\rho}$ , where  $E$  is Young's modulus and  $\rho$  is rod density. The elastic wave amplitude should be equal to the dynamic yield strength of the rod material. The rise time, which

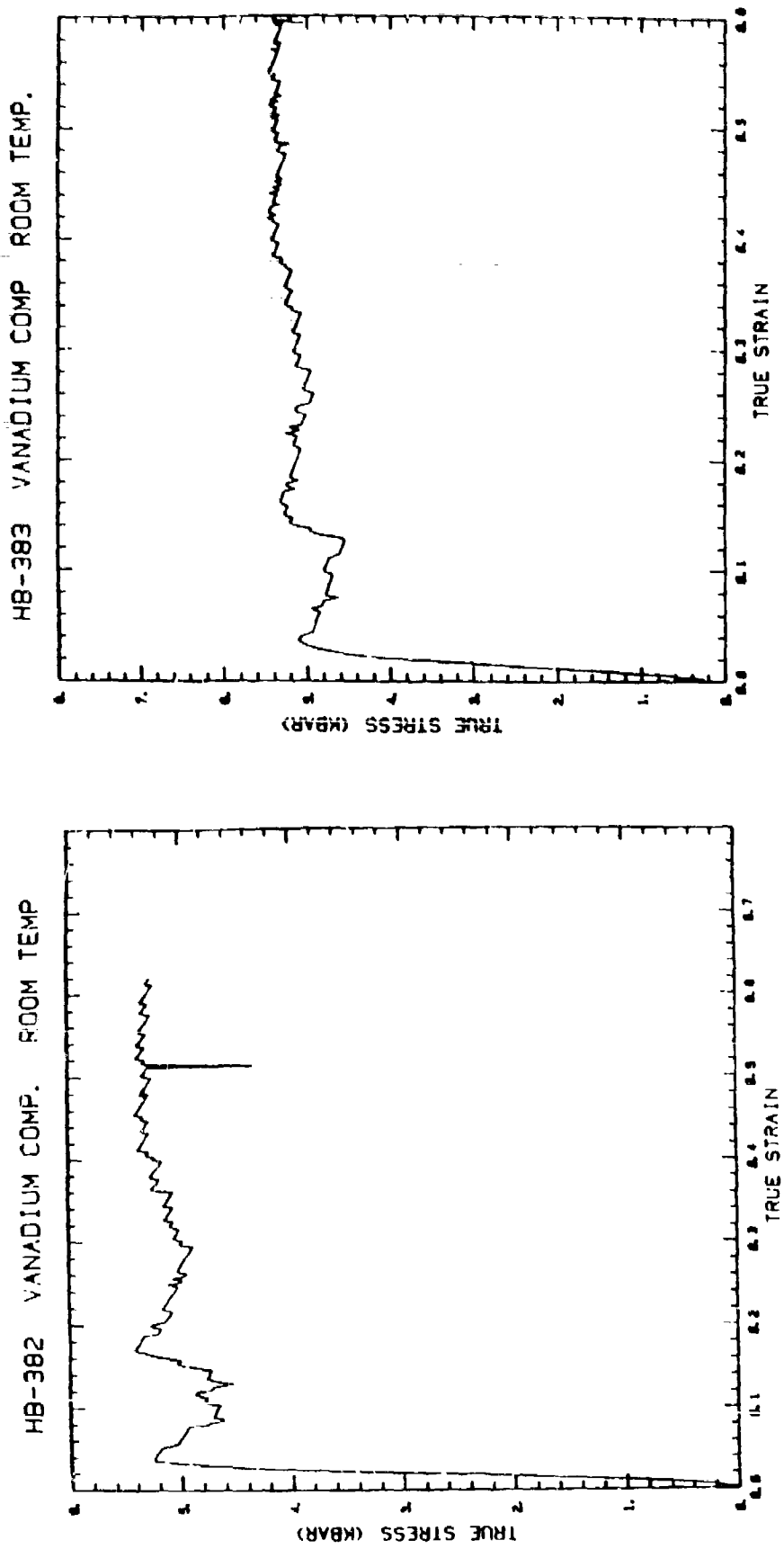
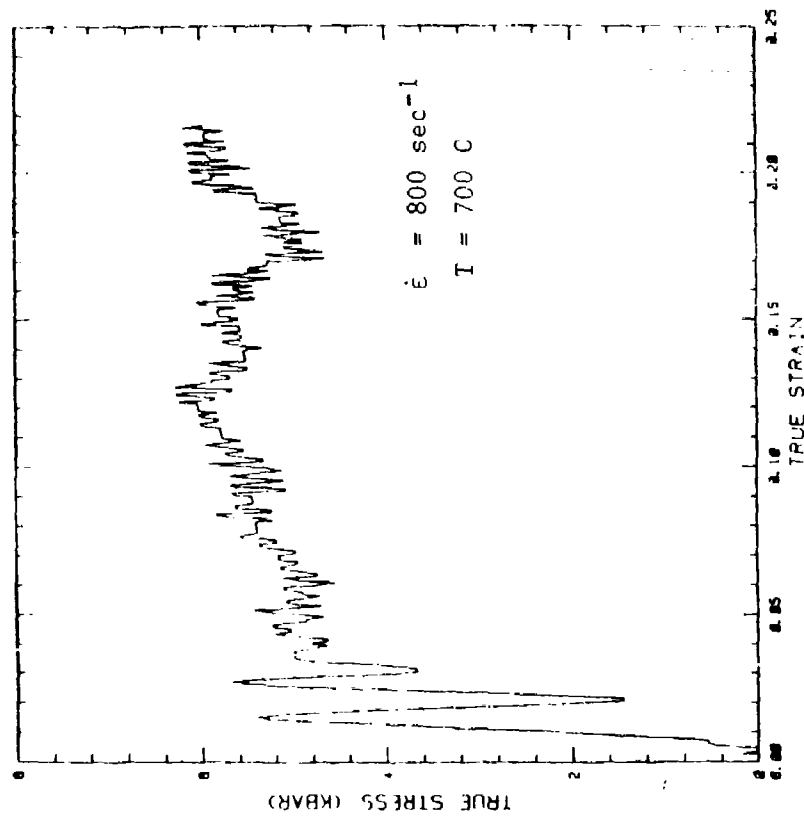


Figure 11. True Stress-True Strain Plots for Vanadium Under Compression.  
 ( $\dot{\epsilon} = 1400\text{--}2000\text{s}^{-1}$ , Note: The Strain Rates Reduced Rapidly from  
 a high ( $1400\text{s}^{-1}$ ) to low ( $200\text{s}^{-1}$ ) in compression tests.)

HB-302 52125 STEEL



HB-303 52125 STEEL

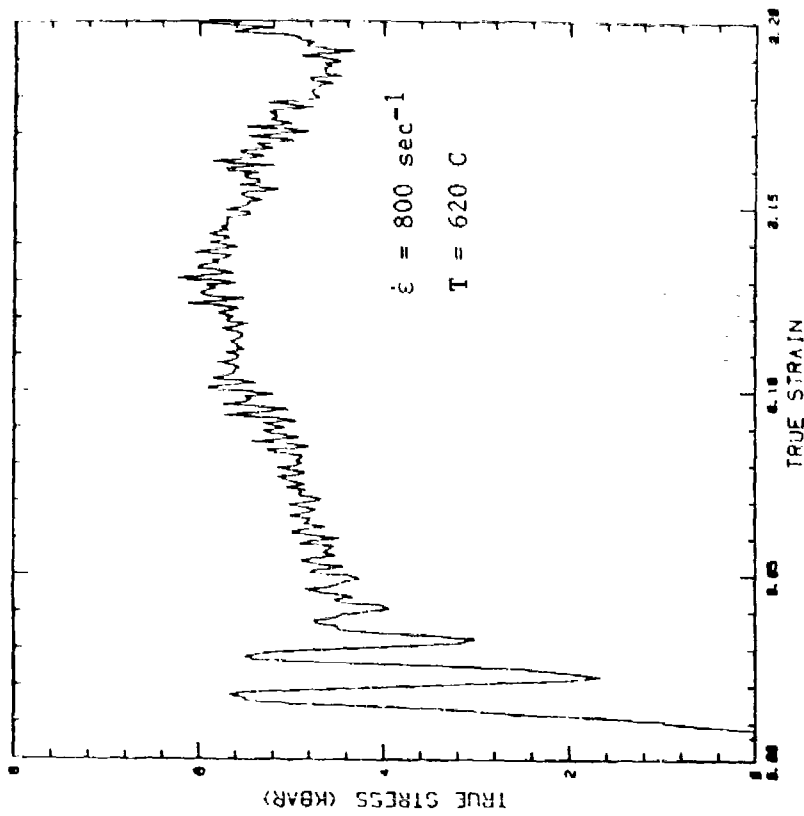


Figure 12. True Stress-True Strain Plots for 52125 Steel under Tension.

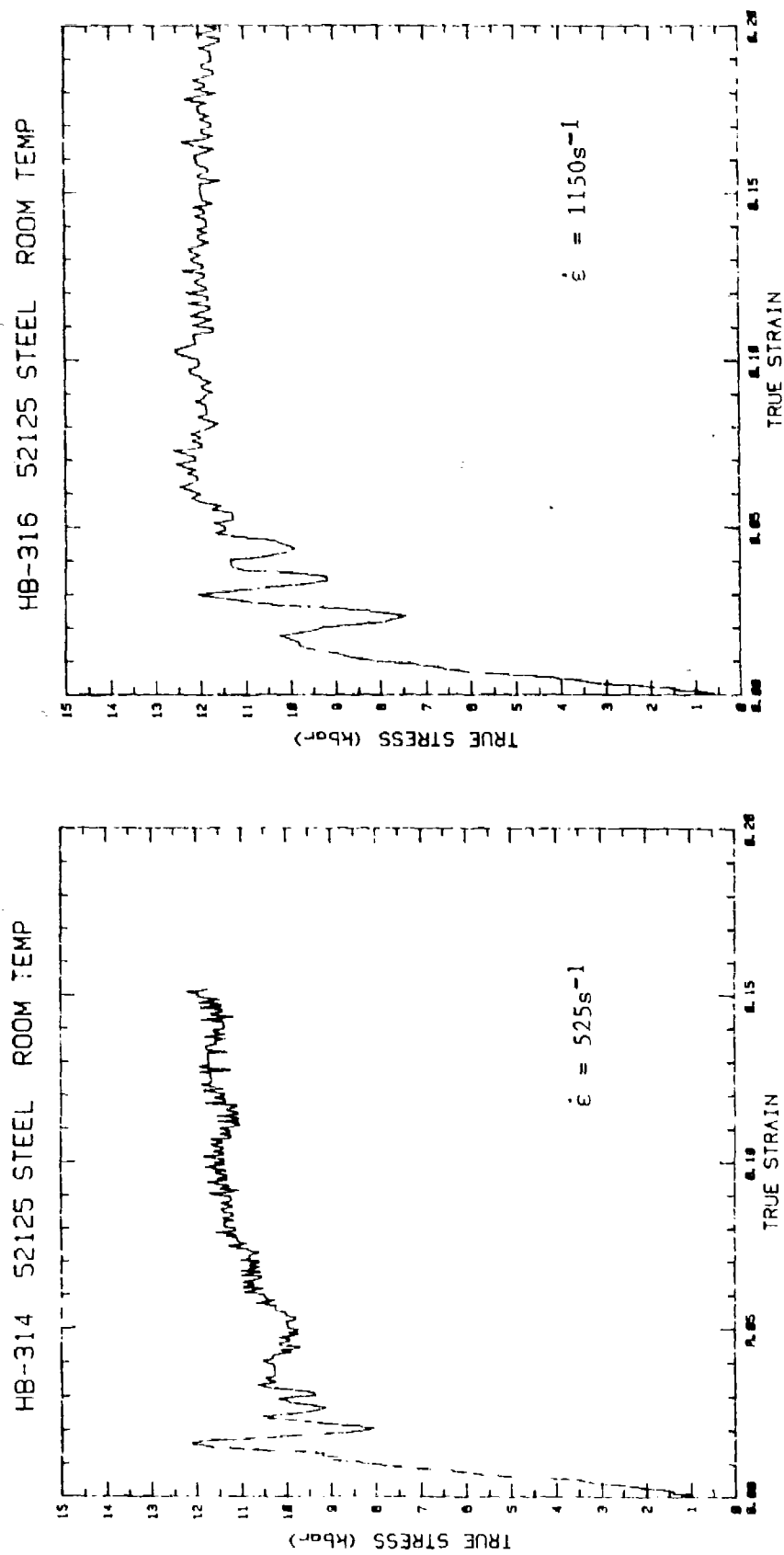


Figure 12. True Stress-True Strain Plots for 52125 Steel Under Tension (concluded).

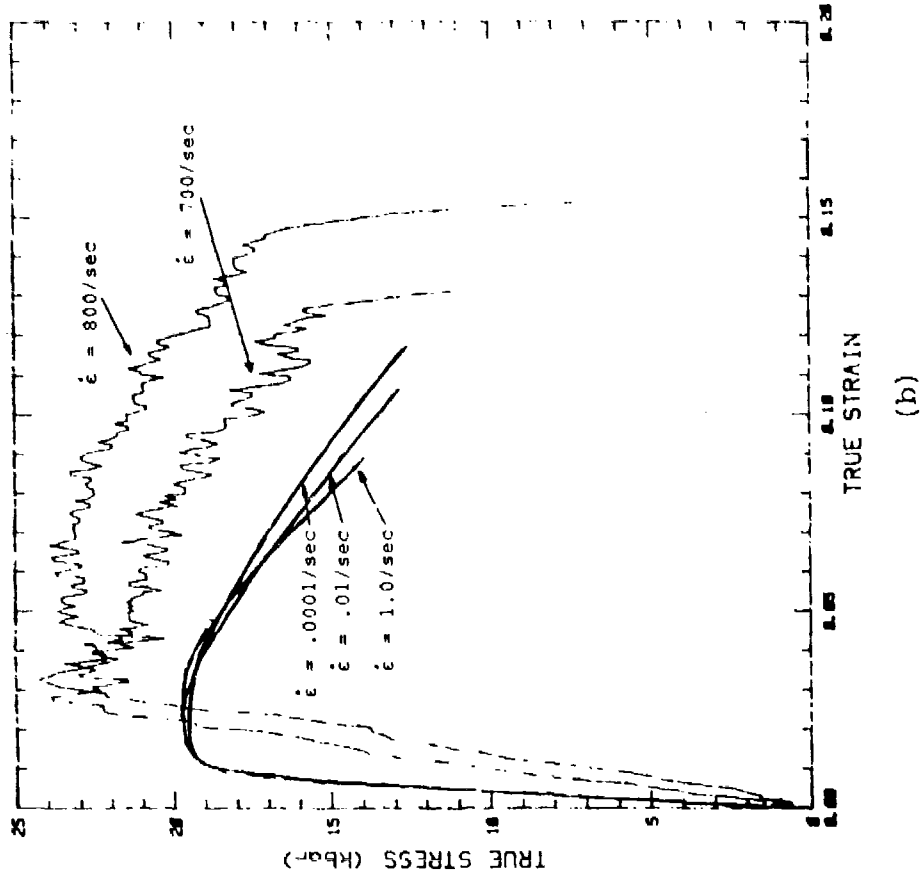
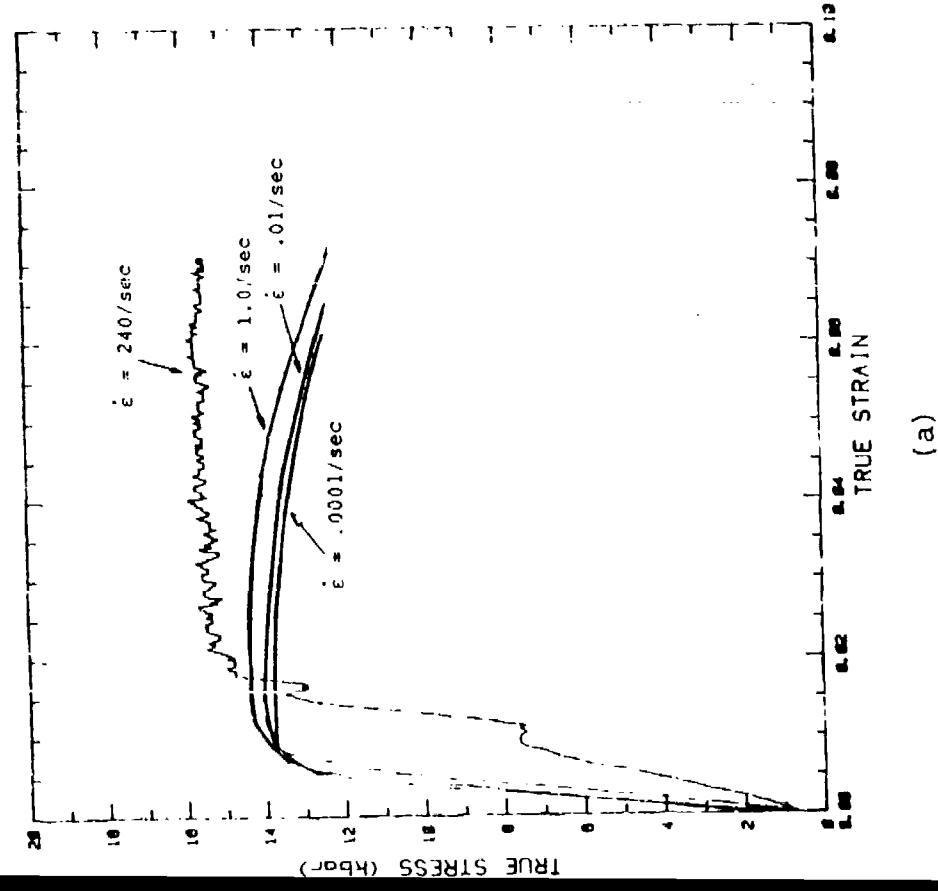


Figure 13. True Stress-True Strain Plots for Maraging Steel (a) Mar-M 200; (b) Mar-M 300.



# 1044 STEEL W/ROLLING ROOM TEMP

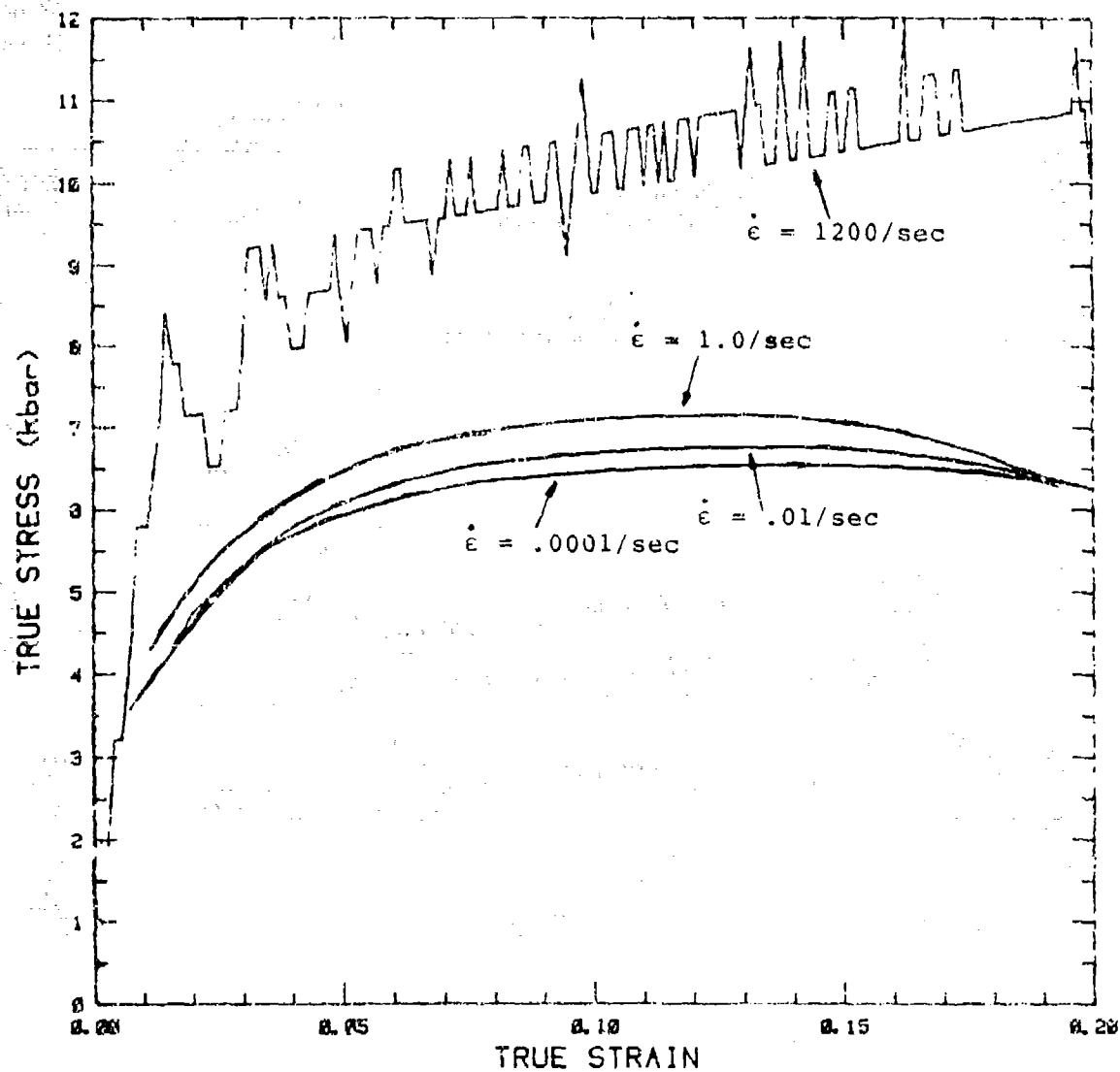


Figure 14. True Stress-True Strain Plots for 1044 Steel Under Tension Rolling Direction.

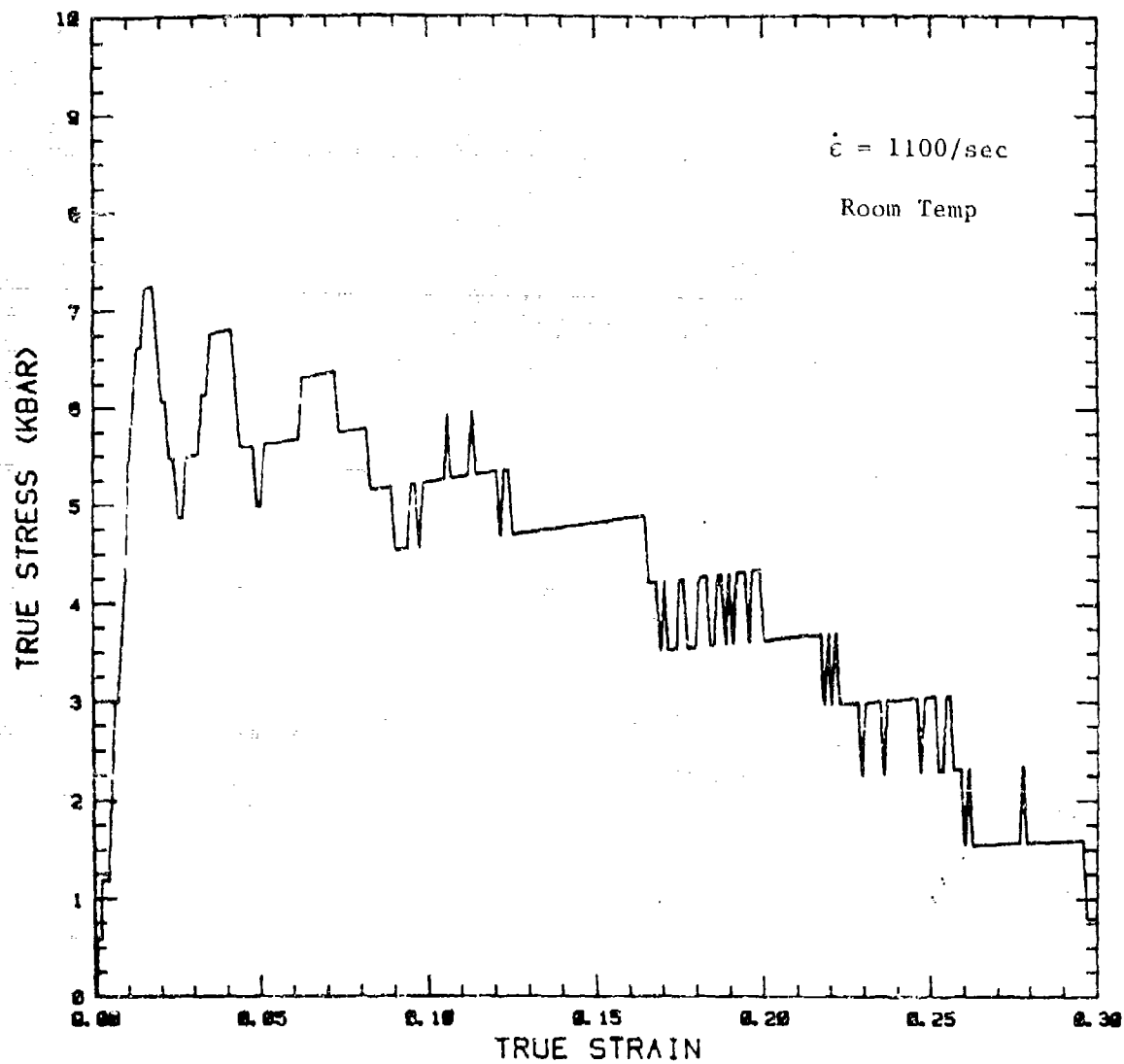


Figure 15. True Stress-True Strain Plots for Pure Tantalum Under Tension.

HB-393 CAST 4140 STEEL RT

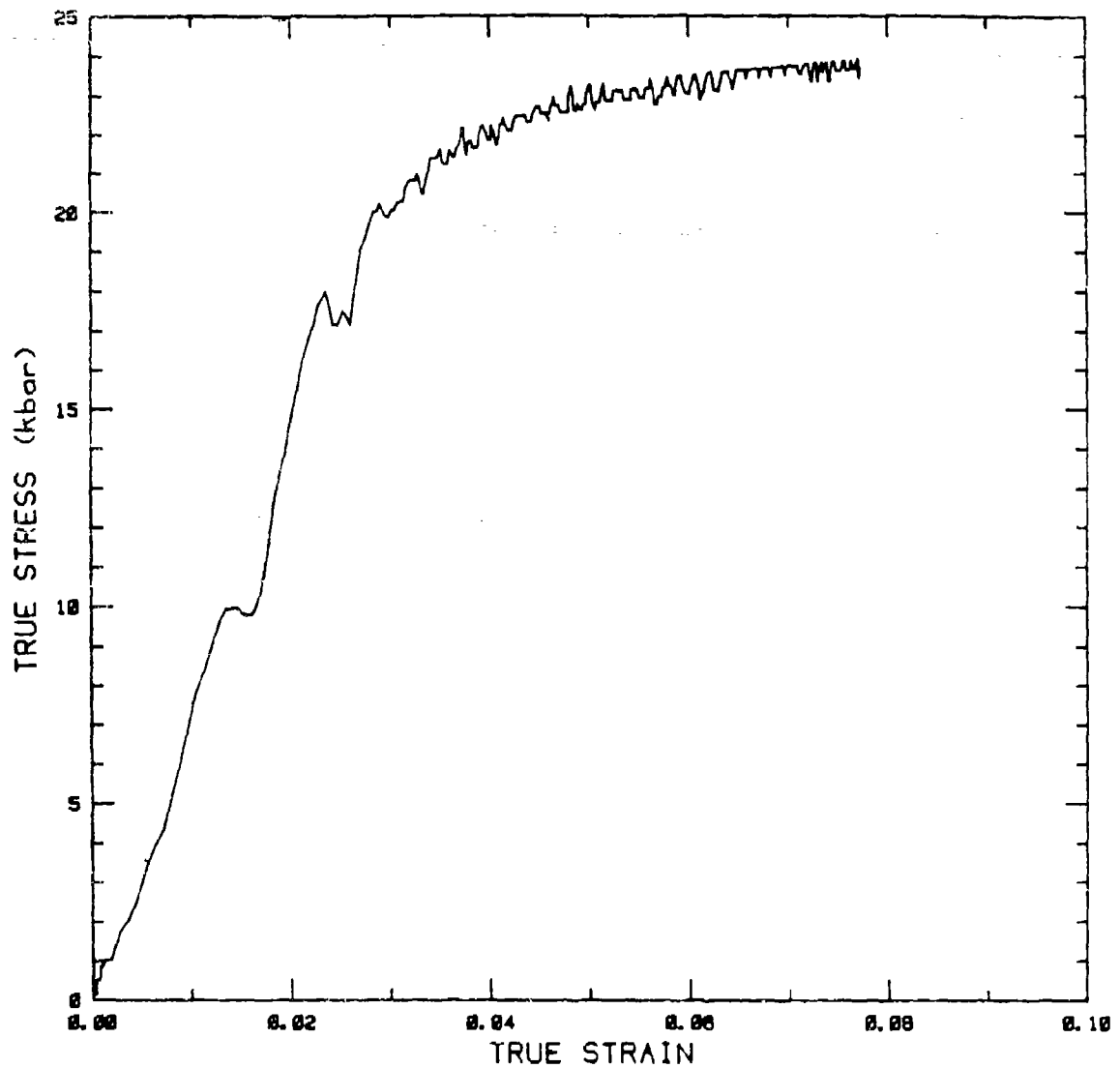


Figure 16. True Stress-True Strain Plots for Cast 4140 Steel at  $\dot{\epsilon} = 1200\text{s}^{-1}$ .

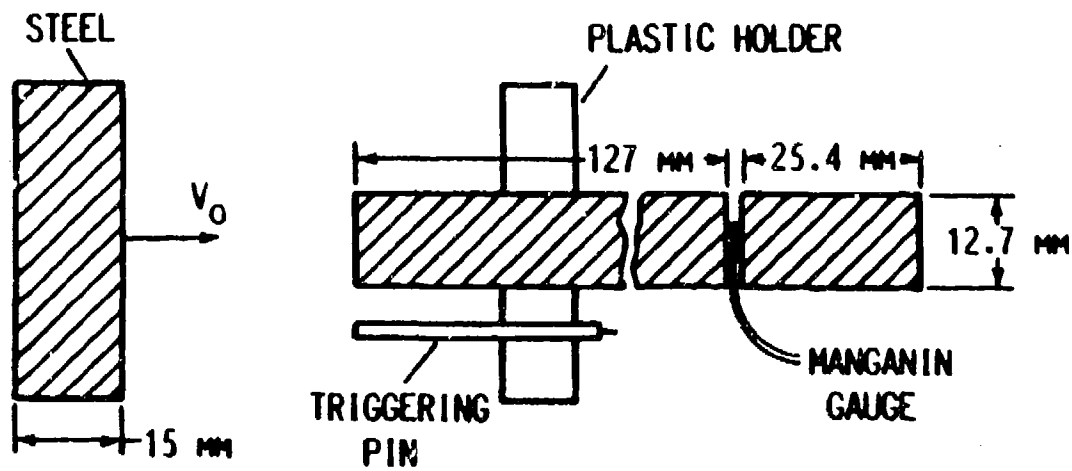


Figure 17. A Schematic Diagram of Long Rod Experiment.

is relatively large because of geometrical dispersion, can be used to derive the (elastic) strain rate.

The fact that the gages, which were calibrated under dynamic uniaxial strain, can be used to measure waves in rods, which experience uniaxial stress, has been explained in Ref. 11. It is assumed that its piezoresistance behavior is the same as in a planar shock experiment. The two parts of the rod, together with the gage and 25  $\mu\text{m}$  thick mylar sheets on each of its sides, are glued together with a Hysol 0151 clear epoxy, in a special fixture which insures good axiality of the parts while the epoxy is curing.

For a rate-insensitive material, such as 2024-T3 aluminum, the measured elastic-wave amplitude is exactly the same as the static yield strength of this material (see Reference 11). Thus the yield strength is the same at strain rates of  $10^{-3}\text{s}^{-1}$ . Moreover, from HEL measurements on this alloy, the dynamic yield strength at  $10^6\text{s}^{-1}$  is also very close to the static value, confirming the rate insensitivity of this material.

A typical gage record from a long-rod experiment is shown in Figure 18. We first note the arrival time of the stress wave (some 20  $\mu\text{s}$ ) which is due to geometric dispersion. A small amplitude oscillation is superimposed on the signal in a similar way to that observed in the earlier work on aluminum rods [11].

### 2.2.2 Results

Experiments were conducted on three steels: 1020, C1008 and HY100. The amplitude for the elastic waves for the three steel specimens is given in Table 2 together with the relevant data concerning these shots. In order to compare these results with the static and plate impact experiments, we listed the various yield strengths for the three steels in Table 3.

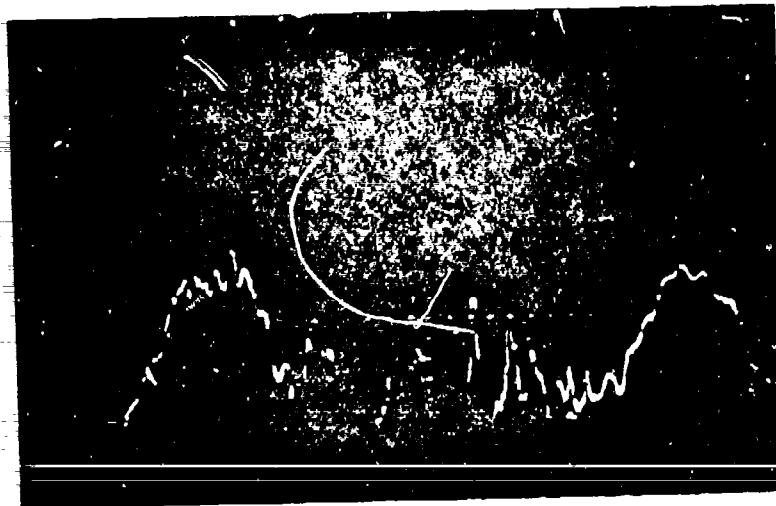


Figure 18. A Typical Stress Gauge Record from a Long Rod Experiment.

TABLE 2  
RESULTS FROM LONG-ROD EXPERIMENTS

| Shot No. | Rod Material | Impact Velocity (m/s) | $Y_d$ (GPa)* |
|----------|--------------|-----------------------|--------------|
| 925      | C1008        | 196                   | 3.7          |
| 926      | HY100        | 201                   | 8.7          |
| 897      | 1020         | 94                    | 5.5          |
| 898      | 1020         | 164                   | 5.2          |

\* Initial yield stress,  $Y_d$

TABLE 3  
THE YIELD STRENGTHS (IN GPa) FROM DIFFERENT TESTS

| Material | Plate Impact<br>( $10^6 s^{-1}$ ) | Long Rod<br>( $10^2-10^3 s^{-1}$ ) | Static Tests<br>( $10^{-3} s^{-1}$ ) |
|----------|-----------------------------------|------------------------------------|--------------------------------------|
| C1008    | 0.65                              | 0.47                               | 0.25                                 |
| HY100    | 1.03                              | 0.87                               | 0.73                                 |
| 1020     | 0.65                              | 0.53                               | 0.25                                 |

The 1020 and C1008 are relatively soft steels compared to the HY100 steel (static yield strength of 7.3 kbar in HY100 as compared to 2.5 kbar for the other two steels) [1].

### 2.2.3 Gage-Signal Analysis

Analysis of the gage record shown in Figure 18 is presented in this section. A small precursor arrives at the gage location at a time which corresponds to a longitudinal wave velocity  $C_L = [(K + 4/3G)/\rho]^{1/2}$  (where K and G are bulk and shear moduli, respectively). The value of  $C_L$  is 6 mm/ $\mu s$  and is higher than the sound speed  $C_0 = 4.6$  mm/ $\mu s$  ( $C_0 = \sqrt{E/\rho}$ , where E is Young's modulus). Their existence shows that the longitudinal elastic

waves do not damp completely even at these large distances from the impact end.

The wave reflections in the long rod can be explained with the aid of a Lagrangian x-t diagram as shown in Figure 19. Upon impact, an elastic precursor (compression wave) travels through the rod. It arrives at the gage location at point 'A' and reflects from the free end at 'B' as a release wave towards the gage section at point 'C'. Further towards the impact end, this release wave encounters the slow-moving plastic boundary at point 'D'. It reflects back at this boundary towards the gage section as a second elastic compression wave. By observing the time of arrival of this reflected wave, we can determine the distance which the plastic front travelled from the impact point until it met the elastic release wave. Thus, for C1008 steel, this interaction occurred 33 mm away from impact; while for the HY100 it was at 44 mm. This difference is consistent with the fact that in the SHB experiments, HY100 experiences more work hardening than C1008 (see Ref. 1). The results for HY100 steel obtained from the manganin stress gages compared extremely well with the results on a similar steel reported by Kuscher et al. in Reference 12.

As mentioned earlier, the SHB is not accurate enough in the low strain region to provide a reliable value for the initial yield stress. Thus, the long-rod experiment fills the gap between the static and shock regimes and complements the data for SHB measurements which give stress-strain curves at plastic strains (beyond 3-5 percent). To accurately determine the strain rate for the long-rod experiment, we used the measured wave amplitude and the Young's modulus of steel to get the strain carried by the wave (in the range of 0.25-0.4 percent) and the rise time of the wave (4-5 microseconds). These result in strain rates in the  $500\text{--}800\text{s}^{-1}$  region. The main contribution of the long-rod experiment is that with a relatively simple and straightforward technique we can measure the yield strength of the specimen at strain rates of  $10^2$  to  $10^3\text{s}^{-1}$ . These values can then be used to complement SHB data which lack accuracy in the low strain region.



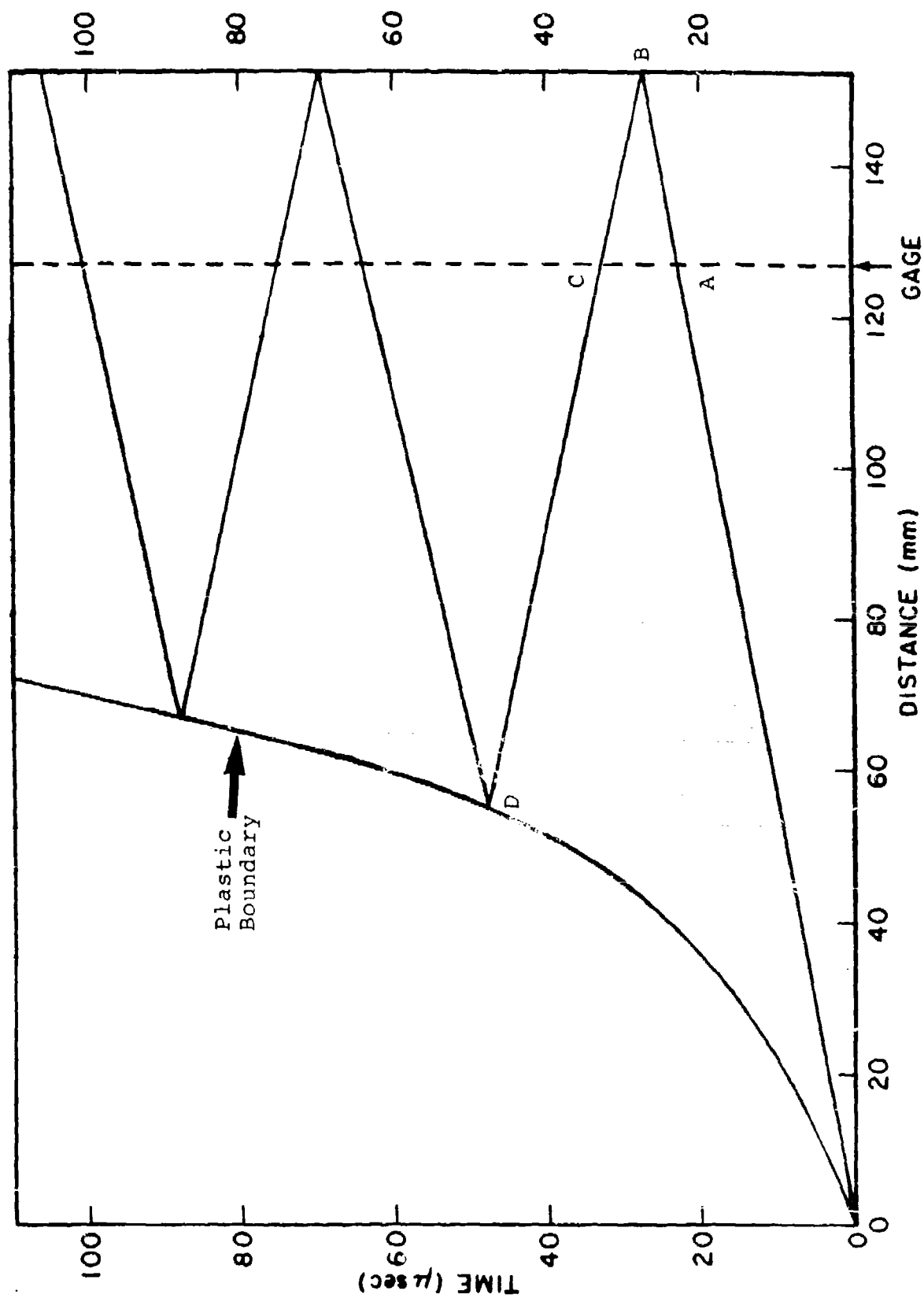


Figure 19. Lagrangian x-t Diagram for the Long Rod Experiment.

## 2.3 EXPANDING RING EXPERIMENTS

The expanding ring technique presents an attractive supplement to conventional tensile test techniques. Relatively high rates can be achieved,  $>10^4 \text{ s}^{-1}$ . However, the most attractive feature of ring tests is that the data analysis is free from assumptions involving wave propagation.

In the expanding ring test, an axisymmetric thin short ring is driven radially outward. The ring may be launched explosively, with a magnetic field or with an exploding wire via a driver cylinder. Most past work with expanding rings has been designed to measure ultimate strain at fracture. The ultimate strain is given by:

$$\epsilon_f = \ln r_f/r_o \quad (1)$$

Here  $r_o$  and  $r_f$  are the initial radius of the cylinder and the radius of failure, respectively. When the average velocity,  $\dot{r}$ , is monitored, strain rate may be calculated from:

$$\dot{\epsilon} = \dot{r}/r \quad (2)$$

The strain in the ring can be determined from the instantaneous diameter. The condition that the ring is in free flight permits the stress in the ring,  $\sigma_\theta$ , to be determined by measuring the radial deceleration:

$$\sigma_\theta = -\rho r \ddot{r} \quad (3)$$

The experimental setup to expand the ring dynamically consists of a capacitor bank with detonating wire assembly, basically as described by Rajendran and Fyfe [13]. An average deceleration can be measured from the record using a streak camera - flashlamp optical setup. We introduced several modifications to both the mechanical operation and the electronic circuitry. This includes: (a) modification of the rail spark gap reducing its separation to 1/4" and hookup of its trigger electrode by a voltage divider, (b)

replacement of the kv trigger module, (c) design and installation of a safety switch, which allows testing of prefire/no fire without discharging the bank, and (d) shadow graph recording system, using a Xenon flashlight and a streak camera. Tests conducted showed a complete detonation of a copper wire 0.85 mm thick, discharging 19 kv from the 87  $\mu$ f capacitor bank at an energy equivalent of about 16 KJ.

Currently, the expanding ring experimental setup is being routinely used. We conducted several tests on 6061-T6 aluminum and 1100-0 aluminum to demonstrate the capabilities of the system. In Figure 20, a sample streak record is shown. On this Air Force contract, we updated our expanding ring facility to acquire high strain rate properties routinely. Future efforts will include acquiring data for several metals.

#### 2.4 PLATE IMPACT EXPERIMENTS

In the plate impact test, a flat flyer plate is impacted against a target plate at a high velocity. The flyer and target may be of the same or different material. Compressive stresses are produced and transmitted rapidly from the plane of impact to the adjacent stress free areas of the material in the form of a stress pulse. Many discussions of planar impact loading are available [14,15].

Plate impact test provide a loading path that is very different from conventional SHB compression or tension tests. The deformation is that of one-dimensional strain, and the mean stress is generally very high compared to that of SHB tests. Strain rates are  $10^5 \text{s}^{-1}$  or higher. The material undergoes compression immediately followed by tension due to a reflected wave from the rear surface of the target. Plate impact experiments are essential for calibrating and validating high strain rate material models that aspire to general applicability. Specifically, plate impact data may be interpreted to infer compression and tensile yield strengths and failure parameters.

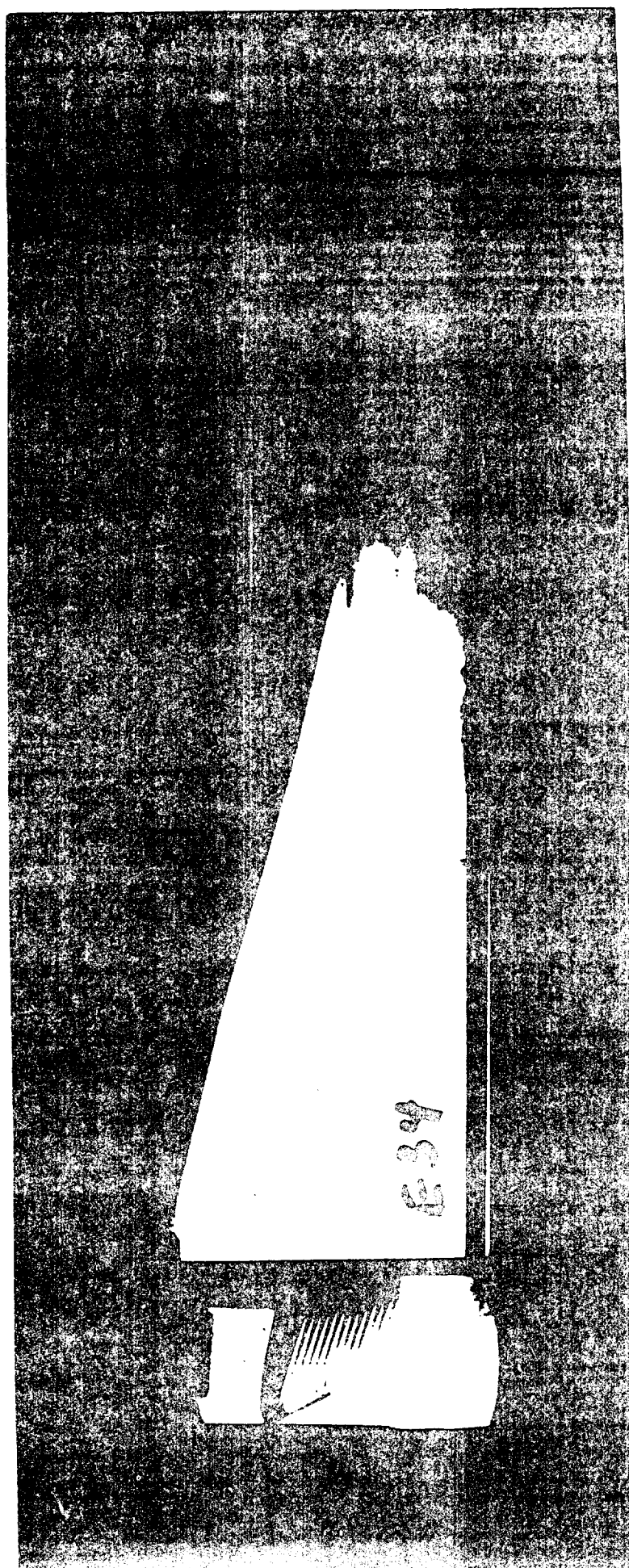


Figure 20. A Sample Streak Record from an Expanding Ring Experiment.

The plate impact tests were conducted with three objectives: (1) determination of Hugoniot Elastic Limit, (2) determination of the unloading path from the free surface velocity history, and (3) determination of the threshold conditions associated with onset of spall fracture.

Impact induces an elastic shock and a plastic shock in the target. The amplitude of the elastic shock is  $\sigma_{HEL}$ . The Hugoniot Elastic Limit,  $\sigma_{HEL}$ , is the maximum stress in the elastic regime for one-dimensional wave propagation. This stress level is generally treated as a material property, and above this level the material flows plastically. The stress  $\sigma_{HEL}$  can be determined from the experimentally obtained free surface velocity of the target that corresponds to the elastic shock velocity,  $u_{HEL}$

$$\sigma_{HEL} = 1/2 \rho C_L u_{HEL} \quad (4)$$

where  $C_L$  is the elastic sound speed in one-dimensional strain. The high strain rate yield strength  $Y_0$  can then be calculated from the relationship:

$$Y_0 = \frac{\sigma_{HEL}}{\left(\frac{K}{2G} + \frac{2}{3}\right)} \quad (5)$$

where  $G$  is the shear modulus and  $K$  is the bulk modulus.

#### 2.4.1 Results

Plate impact tests were conducted on W-2 tungsten, 1215 steel, 5083-0 aluminum, and Armco Iron. In addition, for precursor decay analysis, several additional plate impact tests on C1008 steel were conducted. Results in terms of  $\sigma_{HEL}$  and the spall stress for these metals are given in Table 4.

### 2.5 NEW EXPERIMENTAL TECHNIQUES

A number of new or improved techniques for high strain rate measurements were developed. These are described in detail in this section. Various applications are also discussed.

TABLE 4

## OBSERVED HEL AND SPALL THRESHOLDS FOR CRACK FORMATION

| Material           | HEL<br>(Kbar) * | Spall Threshold<br>Impact Velocity<br>(M/S) | Spall<br>Stress, $\sigma_s$<br>(kbar) |
|--------------------|-----------------|---|---------------------------------------|
| 1215<br>Steel      | 14.4+02         | 230   | 8.0 <sup>‡</sup>                      |
| W2<br>Tungsten     | 24.0            | 210   | 7.4                                   |
| 5083-0<br>Aluminum | 2.9             | 426   | 16.0                                  |

\* 1 Kbar = 14504 psi  
= 100 MPA  
=  $10^9$  dynes/cm<sup>2</sup>

<sup>‡</sup> Incipient spall; low spall strength because spall signal was due to precursor voids in the target.

### 2.5.1 Manganin Gauge Technique

Piezoresistive gauges have been used extensively during the past 20 years as in-material stress transducers in planar shock wave studies. Manganin and Ytterbium are the most popular among these transducers. Many workers determined calibration curves for manganin, in the 0-200 kb range, in terms of relative resistance change versus shock stress. These are reviewed in References 2, 16, and 17. There are two important difficulties with the use of piezoresistance stress gauges in dynamic experiments. First, there is the interpretation of data for loading conditions which differ from the standard calibration experiments. The most prominent example is the use of piezoresistive gauges to measure lateral stress in i-D experiments. A second difficulty arises from the appearance of a substantial resistive hysteresis in the gauge response upon unloading. For example, it can be shown that wire gauges should have a different response than foil gauges.

We used and refined a rather simple analytic elastoplastic model for the gauge response which is a direct continuation of the work [2]. The present approach is general and can be used for any piezoresistance gauge. However, manganin gauges are the only gauges for which we have a large amount of data so that most of this section deals with these gauges. Specifically we deal with three issues: (1) accounting for the differences between the various calibration curves for manganin gauges, (2) demonstrating the importance of the yield strength of the gauge material in determining its resistive hysteresis upon unloading and accounting for the higher response of annealed gauges, and (3) the response of transverse foil gauges which measure the lateral stresses in plane shock wave experiments.

The well-known logarithmic derivative of the electrical resistance of a conducting element having length  $\ell$ , cross section  $A$ , and resistivity  $\rho$  is given by:

$$R = \rho \frac{\ell}{A} \tag{6}$$

$$\frac{\Delta R}{R_0} = \frac{\Delta \rho}{\rho_0} + \frac{\Delta l}{l_0} - \frac{\Delta A}{A} = \frac{\Delta \rho}{\rho_0} - \epsilon_L + \epsilon_A$$

where  $\epsilon_L$ ,  $\epsilon_A$  are longitudinal (in the current direction) and cross-sectional strains, defined positive in compression. For the various configurations which one encounters in 1-D experiments, the gauge is emplaced so that its length, width, and thickness coincide with the three principal directions of the stress tensor which defines the shocked state. This point is very important because it means that the following analysis is not general enough to include cases where the gauge is emplaced in an arbitrary orientation relative to the shock front. Thus, in conventional plate impact test, shear stresses do not act on the gauge element.

The relative resistivity change can, in principle, depending on the plastic work done on the gauge through the lattice defects which are generated by the shock wave. These extra defects were considered, for some time, to be the main reason for the resistive hysteresis in manganin gauges. Recently, Chen et al. [18] found that for manganin these defects do not contribute significantly to the residual resistivity. This confirms the assumption in Reference 19 about the "mechanical" nature of the hysteresis in manganin rather than the extra defect explanation. For such a gauge element, which is aligned along the z direction, the general expression (see References 20 and 21) for the resistivity change, is given by

$$\begin{aligned} \frac{\Delta \rho}{\rho_0} &= \pi_{12} (\sigma_x + \sigma_y) + \pi_{11} \sigma_z \\ &= \pi_{12} 3p + (\pi_{11} - \pi_{12}) \sigma_z; \quad p = \frac{\sigma_x + \sigma_y + \sigma_z}{3} \end{aligned} \quad (7)$$

where  $\pi_{ij}$  are the well-known piezoresistance coefficients and  $\sigma_i$  are the principal stresses. The  $\pi_{44}$  term does not appear in Equation (7) because no shear stresses act on the gauge element. Figure 21 shows the position of the gauge element in relation to the shock front and the principal axes.



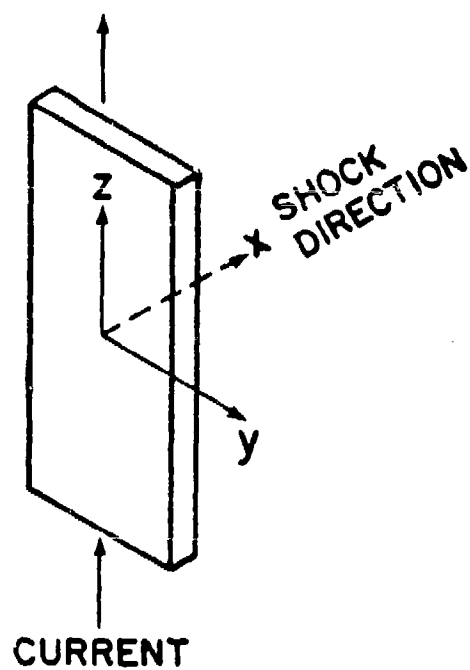


Figure 21 . The Principal Axes for a Longitudinal Stress Gauge.

We next decompose  $\sigma_z$  to its hydrostatic and deviatoric terms ( $\sigma_z = p + \sigma'_z$ ) and the following relations can be obtained:

$$\begin{aligned} \frac{\Delta \rho}{\rho_0} &= (\pi_{11} - \pi_{12}) (p + \sigma'_z) + 3\pi_{12} p \\ &= (\pi_{11} + 2\pi_{12})p + (\pi_{11} - \pi_{12}) \sigma'_z \\ &= \pi_{HS} \cdot p + \pi_{\text{shear}} \sigma'_z = \left( \frac{\Delta \rho}{\rho_0} \right)_{HS} + s e'_L, \end{aligned} \quad (8)$$

where  $e'_L$  is the elastic deviatoric strain along the current direction (z) and s is an empirical constant. The first term on the right-hand side depends only on the volumetric strain of the gauge  $\epsilon_v$  and can be determined from hydrostatic compression. The second term is a deviatoric contribution which is proportional to the deviatoric part of the elastic strain along the gauge length  $e'_L$ .

We now make the usual assumption that if the gauge element is much longer than both its width and thickness, then the strain,  $\epsilon_L$ , along the gauge length is zero. Since  $\epsilon_v = \epsilon_L + \epsilon_A$ , we get for the relative resistance change is:

$$\left( \frac{\Delta R}{R_0} \right) \epsilon_L = 0 = \left( \frac{\Delta \rho}{\rho_0} \right)_{HS} + s e'_L + \epsilon_v \quad (9)$$

This equation is the general result which shows that the response of piezoresistive gauges is mainly determined by the hydrodynamic pressure through the  $(\Delta \rho / \rho_0)_{HS}$  and  $\epsilon_v$  terms. The third term ( $s \cdot e'_L$ ) is a deviatoric one and its magnitude depends on the yield strength of the gauge.

In Reference 1, the method to obtain s for manganin by using the measured relative resistance changes under both hydrostatic and uniaxial strain conditions has been shown. We used the compression curve for manganin, as given in Reference 22:

$$p = 1160 \epsilon_v + 4120 \epsilon_v^2, \quad (10)$$

where  $p$  is the kbar. The most accepted values for the piezoresistance coefficient under hydrostatic conditions is  $2.4 \times 10^{-3}$   $(\Omega/\Omega)/\text{kb}$ . The 1-D coefficient found in Reference 23 for the elastic range of gauge response is  $1.95 \times 10^{-3}$   $(\Omega/\Omega)/\text{kb}$ . These values result in a value of  $s = 0.18$  for the empirical constant in Equation (9). Using this value together with the compression curve, (Equation (10)), we finally get for manganin:

$$\left(\frac{\Delta R}{R_0}\right)_{\epsilon_L = 0} = 3.45 (1 + 2.87\epsilon_V) \epsilon_V + 0.18\epsilon_L \quad (11)$$

The stress-time history can be obtained using the above calibration relationship.

The analysis presented above demonstrates the importance of the yield strength of the gauge material in determining its resistance change for given stress and strain conditions. We can clearly see how a high value of  $Y$  and especially one which increases with pressure, can affect the value of hydrodynamic pressure ( $p$ ) in the gauge element, which is the main factor in the gauge response. The importance of the yield strength can be further demonstrated by considering its influence on: (1) the resistive hysteresis of the gauge and (2) the response of annealed gauges. In the next subsections we elaborate on these issues. By observing these issues, in light of the elasto-plastic response of the gauge material, we get a better understanding of the dynamic loading process. These points are also discussed in Reference 2.

### 2.5.2 Transverse Gauge Technique

One of the most important issues in the study of dynamic behavior of solids under shock loading is the determination of the lateral stress in the shocked specimen. The only direct technique for such a measurement uses thin piezoresistance stress gauges which are inserted laterally in the shocked target as shown schematically in Figure 22.

In Reference 2 past work on direct measurement of lateral stress with piezoresistive gauges has been reviewed. The

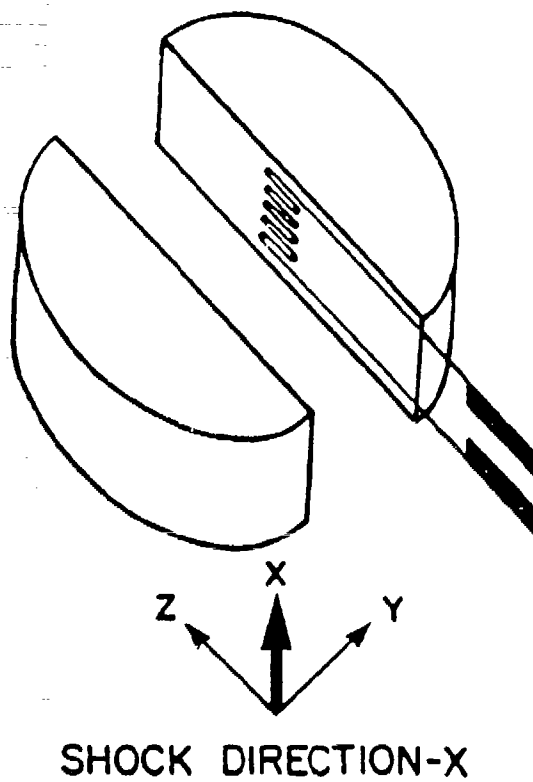


Figure 22 . The Principal Stresses for a Transverse Stress Gauge.

approach used in this program is based on that work. Our technique is also described in Reference 24.

In order to develop an analytical calibration for the transverse gauge, the stress across the thickness of the gauge is assumed to be equal to the lateral stress in the target -  $\sigma_y$ . This assumption is actually the basic one behind the lateral stress measurement technique with piezoresistive gauges, and it is justified for very thin (foil) gauges. It is also assumed that the strain in the gauge along the shock direction is the same as the uniaxial strain in the surrounding specimen -  $\epsilon_x$ . This means that the width of the gauge is decreased by  $\epsilon_x$  (the gauge is bonded perfectly to the specimen). To justify this perfect bonding assumption, it is best to refer to a related work in which we have shown that a thin wire, or foil, which is placed longitudinally in the target (along shock propagation direction) undergoes the same strain as its surroundings.

The next step is to realize that the elastic constants of the gauge and matrix can be very different (as in the case of manganin in PMMA). Thus the assumption of equal  $\epsilon_x$  means that the stress in the gauge along its width ( $\sigma_x$ ) may be very large. This can easily be seen if we write the elastic expression for  $\sigma_x$ :

$$\sigma_x = (K - \frac{2}{3}G) \epsilon_v + 2G\epsilon_x \quad (12)$$

where  $\epsilon_v$  is the volumetric strain of the gauge and K and G are its bulk and shear moduli, respectively. Thus, the relatively large strains in shock-loaded PMMA (about 1 percent per kbar) will result in very large stresses in the manganin gauge because of the  $2G\epsilon_x$  term ( $2G = 870$  kbar; see Reference 22). This means that the elastic behavior of the transverse gauge can be confined to a very small stress range. For manganin in PMMA this range is limited to shock stresses of less than about 0.5 kbar. The values that  $\sigma_x$  can take are then determined by the value of  $\sigma_y$  and the yield criterion of the gauge material. Assuming a Von-Mises (or Tresca) yield criterion, we thus write for  $\sigma_x$  in the gauge:

$$\sigma_x = \sigma_y + Y \quad (13)$$

where  $Y$  is the yield strength of the gauge material.

There remains the question of the magnitude of the third stress component along the gauge length -  $\sigma_z$ . Since this is the largest dimension of the gauge we may assume, as do others, that the strain along this direction is zero. As for the stress along the  $z$ -axis we assume that it is equal to  $\sigma_y$  in the gauge. This assumption can have some justification if we consider the calculations of Gupta [25] which show that the two lateral stresses in the gauge ( $\sigma_y$  and  $\sigma_z$ ) are nearly equal.

Thus the stress and strain tensors which describe the transverse gauge are:

$$\sigma_{ij} = \begin{pmatrix} (\sigma_y + Y) & 0 & 0 \\ 0 & \sigma_y & 0 \\ 0 & 0 & \sigma_y \end{pmatrix}, \quad (14)$$

$$\epsilon_{ij} = \begin{pmatrix} \epsilon_x & 0 & 0 \\ 0 & (\epsilon_v - \epsilon_x) & 0 \\ 0 & 0 & 0 \end{pmatrix}.$$

We note here that because  $\epsilon_x$  can be much larger than  $\epsilon_v$  (as in the case of manganin in PMMA) the value of the strain through the thickness of the gauge ( $\epsilon_y$ ) can be negative. Thus the thickness of the transverse gauge can increase under shock compression. This is also what Gupta [25] found in his calculations for Ytterbium in PMMA.

After having the principal stress in the gauge, we can write an expression for the hydrostatic pressure which prevails in it:

$$P = \frac{\sigma_x + \sigma_y + \sigma_z}{3} = \sigma_y + \frac{1}{3} Y \quad (15)$$

The next step is to consider the calibration curve of the piezoresistive gauge in terms of its relative resistance change versus its volumetric strain ( $\epsilon_v$ ) as in Equation (11) for manganin. This curve can also be given by the hydrostatic pressure in the gauge with the aid of the dynamic compression curve of the gauge  $P = f(\epsilon_v)$  as in Equation (10). Thus:

$$\frac{\Delta R}{R_0} = f(\epsilon_v) = g(P), \quad (16)$$

where  $\Delta R/R_0$  is the relative resistance change of the gauge.

For manganin it was found (see Reference 21) that Equation (16) takes the form given by Equation (11). Thus  $\epsilon_v$  is given by solving this quadratic relation:

$$\epsilon_v = -0.1774 + \sqrt{0.03042 + \frac{\Delta}{9.89}} \quad (17)$$

where  $\Delta = \Delta R/R_0$ .

The data reduction process involves only two steps. First, use the measured  $\Delta$  value in Equation (17) to obtain the value of  $\epsilon_v$ . Then use  $\epsilon_v$  in Equation (10) to obtain the value of the pressure in the gauge ( $P$ ). The second step is to use this value of  $P$  in Equation (15) to get the value of  $\sigma_y$ . In order to allow for the changes of  $Y$  with peak pressure we use the  $Y = Y(P)$  curve in Reference 26.

### 2.5.3 High Pressure Measurements

The direct determination of rarefaction wave velocities in shock-loaded solids is important for high-pressure equation of state data. Various experimental techniques have been attempted in the past 20 years, and these are summarized in Reference 27. Currently, the most widely used technique employs optical flash gaps. This technique has since been used to measure longitudinal wave velocities for a variety of shocked materials. In this technique, a relatively thin flyer plate strikes a stepped target plate. The time duration ( $\Delta t$ ) of the shock level at each step is recorded. This is done by backing the stepped target with transparent materials which emit large amounts of thermal radiation

(when shocked) and using optical analyzers to record these radiation versus time histories. From the different time durations versus the position of the optical analyzer (step thickness) one then determines the catch-up ratio (R). This is the ratio of target to flyer thickness where the release wave from the flyer's back face overtakes the shock wave in the target. The longitudinal sound velocity (the leading edge of the rarefaction fan) is given by

$$C = \frac{\rho_0}{\rho} U_s \frac{R + 1}{R - 1} \quad (18)$$

where  $\rho_0$  and  $\rho$  are initial and shock-compressed densities of the specimen and  $U_s$  is its shock velocity.

The optical technique has several disadvantages for use at the University. It requires extremely sensitive or fast optical recording apparatus, intricate target fabrication, and use of noxious gasses. Therefore, a new technique was developed using manganin gauges as the time-of-arrival sensors (Reference 28). The experimental configuration is shown schematically in Figure 23. A thin flyer plate impacts a stepped target plate. At the center of each step is placed a thin (5  $\mu\text{m}$  thick) manganin stress gauge backed by a thick epoxy disk. For metallic targets, a thin Mylar sheet (10-25  $\mu\text{m}$ ) is placed between the gauge and the target. All these elements (Mylar sheet, gauge, and epoxy disk) are then bonded together and to the target with epoxy under a press in order to minimize bond thickness and air bubbles. Thus, the gauge is surrounded by a uniform material (epoxy) and is close enough to the interface to measure the stress-time history there. By embedding the gauge in plastic, we greatly improve its time resolution, which is determined by the gauge thickness and is of the order of a few nanoseconds.

There is another advantage to the backface over the in-material configuration which is very important for the present application. The embedded gauge is limited to shock stresses of 200 kb or so. This is so because most polymers (epoxy and Mylar



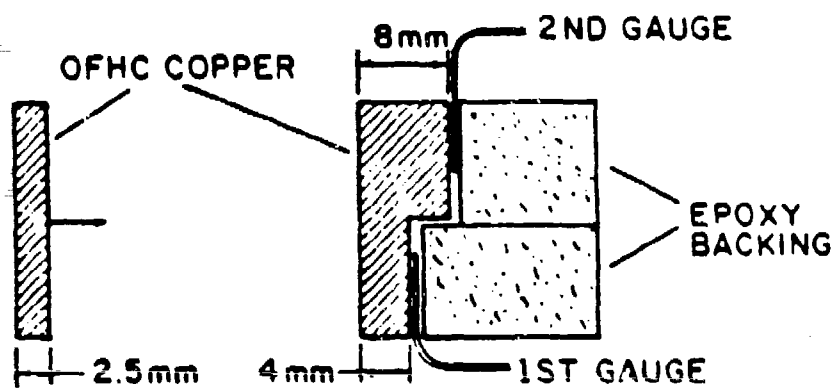


Figure 23. Schematic Representation of the Impact Configuration.

included) become electrically conducting at these pressures and they short circuit the gauge and its leads. With the backface configuration the stresses in the specimen can be very high (of the order of megabar) before the stresses in the epoxy backing reach 200 kb. This is especially true for materials with high acoustic impedances (like copper, steels, tungsten, etc.).

Thus, the backface configuration for manganin gauges is most appropriate for catch-up ratio determination because it overcomes the two difficulties of the in-material gauge configuration (long rise times and limited stress range). Manganin gauges have two advantages over the optical analyzers as stress-time sensors. First of all, they are much simpler to use and their experimental assembly involves fewer components and is less time consuming. Second, they are calibrated for the entire stress range of 0-200 kb both under loading and unloading conditions. This enables us to identify the arrival of other release waves with much more certainty than with the optical analyzers. Moreover, from the measured stress-time history at the specimen-epoxy interface we can determine the spall strength of the target.

In order to demonstrate the usefulness of manganin gauges as time-of-arrival sensors we performed a few symmetric plate impact experiments with OFHC copper flyers and targets. Gauges were used as described in Section 2.5.1. Their main use in the present study is as time-of-arrival gauges. Details of these experiments can be found in Reference 28.

Figure 24 shows the extrapolation of the  $\Delta t$  vs gauge location points to obtain the catch-up distance for this shot. The impact velocity was 1042 m/s. The value of 15.8 mm corresponds to a catch-up ratio of  $R = 6.15$  (flyer thickness was 2.57 mm). This value together with the measured shock velocity of  $U_s = 4.65$  mm/ $\mu$ s are then inserted in Equation (18) to give a value of  $C_L = 5.73$  mm/ $\mu$ s for the longitudinal sound speed of copper compressed to 220 kb. This value is in excellent agreement with the value of 5.7 mm/ $\mu$ s obtained by Morris et al. [29]. The details of the tests on 1215 steel are summarized in Table 5.

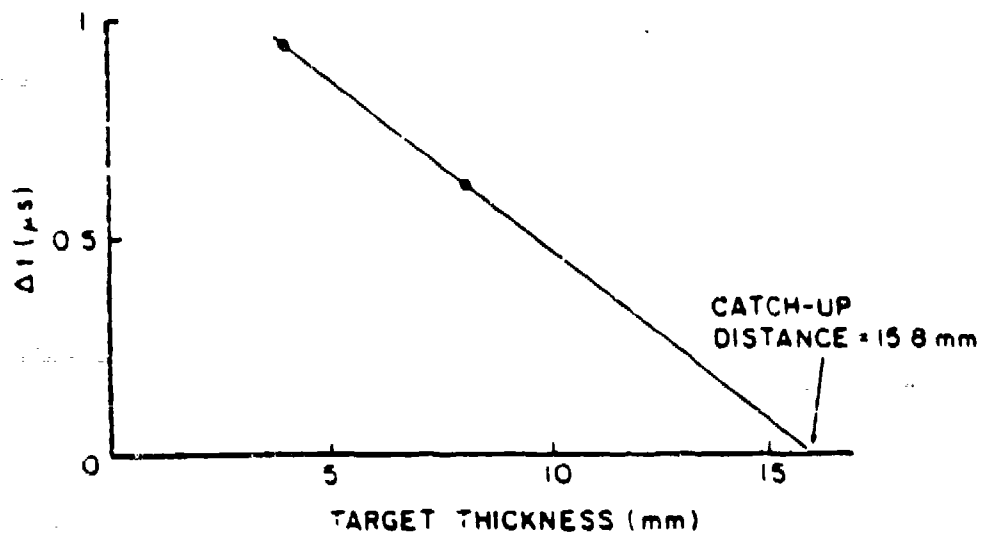


Figure 24. Linear Extrapolation to Find the Catch-up Distance.

TABLE 5  
SUMMARY OF THE RESULTS ON 1215 STEEL

A. IN MATERIAL GAUGE CONFIGURATION; IMPACTOR - 1215 STEEL

| Shot No. | Impactor Thickness (mm) | Impactor Velocity (m/s) | Target PMMA (mm) | Shock Stress (kbar) |
|----------|-------------------------|-------------------------|------------------|---------------------|
| 7-1027   | 10.2                    | 313                     | 6+6              | 51±2                |
| 7-1028   | 10.2                    | 446                     | 6+6              | 87±3                |
| 7-1039   | 9.52                    | 719                     | 6.35+6.35        | 136±3               |
| 7-1040   | 9.52                    | 870                     | 6.35+6.35        | 164±3               |
| 7-1041   | 9.52                    | 1216                    | 6.35+6.35        | 222±5               |

B. BACK GAUGE CONFIGURATION; IMPACTOR - 1215 STEEL

|        |      |      |     |       |
|--------|------|------|-----|-------|
| 7-1015 | 2.54 | 231  | 4+8 | 46±2  |
| 7-1029 | 2.54 | 901  | 4+8 | 160±5 |
| 7-1000 | 2.54 | 1013 | 4+8 | 179±5 |
| 7-1006 | 2.54 | 1326 | 4+8 | 238±5 |
| 7-1020 | 4.0  | 1661 | 4+8 | 304±5 |
| 7-1051 | 4.0  | 1000 | 8.0 | 177±5 |
| 7-1052 | 4.0  | 1490 | 8.0 |       |

#### 2.5.4 Shear Wave Measurements

Detection of shear waves is one of the more difficult problems in shock wave diagnostics. During this program, we developed a shear wave generation technique, and showed that manganin gauges could be used to detect shear wave arrivals [30].

A piezoresistance gauge was used. It was calibrated under both pressure and shear conditions, in order to have a quantitative measurement of both the compressional and shear wave amplitudes. In addition, the time of arrival of the shear wave at the gauge location can be used to measure the pressure dependence of the shear wave velocity, since this wave follows the faster compressional wave. One should emphasize that at present, the use of piezoresistance gauges in shock wave studies is limited to the more simple one-dimensional configuration. In this configuration, there are no shear stresses acting on the gauge and the only relevant component of the stress tensor is that along the shock propagation direction. This stress component in the gauge element is equal to that in the target, thus, enabling the measurement of shock stresses. In order to use a piezoresistive element of the measurement of a shear stress component, one has to use a gauge which has been calibrated under pure shear conditions. We demonstrated the feasibility of this technique by an oblique-impact experiment with a manganin gauge embedded in an alumina target. The experimental assembly is shown in Figure 25.

The piezoresistance element should ideally have a large and well-calibrated shear coefficient. Polycrystalline solids have a single direct shear piezoresistant coefficient which is term  $\pi_{44}$ . The gauge should also have a well-calibrated pressure coefficient in order to measure the compressional wave amplitude directly. The proper gauge should be embedded between two specimen disks in the same way as regular piezoresistance gauges are installed in plate-impact experiments. Gupta's technique [25] to embed the gauge in very small grooves in the target, without using epoxy and relying only on the friction between the two disks, might prove advantageous here.

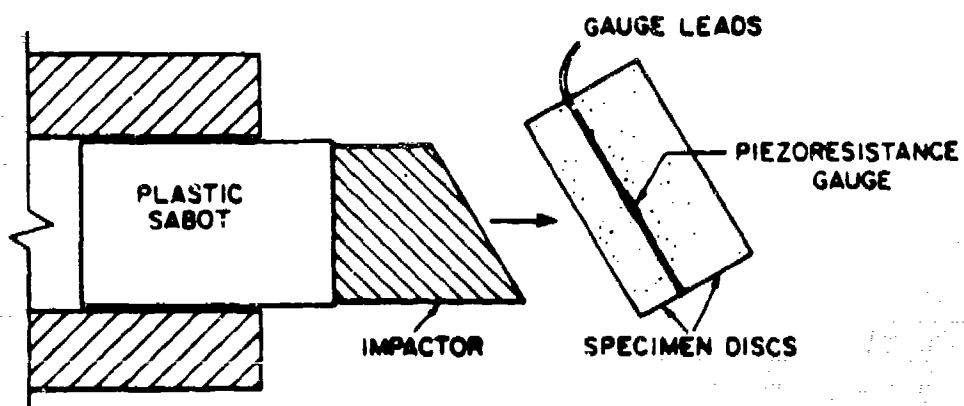


Figure 25. A Schematic Representation of an Oblique-Impact Experiment with a Piezoresistance Gage.

When the oblique impactor hits the target, it generates two waves which propagate away from the impact face. The first is the usual uniaxial-strain compressional wave. It will be recorded by the gauge as described in Section 2.5.1. The slower shear wave, moving in an already compressed material will cause an additional resistance change for the gauge at some later time (depending on the shear wave velocity). The resistance change will either increase or decrease the current resistance of the gauge, depending on the sign of  $\pi_{44}$ . If  $\pi_{44}$  is large enough, this additional resistance change can be used to accurately measure the amplitude of the shear wave. The arrival time of the shear wave can be used to measure the pressure dependence of its velocity. This can then be used to determine the pressure dependence of the shear modulus of the target material which is an important parameter for various applications.

The advantage of the proposed technique is that with a single gauge, both the compressional and shear wave profile can be directly determined. Thus, the effects of shear-related dynamic processes, like phase transformation and spall, can be studied more closely by varying the amount of shear continuously. A drawback to the proposed technique is that at the present time (to our knowledge) no piezoresistance gauge commonly used in shock experiments, has been calibrated for shear response. Our guess is that of the two most commonly used gauges, manganin and ytterbium, the latter will be more adequate for shear measurements because it has much higher-pressure coefficient ( $\pi_{11}$  and  $\pi_{12}$ ). The only shear gauges we know of are those manufactured by Kullite Semiconductors Inc. which are made of p-type silicon. These gauges are evaporated on glass and alumina substrates and they might be used to measure shear waves in these materials. However, their shear piezoresistivity will probably be influenced by both the pressure and temperature rise which result from the leading compressional wave. Thus, more calibration work has to be done on these gauges before they can be used for quantitative measurements in shock wave experiments.

The problem of gauge slippage because of weak epoxy bonding between two solid specimen disks has to be carefully analyzed and one should use the various techniques which have been developed for the prevention of such slippage. The two most promising one are (1) the use of alumina-filled epoxy and (2) embedding the gauge in precisely prepared grooves in the target, without using epoxy and relying on the friction between the disks. The problem of the epoxy failure to transmit high shear stresses is absent if one is using liquid specimens. Thus, it could be very advantageous to perform oblique impact experiments on liquids and measure the shear stresses in these materials.

In order to check the feasibility of the proposed technique, an oblique-impact experiment was performed with the 50 mm gas gun of the University of Dayton Research Institute. This gun does not have a keyway arrangement for oblique impact experiments. Thus, in order to achieve a reasonable planarity of the impact, a few shots were conducted in which it was determined that the amount of rotation the projectile experiences during launch was about  $3^\circ$ . Henceforth, we place the projectile in a position rotated by the same amount. A check for this compensation is obtained by observing the rise time of the compressional wave as recorded by the gauge. Although the compensation was not perfect, the rise times were good enough for a qualitative evaluation of the technique.

Next a commercial manganin gauge was placed between two 98 percent pure alumina disks. This material had a density of 3.75 g/cc and a longitudinal sound velocity of  $C_L = 10.4 \text{ mm}/\mu\text{s}$ . Based on past work the target response should be elastic. The thickness of the first disk was 13.7 mm so that the compression and shear waves should have a large separation between their arrivals at the gauge location. The impactor was a thick copper disk, wedge shaped as shown in Figure 25, and the angle of obliquity was  $15^\circ$ . The impact velocity in this experiment was 210 m/s. Using these values, together with an estimated shear wave velocity of 6 mm/ $\mu\text{s}$ , the shear generated at the impact face should be  $\tau \approx 5 \text{ kbar}$ . According to Reference 31, this shear stress is larger than the



maximum shear that a thin layer of epoxy can transmit dynamically ( $\approx 3\text{kb}$ ). However, the intent was not to measure the shear stress amplitude, but rather to record its arrival at gauge location.

The gauge record in this experiment is shown in Figure 26. It can be clearly seen that the arrival of two waves at the gauge location occurs with a separation of about  $1.2\ \mu\text{s}$ . The rise time of the first wave is relatively large, a constant stress plateau is not observed and the peak stress is less than the predicted stress, as calculated from the impact parameters. Nevertheless, the detection of two separate waves reaching the gauge plane is unambiguous. Using the measured value of  $C_L = 10.4\ \text{mm}/\mu\text{s}$  (with ultrasonic techniques) and the time interval between the waves we get a value of  $C_S = 5.44$  for the shear wave velocity. This value is within the range of values for various alumina specimens, as given by Coors, with a range from  $5.06$  to  $6.38\ \text{mm}/\mu\text{s}$ .

The relatively large apparent shear wave amplitude does not necessarily mean that the  $\pi_{44}$  coefficient of manganin is large. The more probable explanation is that the epoxy layer between the two alumina disks could not transmit the large shear stress (of  $5\ \text{kb}$ ) and it slipped, causing the gauge to elongate and its resistance to increase. This can be verified by performing more experiments with lower shear stresses and with gauges oriented differently. These different orientations will result in different elongations when slippage occurs, thus, different resistance changes.

In summary, we have proposed to use piezoresistance gauges to monitor both compression and shear waves in oblique-impact experiments. The first step is to identify and statically calibrate suitable gauge materials that possess large shear piezoresistance coefficients. The second step is to embed these gauges in well-defined elastic solids, like ceramics, in order to demonstrate their performance and check their static calibration. After these two steps, they can be embedded in any specimen using strong epoxy adhesive (as suggested in Ref. 3i) or the fine grooving technique which was used in Ref. 8. We suggest Ytterbium

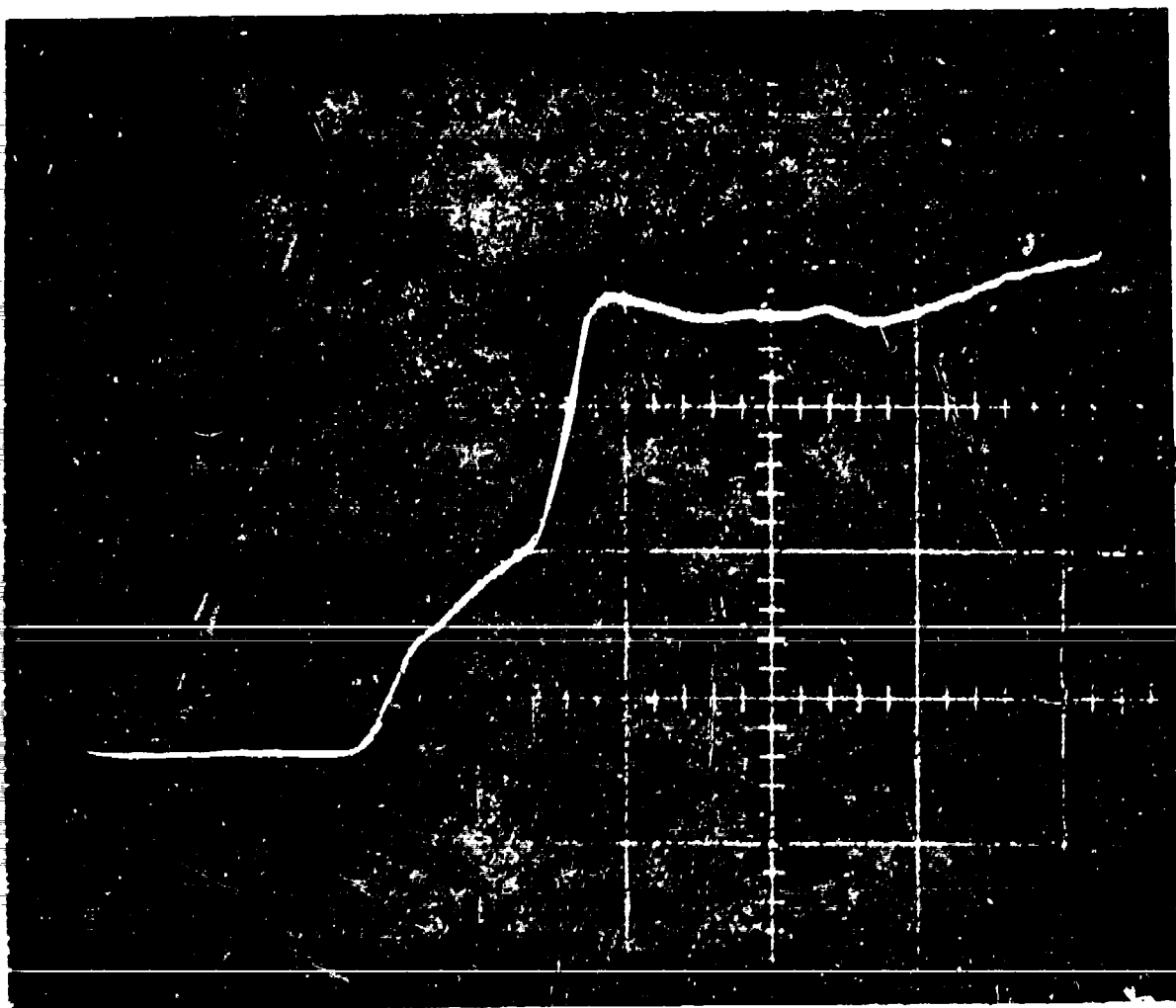


Figure 26. Manganin Gage Record from the Oblique-Impact Experiment. [Note the arrival of the two waves. (0.5 V/div; 1 $\mu$ s/div.)]

gauges because this material has large  $\pi_{11}$  and  $\pi_{12}$  coefficients and it may have a large  $\pi_{44}$  coefficient. The experiments should be performed in a properly keyed gun for good planarity of the impact.

## SECTION III

### ANALYTICAL MODELING

Elementary constitutive models relate stress to strain and are generally independent of loading rate and load history. While these are easy to use, they are not accurate for many metals under load cycles of engineering importance. In particular, numerical simulations of projectile penetration and explosive forming require more accurate constitutive models than are usually available. Rate-dependency is taken into account by overstress concept based viscoplastic models, for example, those of Perzyna [32] and Malvern [33]. However, these models do not consider loading history. A state variable based viscoplastic model must be employed in order to describe both rate- and history-dependent behavior.

The state variable model of Bodner and Partom [34] (B-P) has many attractive features: (1) ability to model a broad range of load histories, (2) ease of determination of parameter values, and (3) adaptability to finite difference and finite element computer codes. This model has been successfully used by various investigators to describe several structural alloys under cyclic and time dependent loading conditions. The strain rates involved in those studies were between  $10^{-6}$  and  $10^{-2} \text{ s}^{-1}$ . The present work reports the successful application of the B-P model to material behavior at high strain rates ( $>100 \text{ s}^{-1}$ ). A unique algorithm was developed to evaluate the model parameters from experimental data.

Details of the modeling technique have been presented in an earlier report [1]. For completeness, we describe briefly the Bodner-Partom model and the model parameter evaluation scheme. We also used the model to describe high temperature SHB test results. The following section discusses these various results.

#### 3.1 BODNER-PARTOM MODEL

We present the major features here, as well as an extension of the model for extreme work hardening materials, as proposed earlier by Bodner et al. [35].

The total strain rate is assumed to be decomposable into elastic and inelastic components.

$$\dot{\epsilon}_{ij} = \dot{\epsilon}_{ij}^e + \dot{\epsilon}_{ij}^p \quad (19)$$

Both are nonzero for all loading/unloading conditions. The elastic strain rate is related to the stress rate by the elastic constants (Hooke's Law). The inelastic strain rate is assumed to be a function of stress,  $\sigma_{ij}$ , a state variable,  $Z$ , and to follow the Prandtl-Reuss flow rule

$$\dot{\epsilon}_{ij}^p = \dot{\epsilon}_{ij}^p = \lambda S_{ij} \quad (20)$$

where  $\dot{\epsilon}_{ij}^p$  and  $S_{ij}$  are the deviatoric plastic strain rate and stress, respectively. Squaring Equation (20) gives

$$D_2^p = \lambda^2 J_2 \quad (21)$$

where  $D_2^p$  is the second invariant of the plastic strain rate and  $J_2$  is the second invariant of the stress deviator.

$$D_2^p = D_0^2 \exp\left[-\left(\frac{Z^2}{3J_2}\right)^n \left(\frac{n+1}{n}\right)\right] \quad (22)$$

where  $D_0$  is the limiting value of the plastic strain rate in shear, and  $n$  is a parameter that is mainly related to strain rate sensitivity.  $Z$  is a measure of the overall resistance of the material to plastic flow, and it depends on the loading history.

The plastic strain rate can be expressed in the following form by regrouping Equations (20)-(22)

$$\dot{\epsilon}_{ij}^p = D_0 \exp\left[-\frac{n+1}{2n} \left(\frac{Z^2}{3J_2}\right)^n\right] \frac{S_{ij}}{\sqrt{J_2}} \quad (23)$$

It is assumed that  $Z$  is a function of the plastic work,  $W_p$ :

$$\dot{Z} = m (Z_1 - Z) \dot{W}_p \quad (24)$$

Integration of this equation will lead to:

$$Z = Z_1 - (Z_1 - Z_0) e^{-mW_p} \quad (25)$$

where  $\dot{W}_p = \sigma_{ij} \dot{\epsilon}_{ij}^p$ .  $Z_0$  is the initial value of  $Z$ ,  $Z_1$  is the maximum value that  $Z$  can attain, and  $m$  is a parameter that describes the strain hardening behavior of the material.

To describe extreme strain hardening material behavior,  $m$  can be assumed to take the following form:

$$m = m_0 + m_1 e^{-\alpha W_p} \quad (26)$$

The expression for  $Z$  is obtained by combining Equations (24) and (26) and integrating,

$$Z = Z_1 - (Z_1 - Z_0) e^{-m_0 W_p} e^{-\frac{(m_0 + m_1 - m)}{\alpha}} \quad (27)$$

The additional constants,  $m_0$  and  $m_1$ , replaces the original 'm'. We also need ' $\alpha$ ' to model extreme strain hardening behavior of material like annealed OFHC copper.

The effect of temperature on the flow stress is included through the parameter  $n$ . Based on experimental evidence, it is assumed to vary as an inverse function of absolute temperature ( $T$ ):

$$n = A + \frac{B}{T} \quad (28)$$

where  $A$  and  $B$  are model parameters and  $T$  is expressed in degrees Kelvin. Thus the B-P model contains five principal material parameters  $D_0$ ,  $Z_0$ ,  $Z_1$ ,  $m$ , and  $n$  that have to be evaluated from high strain-rate experiments under room temperature for a material with negligible strain hardening. For a strain hardening material, the number of constants is increased by two, with  $m$  being replaced by

$m_0$ ,  $m_1$ , and  $\alpha$ . However, to extend the model to elevated temperature, we need to express  $n$  through the additional parameters  $A$  and  $B$ .

### 3.2 IMPLEMENTATION INTO STEALTH CODE

In most general purpose finite difference codes, the plastic flow is described by rate independent, Von Mises-yield-criterion-based, models. For instance, in the STEALTH [36] finite difference code that we used in our study, the stress deviators  $S_{ij}$  are estimated based on the elastic material behavior at the end of each time step. The effective stress,  $\sigma_{eff}$ , is estimated using:

$\sigma_{eff} = \sqrt{3/2} S_{ij} S_{ij}$ .  $\sigma_{eff}$  is then compared with the constant yield stress,  $Y_0$  which is an input into the code. When  $\sigma_{eff}$  exceeds  $Y_0$ , the stress deviators are brought back to the yield surface by a scaling factor.

The current algorithm to describe the B-P model requires an iterative scheme. The plastic strain rates in Equation (23) are calculated initially based on the elastic stress deviators. Since the total strain-rates are known at the beginning of each global time step of the finite difference solution scheme, we can compute  $\dot{\epsilon}_{ij}^e$  based on the initial estimate of  $\dot{\epsilon}_{ij}^p$ . Using Hooke's law, the stress rates  $\dot{\sigma}_{ij}$  are estimated. We can now estimate  $\dot{S}_{ij}$  based on the  $\dot{\sigma}_{ij}$ . With the improved values of  $S_{ij}$ , the plastic strain rates are again calculated. This procedure is continued until the values of  $\dot{S}_{ij}$  computed for the two successive iterations converged to the same values within the tolerant limits. We introduced a sub-incremental time stepping scheme during the iterations. The global time is further divided into small steps. The solutions converged within 2 or 3 iterations. Rajendran and Grove [37] have discussed this technique in detail.

### 3.3 ESTIMATION OF B-P PARAMETERS

There are seven B-P parameters,  $D_0$ ,  $n$ ,  $m_0$ ,  $m_1$ ,  $\alpha$ ,  $Z_0$  and  $Z_1$ . Rajendran et al. described the estimation scheme in detail in Reference 38. For completeness, a brief summary of the scheme that

was employed in determining these parameters is given in this section.  $D_0$  in the model is the maximum strain rate which the material can experience; it was arbitrarily set at  $10^8 \text{ s}^{-1}$ . The parameters  $n$ ,  $Z_0$ ,  $Z_1$  and  $m_0$  were first estimated from tensile SHB data, and then modified to be consistent with both the SHB test and the plate impact data. The parameter  $m_1$  was initially assumed to be zero, and only in the case of OFHC copper [1,26] does it have a nonzero value.

A series of interactive automated computer programs was developed to carry out the evaluation procedure. A program called BPSOLVE [39] was written to generate uniaxial stress loading curves. The program was used to estimate  $n$ ,  $m_0$ ,  $Z_0$  and  $Z_1$  from the SHB tension test results. Next, STEALTH was used to simulate plate impact tests; usually the value of  $n$  was adjusted to match the yield behavior. The SHB tests were resimulated with the new value of  $n$ , and the other parameters were adjusted interactively. If necessary, further refinements in  $n$  were then made to maintain adequate agreement with the plate impact data.

Since the temperature dependence is modeled through the parameter  $n$ , the other parameter values were assumed to be the same under elevated temperatures. Several SHB tests were conducted at different temperatures. Using BPSOLVE, the value of  $n$  corresponding to each temperature was determined. We then constructed an  $n$  vs.  $1/T$  plot. From this plot,  $A$  and  $B$  were determined.

We also present the new Bodner model [40] which has been used in our study to describe OFHC copper. The following section very briefly discusses the one-dimensional version of this model.

### 3.4 BODNER MODEL FOR DIRECTIONAL HARDENING

In this model, the state variable  $Z$  is assumed to be made up of both isotropic and directional components,

$$Z = Z^I + Z^D \quad (29)$$

The evolution equation for  $Z^I$  is given by:



$$\dot{Z}^I = m_1 (Z_1 - Z^I) \dot{W}_p \quad (30)$$

with the initial condition,  $Z^I(0) = Z_0$ ,  $Z_1$  is the limiting (saturation) value of  $Z^I$ ,  $m_1$  is the hardening rate. The expression for  $Z^D$  is given by:

$$Z^D = \beta_{ij} u_{ij} \quad (31)$$

where  $u_{ij}$  are the direction cosines of the current stress state. Under uniaxial stress state,

$Z^D = \beta \frac{\sigma}{|\sigma|}$  where  $|\sigma|$  is the absolute value of  $\sigma$ . The evolution equation for  $\beta$  is,

$$\dot{\beta} = m_2 (Z_3 \frac{\sigma}{|\sigma|} - \beta) \dot{W}_p \quad (32)$$

This new Bodner model assumes a simplistic plastic strain-rate equation as:

$$\dot{\epsilon}^p = \frac{2}{\sqrt{3}} D_0 e^{-\frac{1}{2}(\frac{Z}{\sigma})^{2n}} \quad (33)$$

The term  $(n+1/n)$  that appeared in Equation (22) of the B-P model is not used in the new formulation. This model has the same number of parameters as the B-P model for high strain hardening materials, as in the case of OFHC copper. The parameters are:  $D_0$ ,  $n$ ,  $m_1$ ,  $m_2$ ,  $Z_0$ ,  $Z_1$  and  $Z_3$ . We used this model to describe the annealed OFHC copper. The SHB test results reported in Reference 1 were used in the modeling efforts.

### 3.5 MODEL PARAMETERS

We reported the B-P model parameters for 1020, C1008, HY100 steels, OFHC copper and 7039-T64 aluminum in an earlier report [1]. In addition to these five materials, we determined model parameters for 6061-T6 aluminum, Nickel 200, W-2 Tungsten, and Armco Iron. We also extended the model parameters for C1008 steel to include

TABLE 6  
BODNER-PARTOM PARAMETERS

| MATERIAL                               | $Z_0$<br>(kbar) | $Z_1$<br>(kbar) | $n^*$ | $m$<br>(kbar <sup>-1</sup> ) | A     | B       |
|--|-----------------|-----------------|-------|------------------------------|-------|---------|
| C1008 Steel                            | 55              | 70              | 0.4   | 1.5                          | 0.245 | 46      |
| HY100 Steel                            | 24              | 35.5            | 1.2   | 1                            | -     | -       |
| 1020 Steel                             | 6.4             | 9.3             | 4.0   | 3.0                          | -     | -       |
| 6061-T6<br>Aluminum                    | 4.5             | 5.5             | 4.0   | 12.0                         | -2.86 | 2343.24 |
| 6039-T64<br>Aluminum                   | 5.6             | 7.6             | 4.0   | 2.8                          | -     | -       |
| Nickel 200                             | 3.2             | 8.2             | 4.0   | 4.0                          | -     | -       |
| W <sub>2</sub> - Tungsten              | 87.5            | 100.0           | 0.578 | 15.0                         | 0.166 | 134.3   |
| Armco Iron                             | 26.46           | 42.00           | 0.58  | 5.65                         | -     | -       |
| OFHC Copper <sup>†</sup><br>(annealed) | 8.0             | 65.5            | 0.4   | 1.4                          |       |         |

\* For high temperatures, value for n is calculated based on  
 $n = A + B/T$ .

† Two additional constants for OFHC copper are:  $m_1 = 15 \text{ kbar}^{-1}$  and  
 $\alpha = 150 \text{ kbar}^{-1}$ .

temperature effects. An attempt was also made to improve the modeling of OFHC copper through the new Bodner model which considers directional hardening effects. Table 6 provides the B-P model parameters for the various metals. The model simulations of SHB and plate impact results are shown in Figures 27-35. It can be seen from these figures that the model reproduced the experimental data extremely well.

### 3.5.1 Improved Model for OFHC Copper

Figure 36 shows the SHB test data at  $\dot{\epsilon} = 1100\text{s}^{-1}$ , and the corresponding simulation of B-P model. The model simulated the test results reasonably well. However, the unrealistic shape (between points A and B in Figure 36) of the simulated curve indicates the inadequacy of B-P model to handle large strain hardening behavior.

Analysis (see Reference 1) of the B-P model equations showed that this inadequacy cannot be eliminated due to the B-P model formulation based on plastic work. We attempted to model OFHC copper using the new Bodner model. The model parameters were obtained using the BPSOLVE program. It required a slight modification of BPSOLVE. The corresponding constants are given in Table 7.

TABLE 7  
BODNER MODEL PARAMETERS

| n    | $m_1$<br>(kbar <sup>-1</sup> ) | $m_2$<br>(kbar <sup>-1</sup> ) | $Z_0$<br>(kbar) | $Z_1$<br>(kbar) | $Z_3$<br>(kbar) |
|------|--------------------------------|--------------------------------|-----------------|-----------------|-----------------|
| 0.34 | 2.1                            | 150                            | 10              | 370             | 110             |

Figure 37, shows the actual SHB test results with the B-P model and Bodner model simulations. It can be seen from the Figures 38-39 that the concavities in the simulated stress-strain curves at three different strain rates could not be eliminated even with the new model. The model simulations are also separately plotted in these figures. The concavity is not that much

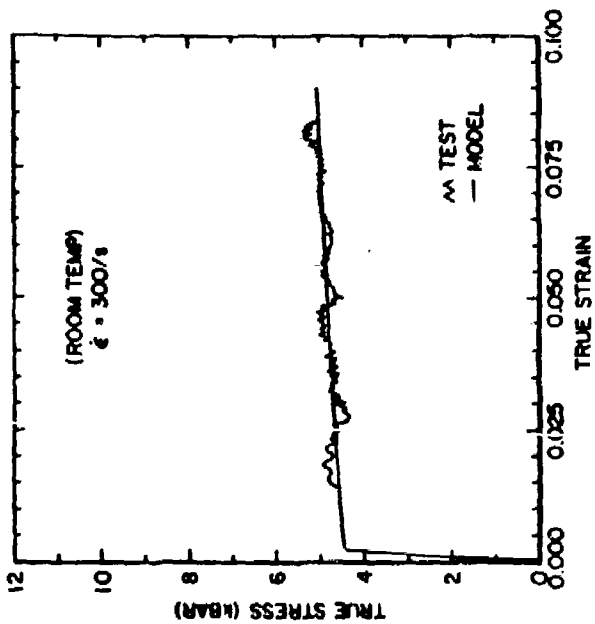
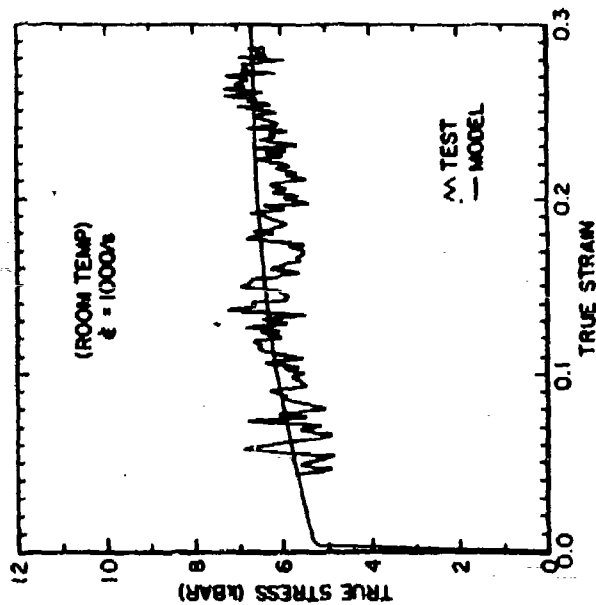
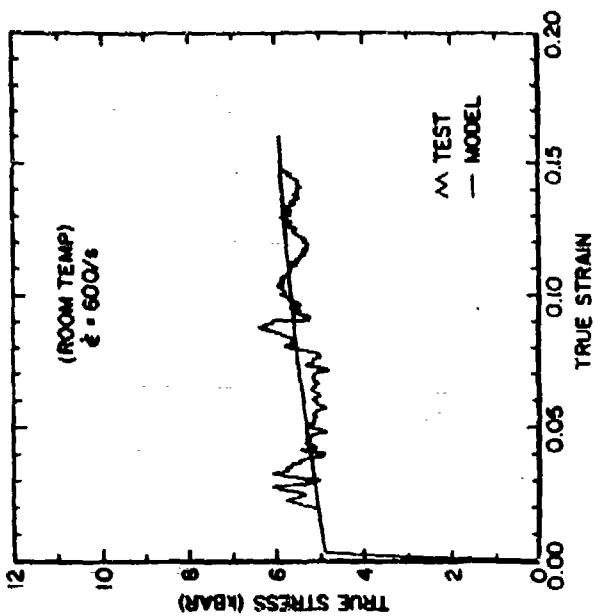


Figure 27. Comparisons of B-p Model Simulations with SHB Room and High Temperature Tests Results for C1008 Steel.

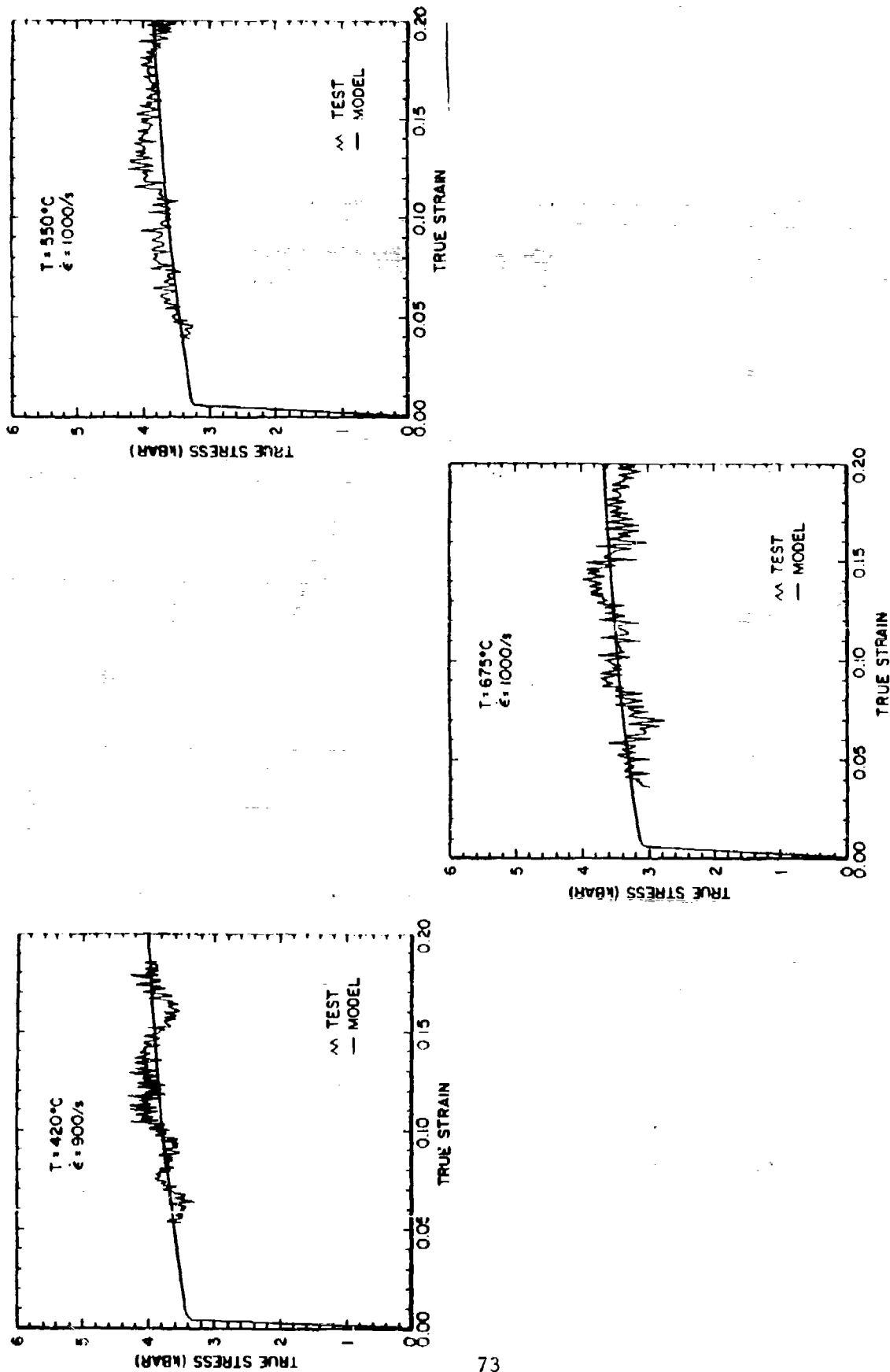


Figure 27. Comparisons of B-P Model Simulations with SHB Room and High Temperature Tests Results for C1008 Steel (concluded).

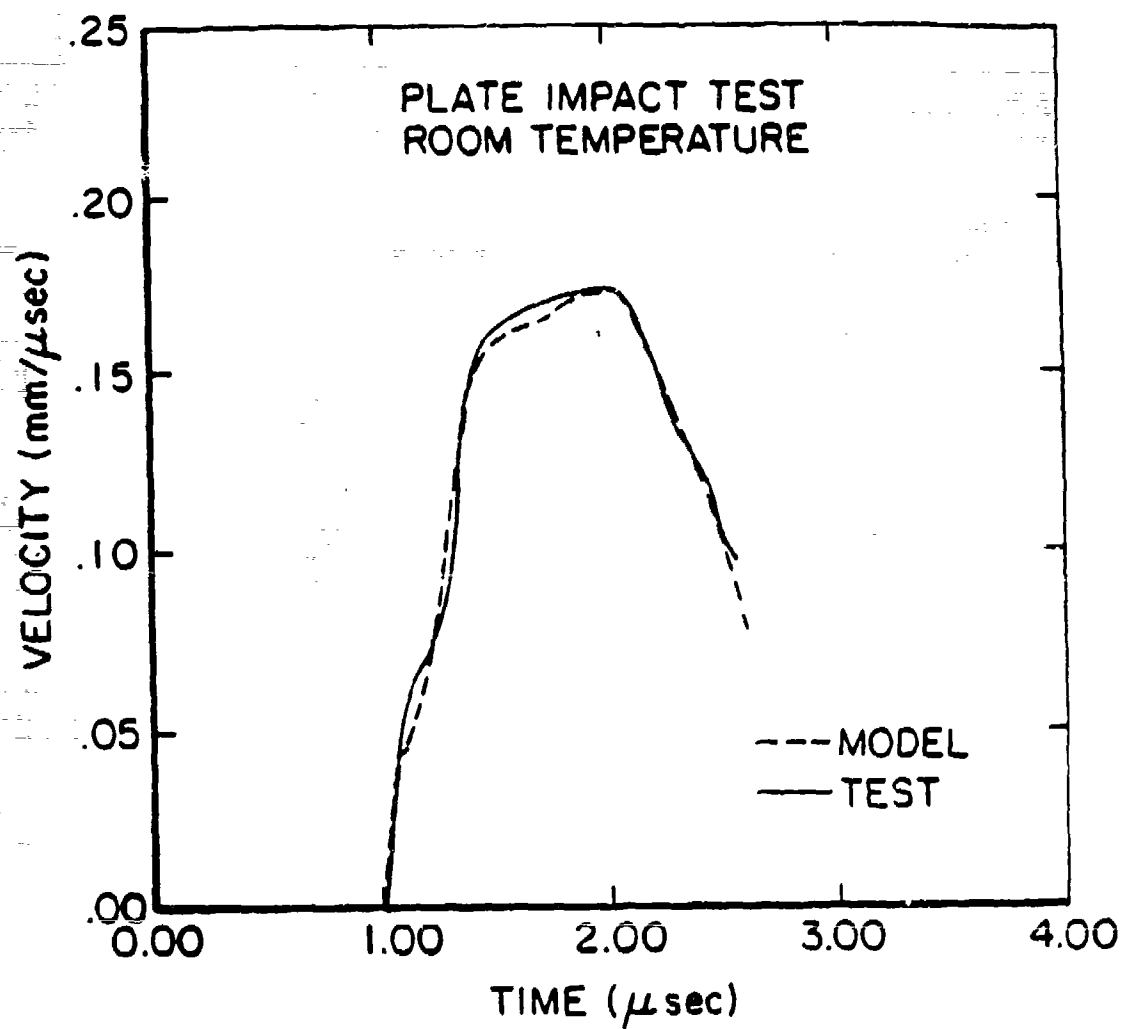


Figure 28. Comparison of B-P Model Simulation with Plate Impact VISAR Data for C1008 Steel.

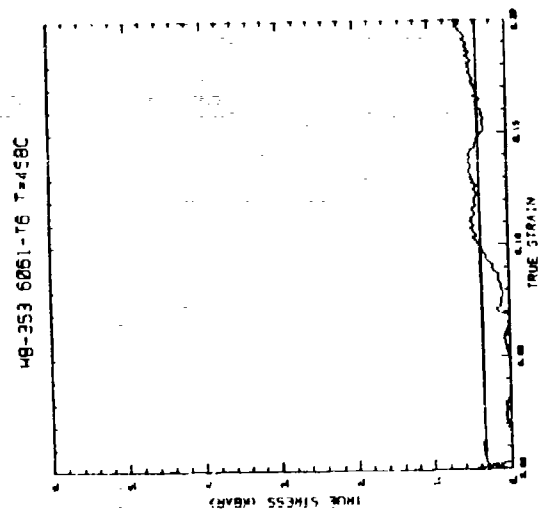
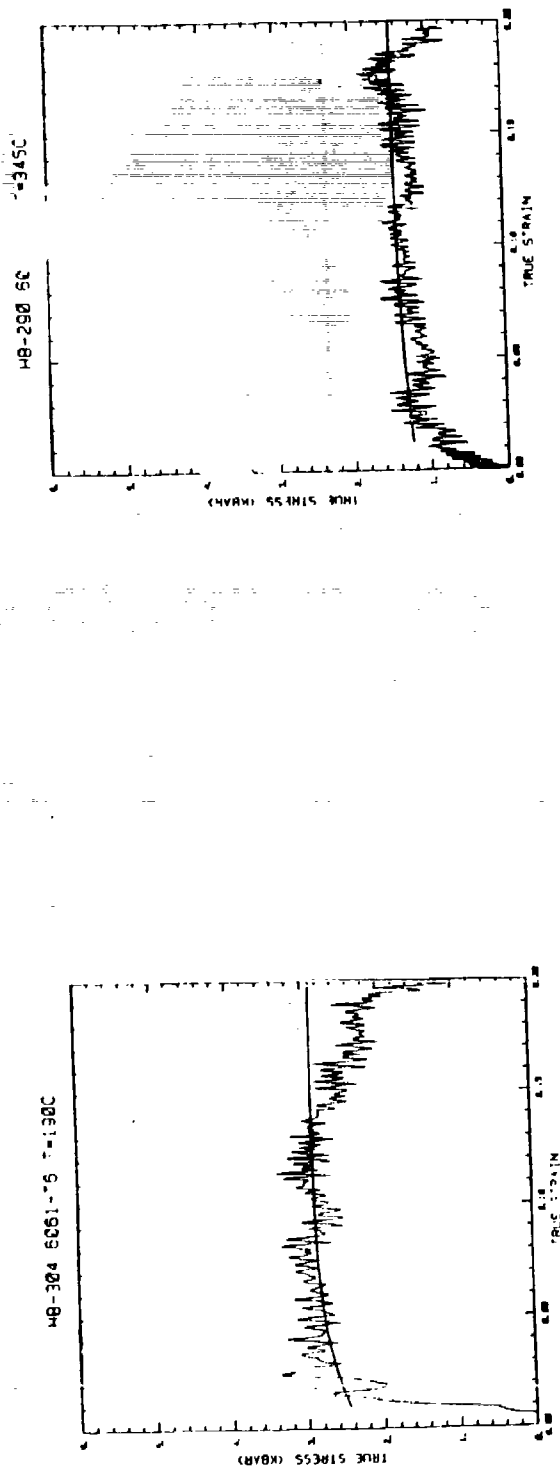
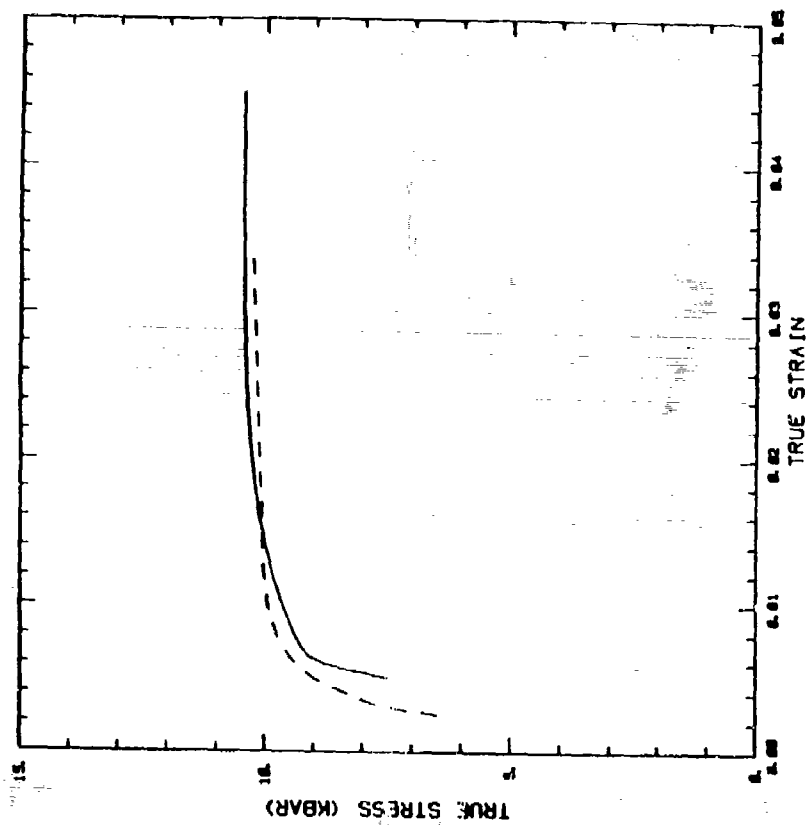


Figure 29. Comparison of B-P Model Simulations with SHB Room and High Temperature Tests Results for 6061-T6 Aluminum.

TUNGSTEN STATIC SR=1.0



TUNGSTEN STATIC SR=.001

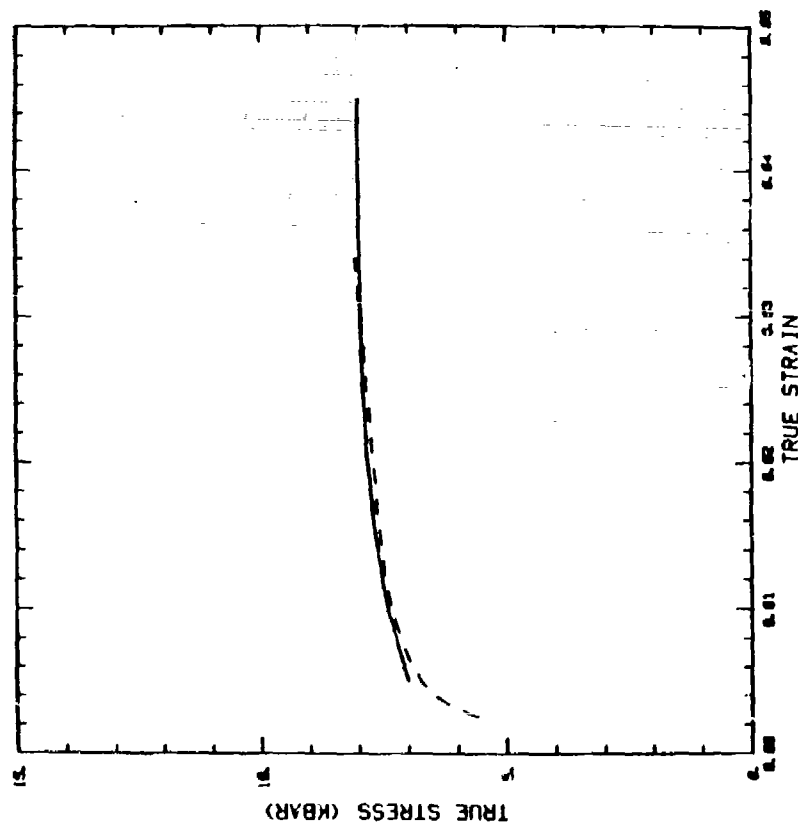


Figure 30. Comparison of Quasi-static Tensile Test Results with B-P Model Simulations for W-2 Tungsten.



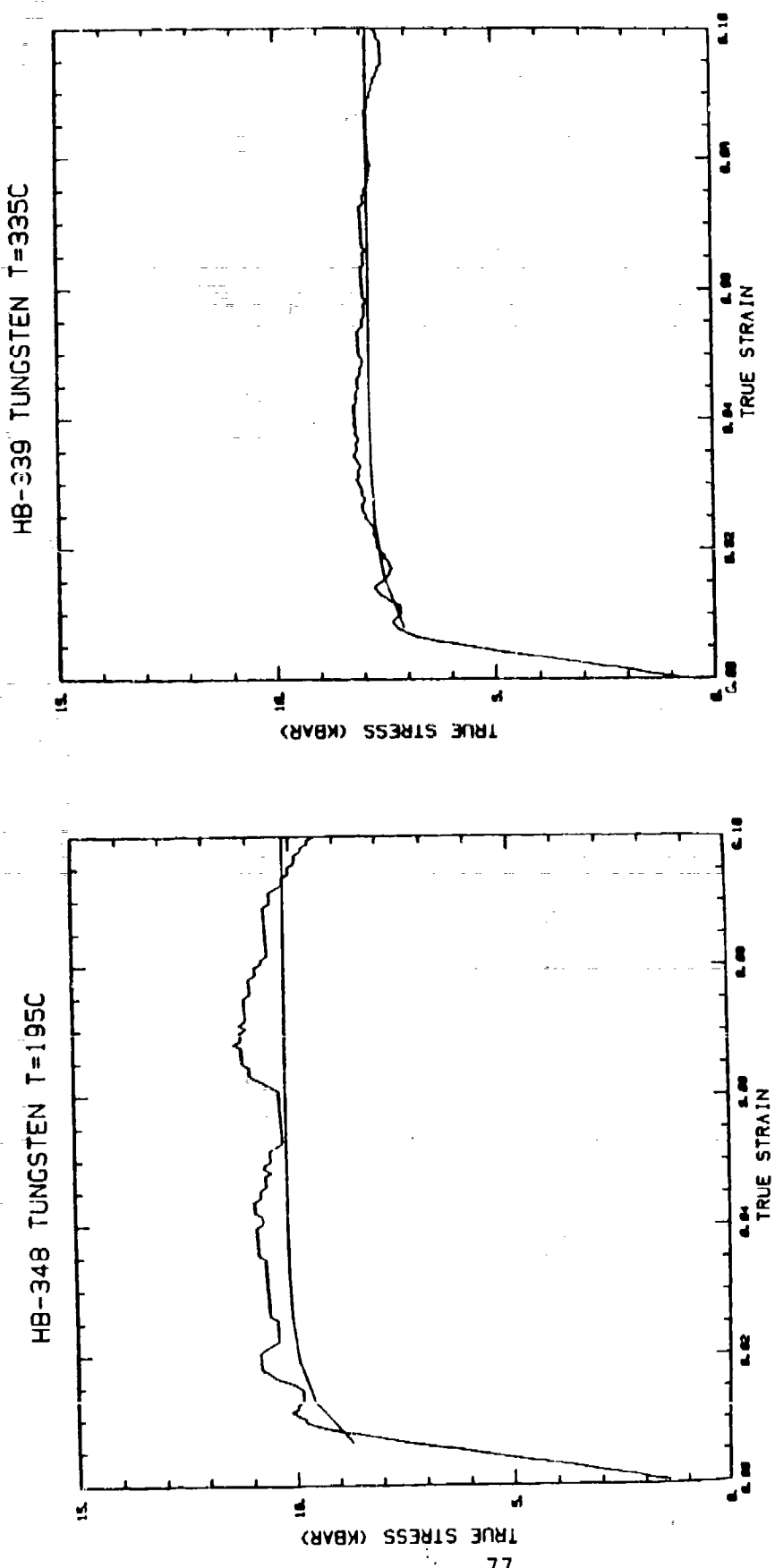
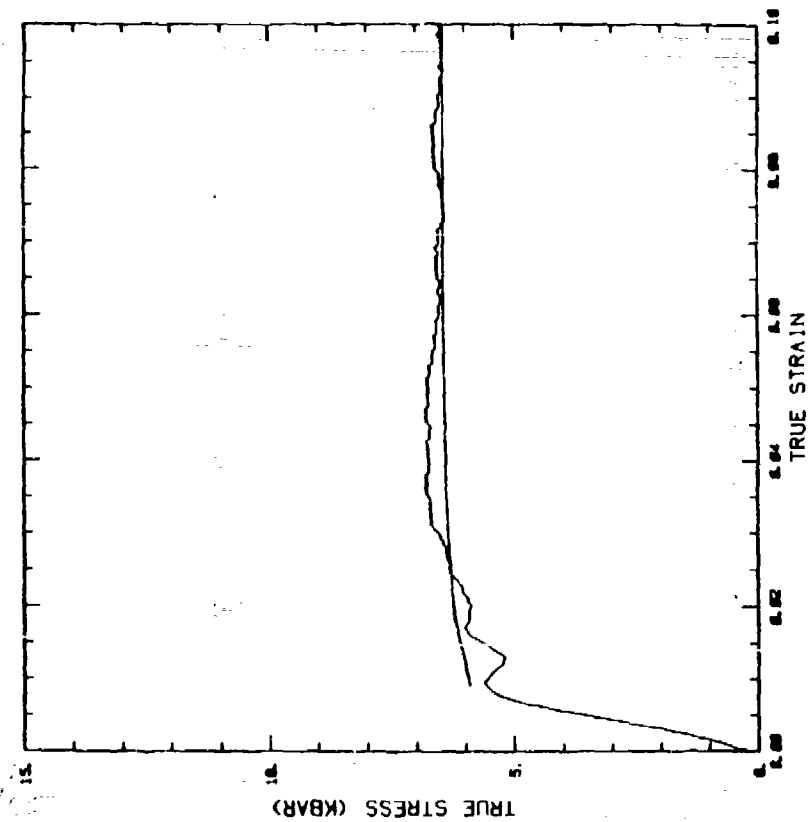


Figure 31. Comparison of B-P Model Simulations with SHB Room and High Temperature Test Results for W-2 Tungsten.

HB-337 TUNGSTEN T=550C



HB-338 TUNGSTEN T = 650C

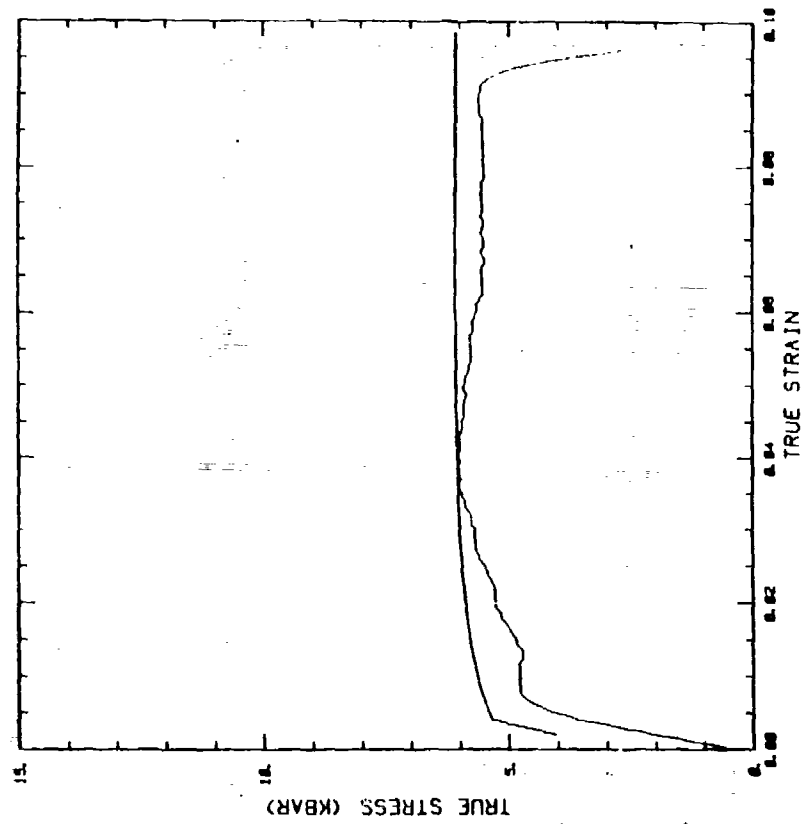


Figure 31. Comparison of B-P Model Simulations with SHB Room and High Temperature Test Results for W-2 Tungsten (concluded).

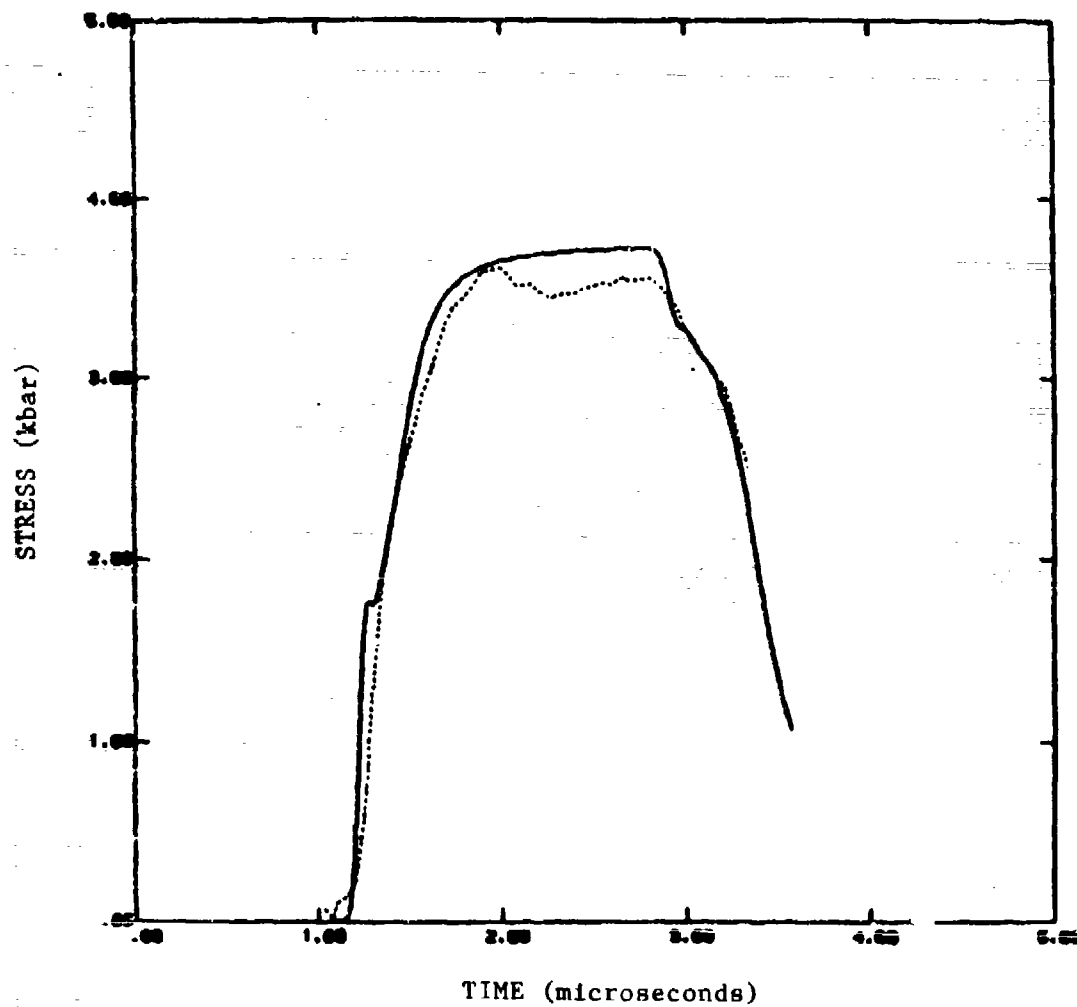


Figure 32. Comparison of B-P Model Simulation with Manganin Gauge Stress History in PMMA W-2 Tungsten.

# NICKEL ROOM TEMPERATURE

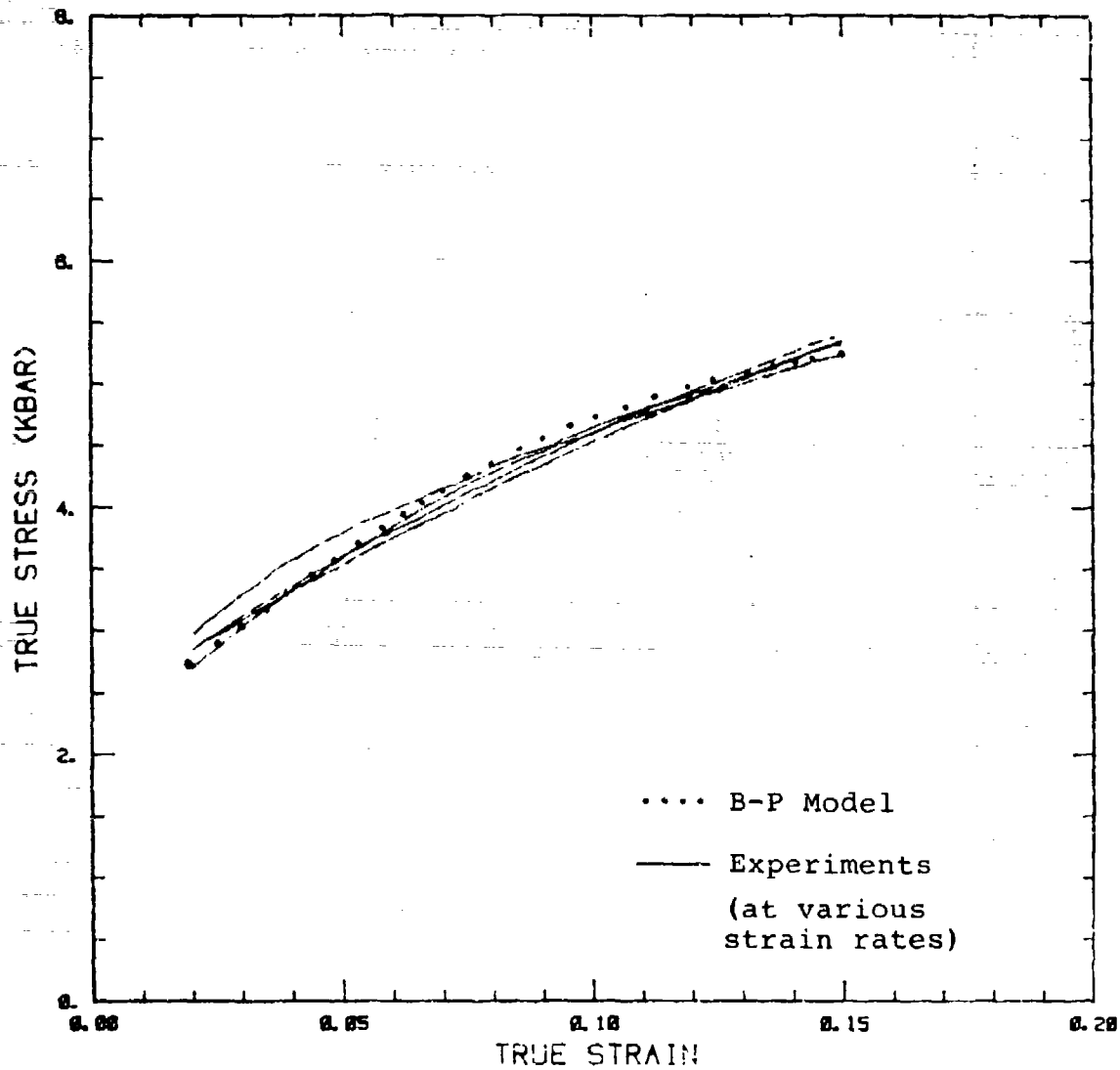


Figure 33. Comparison of B-P Model Simulations with SHB Tensile Test Data for Nickel.

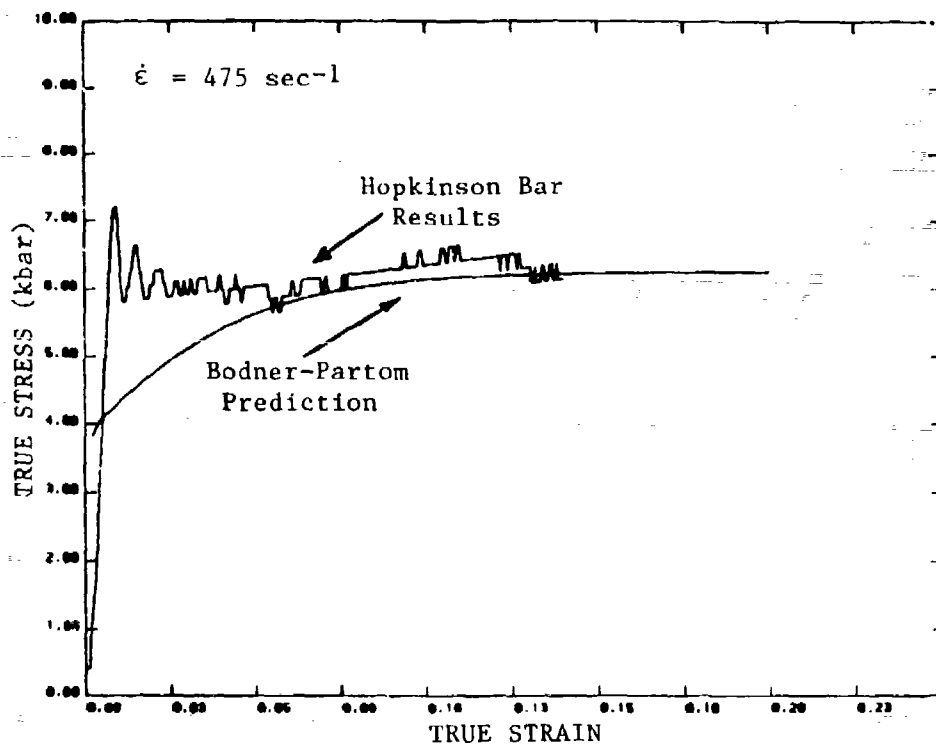
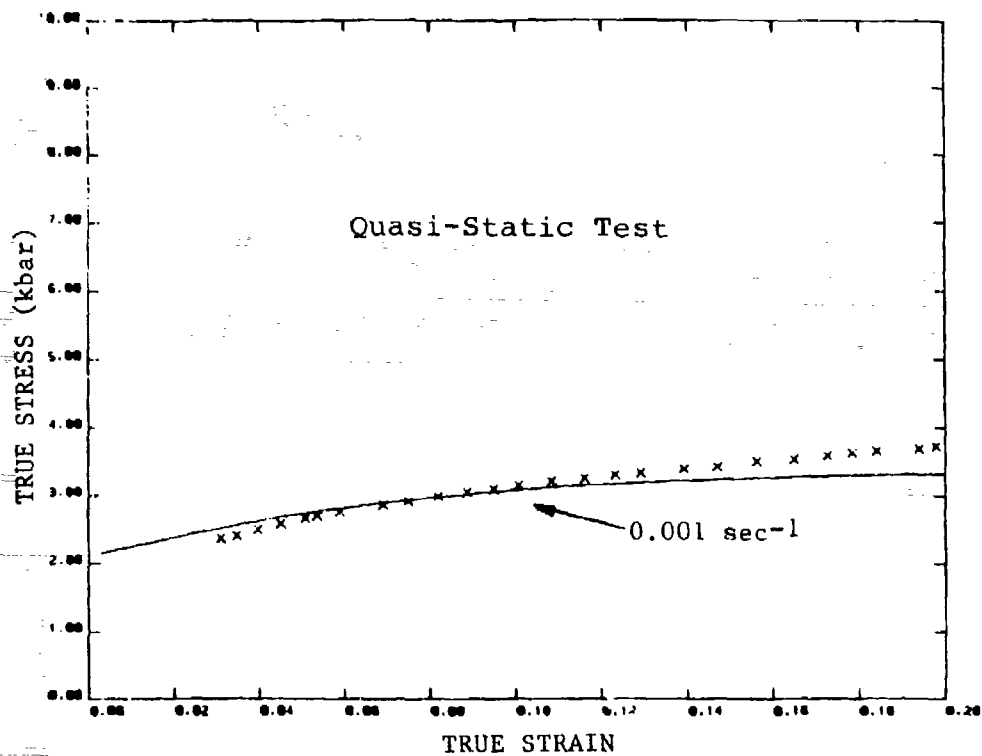


Figure 34. Comparison of B-P Model Simulations with SHB Tensile Tests Data for Armco Iron.

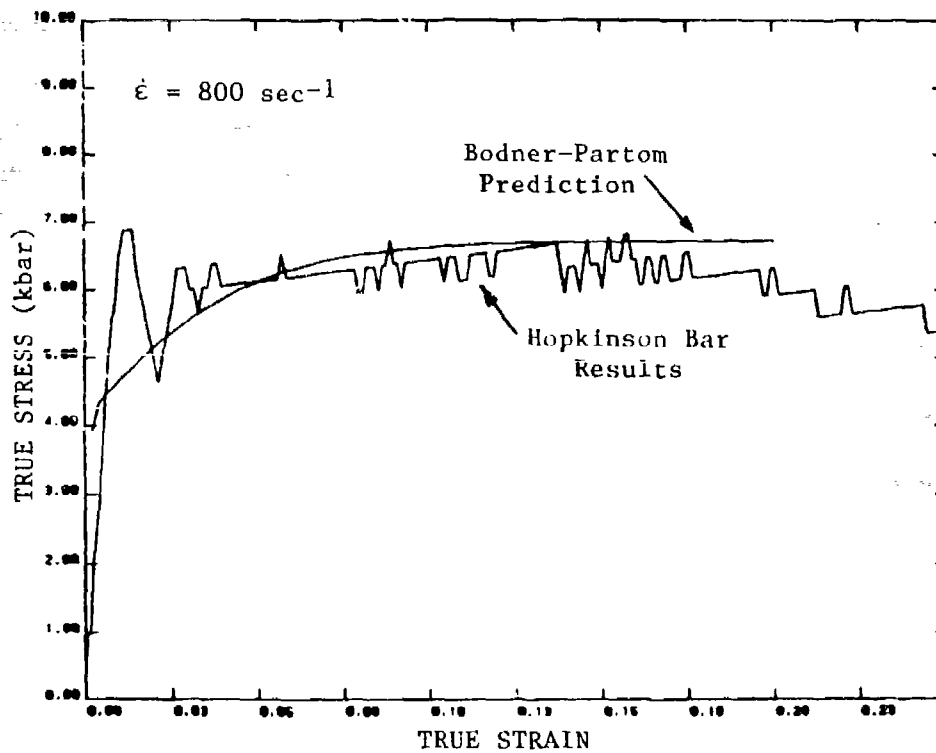
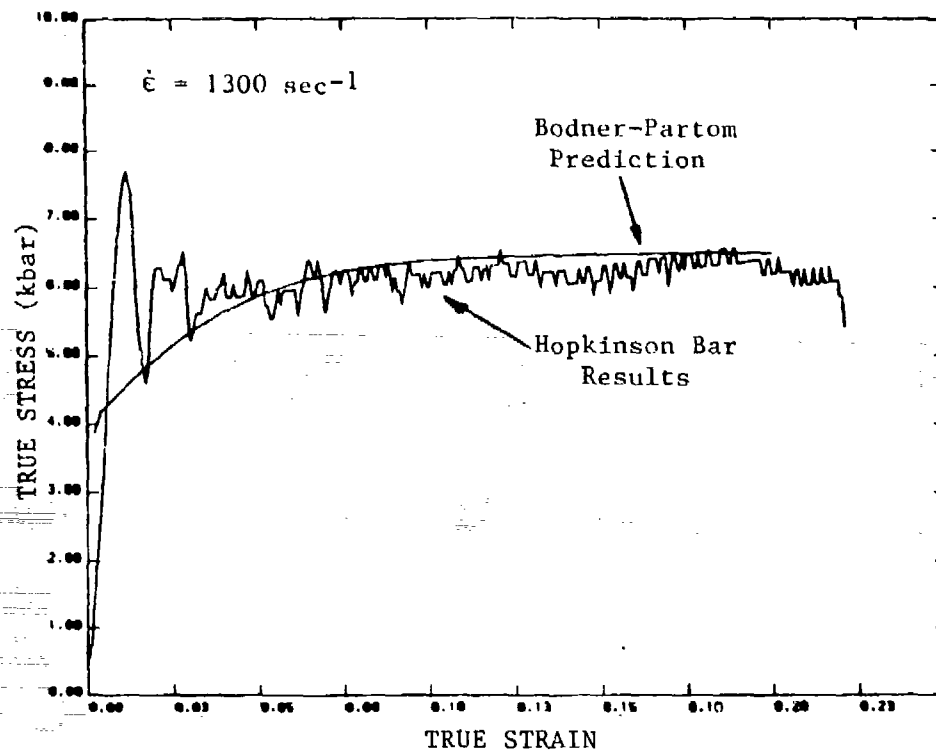


Figure 34. Comparison of B-P Model Simulations with SHB Tensile Test Data for Armco Iron (concluded).

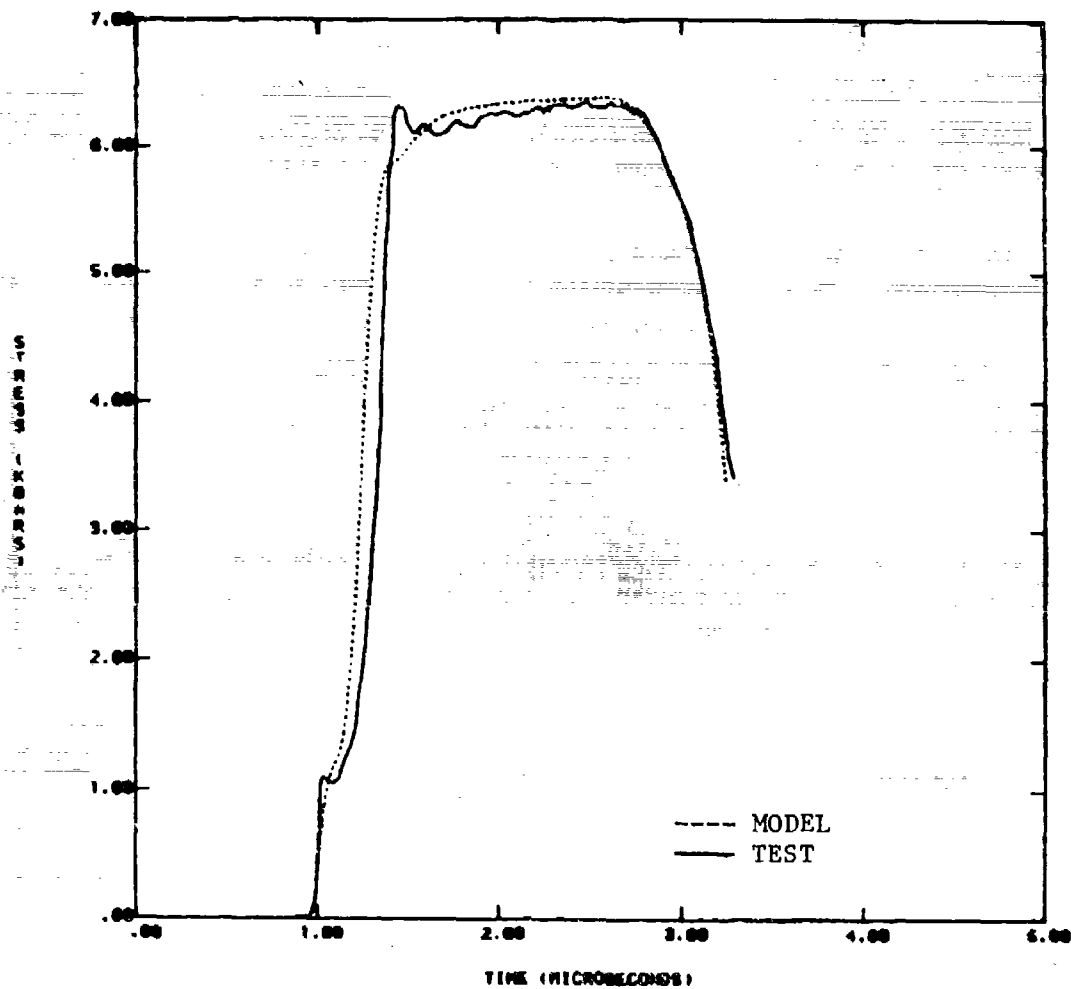


Figure 35. Comparison of B-P Model Simulations with Plate Impact Test Plot for Armco Iron.

# HB-172 OFHC COPPER FULLY ANNEALED

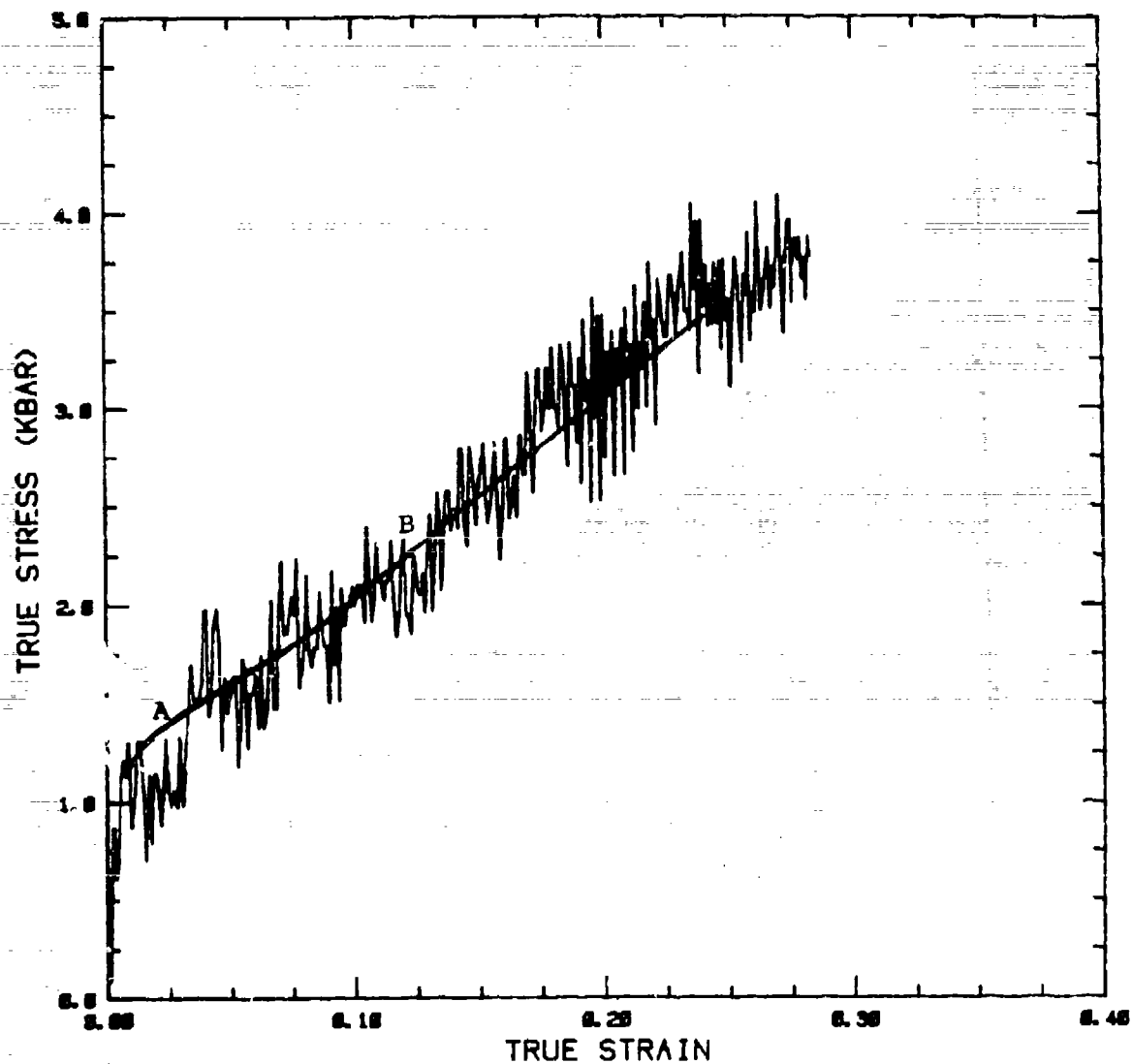


Figure 36. Comparison of B-P Model Simulation with SHB Test Data for OFHC Copper. (Note the unrealistic shape between points A and B.)



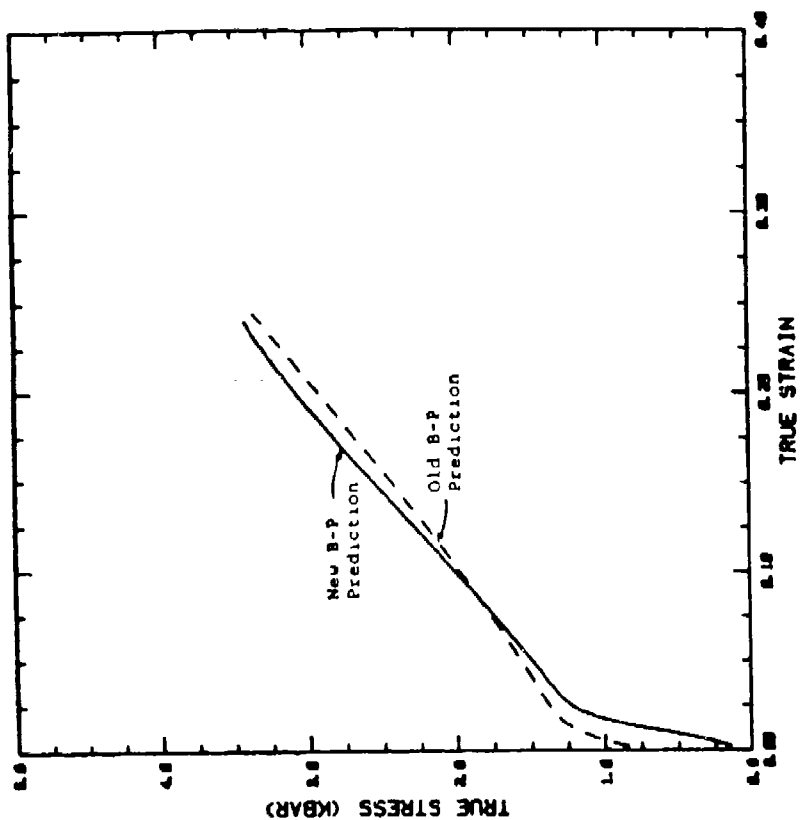
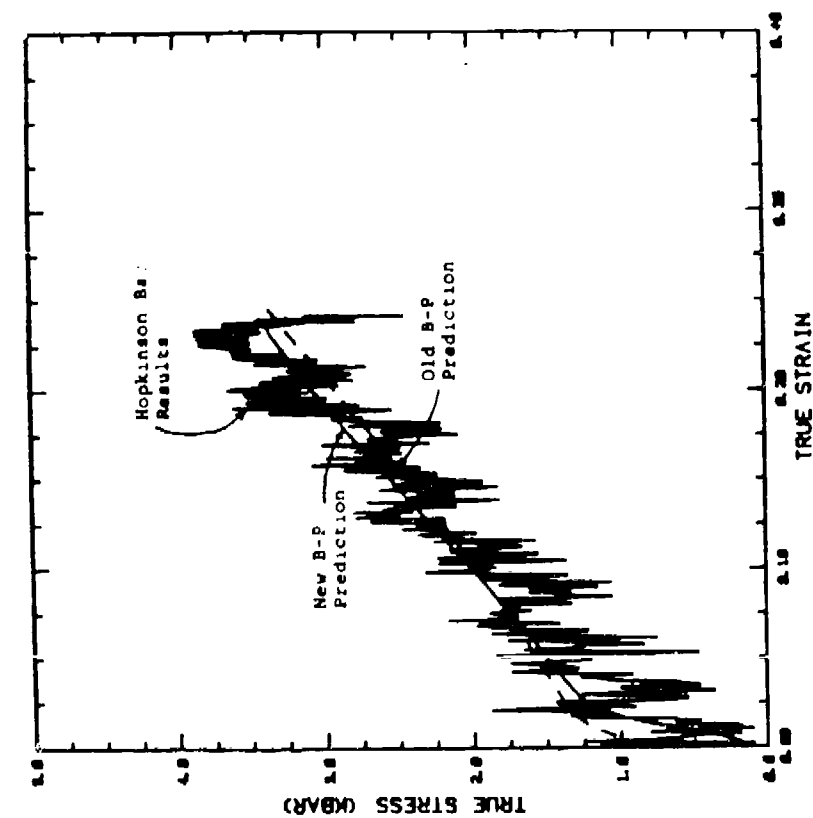


Figure 37. Comparisons Between B-P Model, New Bodner Model, and SHB Test Data for OFHC Copper at  $\dot{\epsilon} = 875s^{-1}$ .

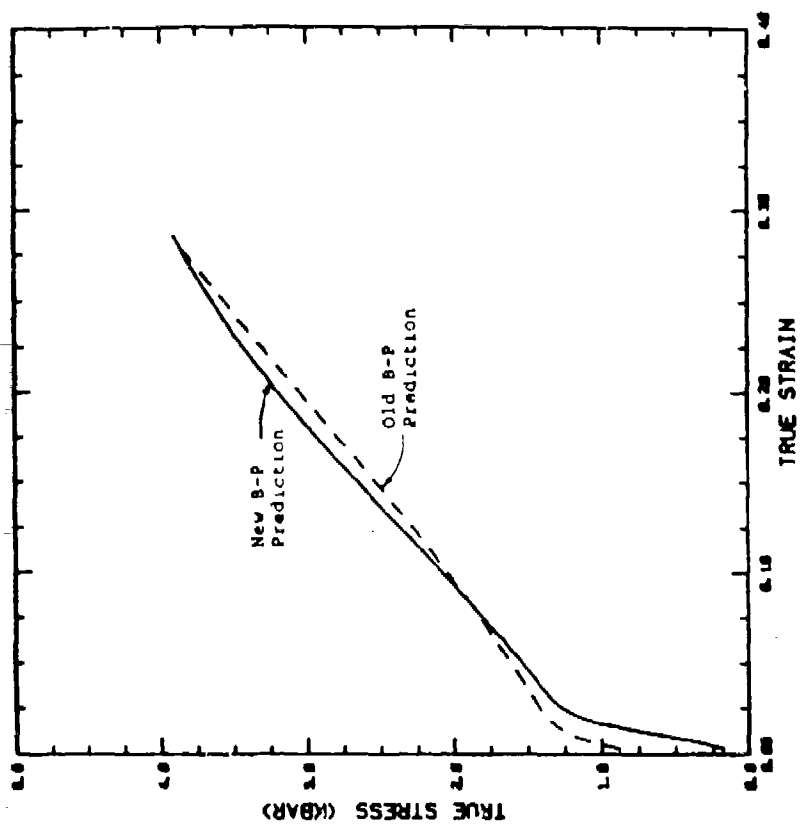
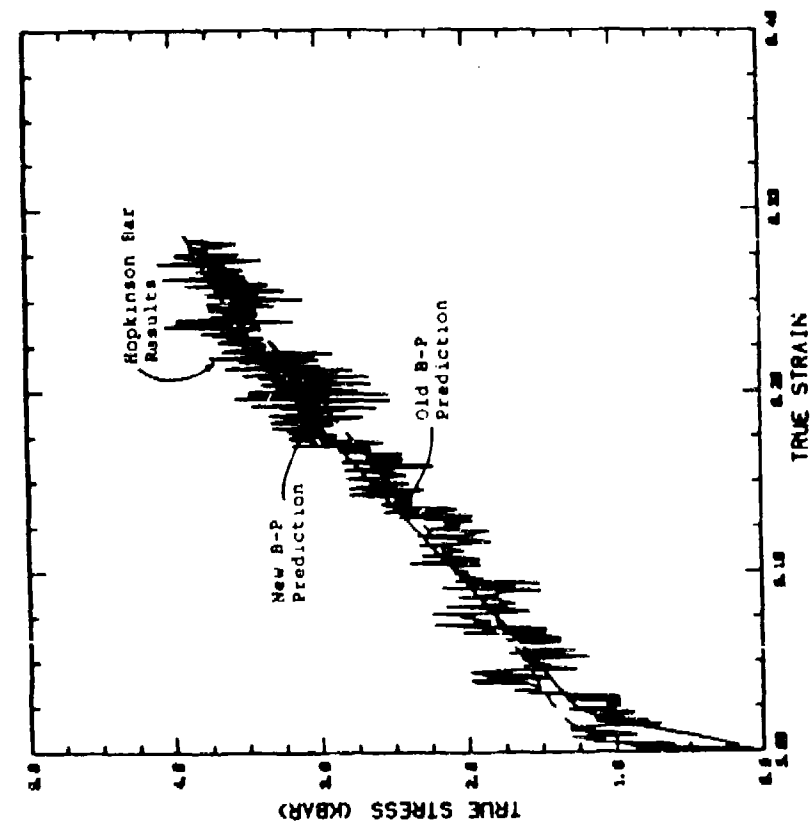


Figure 38. Comparisons Between B-P Model, New Bodner Model, and SHB Tests Data for OFHC Copper at  $\dot{\epsilon} = 1100s^{-1}$ .

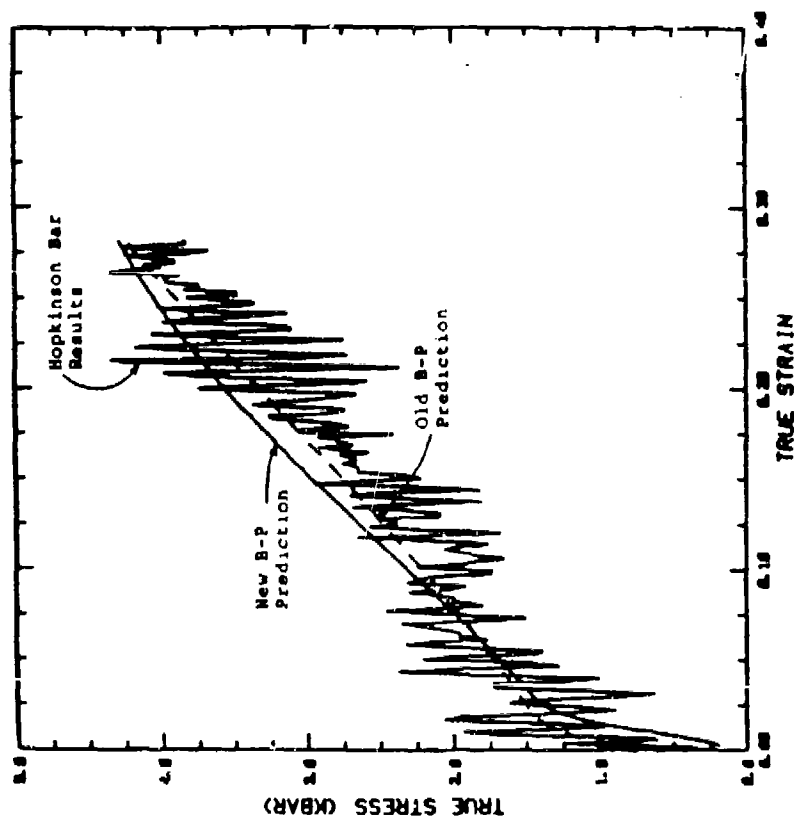
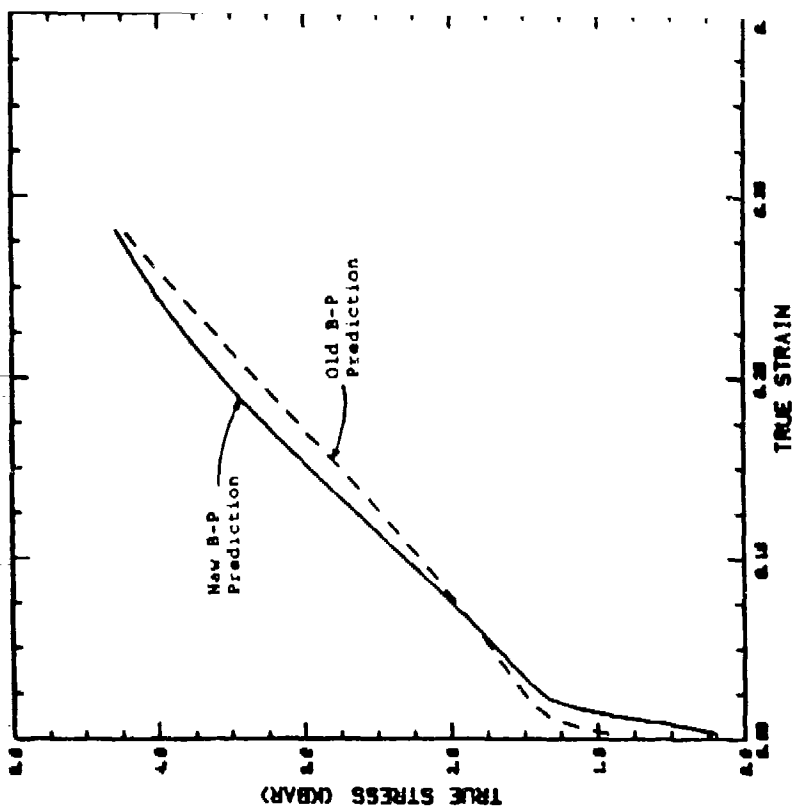


Figure 39. Comparisons Between B-P Model, New Bodner Model, and SHB Test Data for OFHC Copper at  $\dot{\epsilon} = 1300\text{s}^{-1}$ .

pronounced in the new model when compared to the B-P model. It further confirms that the plastic work based evolution equations for state variable may not be able to describe extreme strain hardening behavior.

As a final exercise, we slightly modified the evolution equation for  $Z$  in the B-P model formulation as follows:

$$\dot{Z} = m (Z_1 - Z) \dot{\epsilon}_{eff}^p \quad (34)$$

where  $\dot{\epsilon}_{eff}^p$  is the effective plastic strain rate and is defined by,

$$\dot{\epsilon}_{eff}^p = \sqrt{\frac{2}{3} \dot{\epsilon}_{ij}^p \dot{\epsilon}_{ij}^p} \quad (35)$$

Under uniaxial stress condition, it reduces to:

$$\dot{\epsilon}_{eff}^p = \dot{\epsilon}_1^p \quad (36)$$

We modeled the SHB test results on OFHC copper using this modified equation. Figure 40 shows the comparison of the model simulation with the SHB stress-strain curve. Use of effective plastic strain rate has eliminated the unrealistic concavity in the stress-strain curve. It also compared with the test results very well. In Figure 41 the model simulations of  $\dot{W}_p$  and  $\dot{\epsilon}_{eff}^p$  based B-P models are compared. It can be seen from this figure, the shape of the stress-strain curve of  $\dot{\epsilon}_{eff}^p$  based model is extremely good. The strain-hardening behavior is very realistic due to the absence of the concave-up behavior. At present we are not sure whether this indicates that the B-P model equation requires modification. The stress-strain behavior based on the strain rate jump test results on OFHC copper was modeled by the Bodner-Partom equations [41] extremely well. The merit of B-P model is in its ability to model the loading history effect on flow stress. It is yet to be seen whether a similar match can be achieved with the  $\dot{\epsilon}_{eff}^p$  based B P model.

# HB-181 PREDICTED ( $\dot{E}_p$ ) VS. EXPERIMENTAL

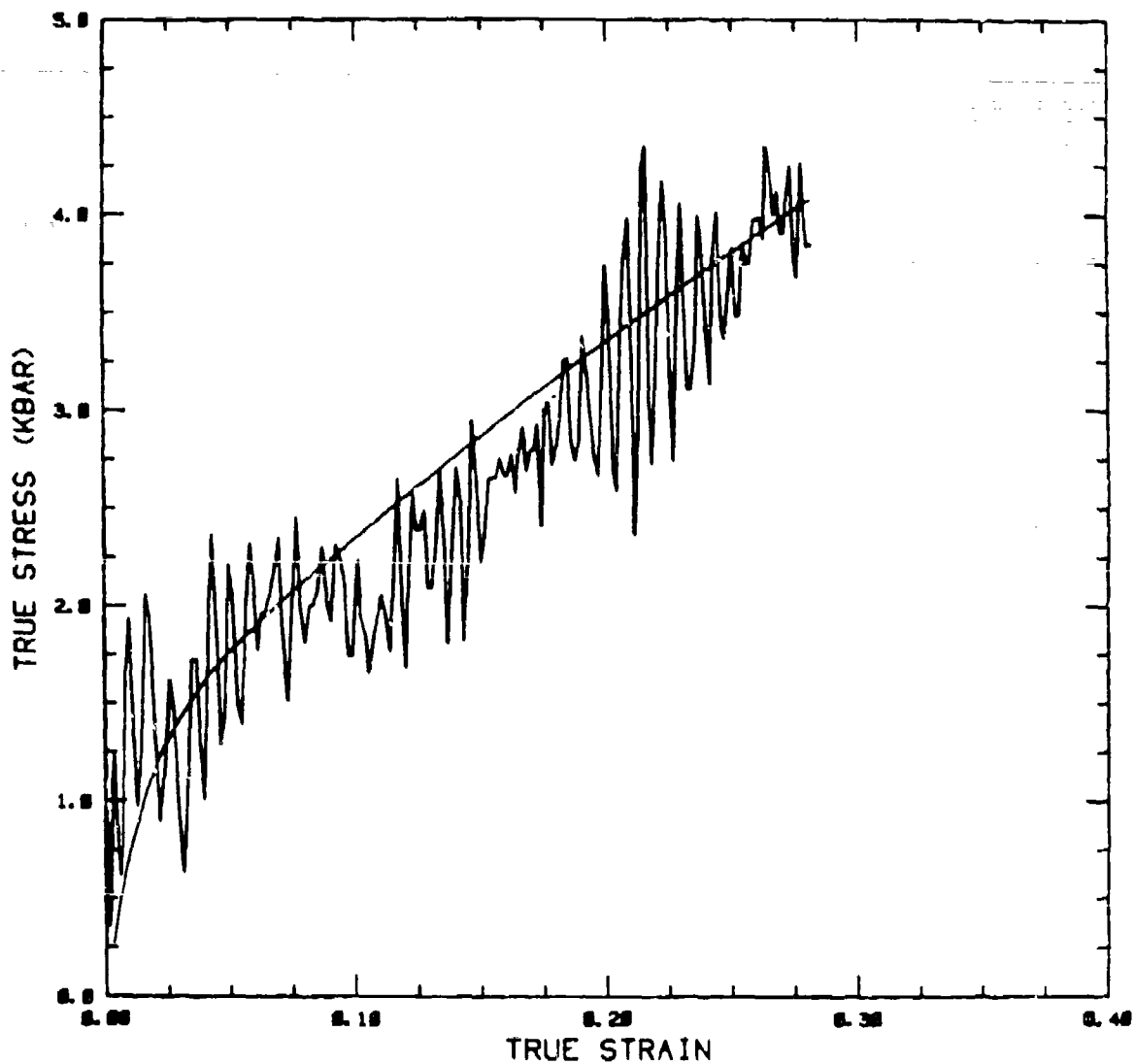


Figure 40. Comparison of Modified B-P Model (Effective Plastic Strain Rate Based) with SHB Test Data for OFHC Copper.

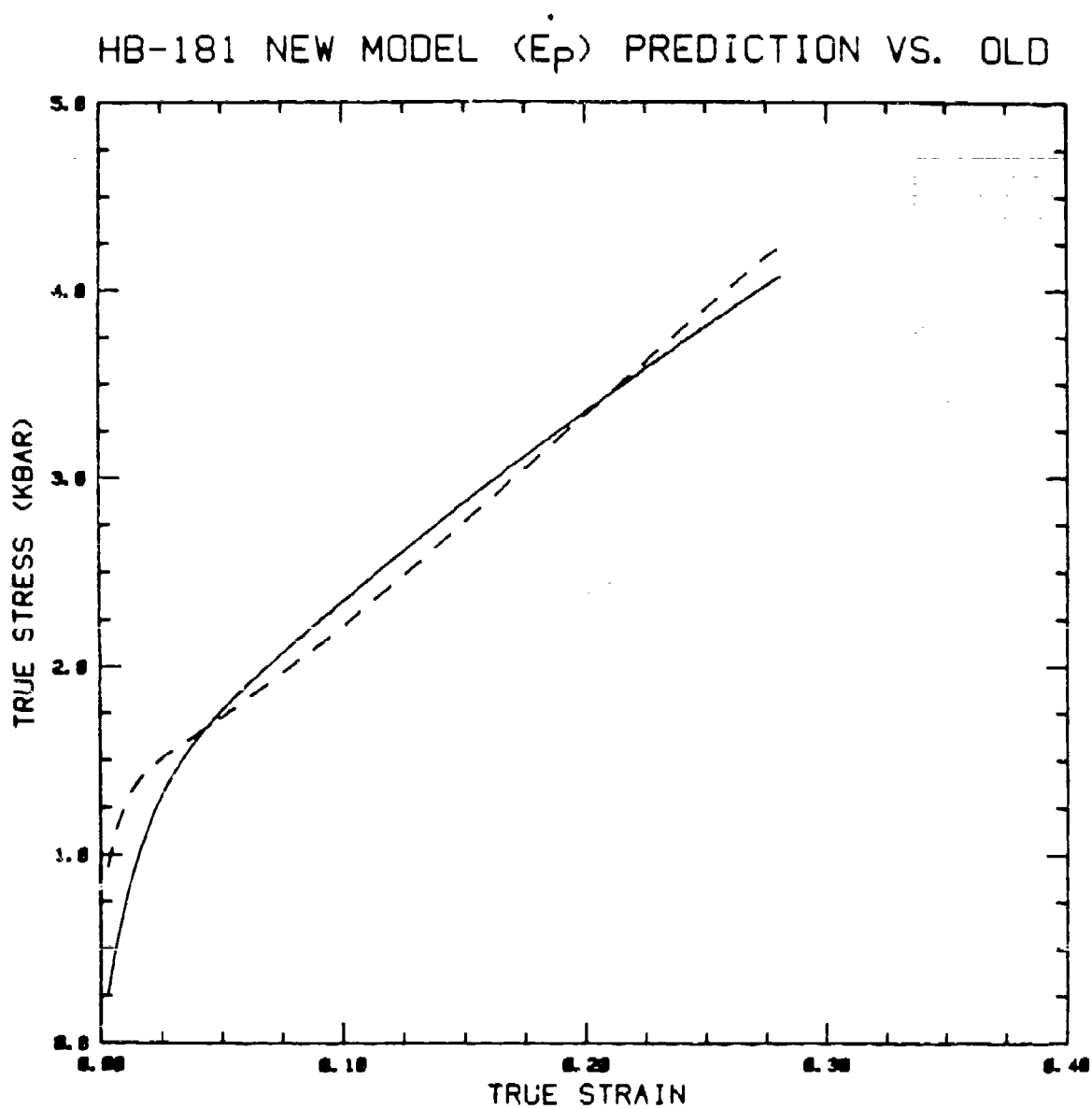


Figure 41. Comparison Between Effective Plastic Strain Rate Based Model and Plastic Work Based B-P Model.

### 3.6 PRECURSOR DECAY ANALYSIS

The phenomenon of elastic precursor decay in planar impact experiments has been a subject of great interest to researchers in dynamic plasticity and shock wave propagation during the last few decades. Efforts to understand and predict precursor decay have involved both experiments and analytical/computational modeling. The latter has been largely associated with concepts based on dislocation dynamics. In this investigation, we invoke the basic assumption that the precursor decay phenomenon is associated with rate-dependent material response. Our objective was to model this phenomenon using the Bodner-Partom model. In the present study, the B-P model parameters for rate-dependent C1008 steel were determined based on a combination of dynamic stress-strain curves obtained from the SHB tests and the HEL obtained from planar plate impact tests. Using the STEALTH code, we simulated plate impact tests. The transient wave profiles in terms of stress vs. time and velocity vs. time were numerically obtained. The B-P model predictions of these wave profiles were compared directly with the experimental data reported in Reference 1. In the numerical evaluation, a mathematical definition of the HEL has also been proposed.

Precursor decay is a phenomenon that is associated with a planar plate impact test configuration. It is defined as the decay of the longitudinal stress amplitude ( $\sigma_{HEL}$ ) of the elastic wave (precursor) from a peak value at the plane of impact ( $= 1/2\rho cv$ ;  $\rho$ , the density,  $c$ , the sound speed,  $v$ , the impact velocity) to a steady state value at some distance from the impact plane. For an elastic-perfectly plastic, rate independent material, the  $\sigma_{HEL}$  is related to the initial yield stress ( $Y_0$ ) under uniaxial stress through the relationship (5), given in Section 2.4.

Precursor decay cannot be modeled by rate independent models. A rate dependent theory is required to model precursor decay. When such a theory is employed in a finite difference code to evaluate the decay phenomenon, a mathematical definition of HEL is essential. For this purpose, using a concept similar to the 0.2

percent offset criterion that has been used to determine the initial yield stress in a uniaxial quasi-static tension test, a critical value of effective plastic strain,  $\epsilon_{eff}^p$ , is proposed. A detailed analysis of the proposed criterion can be found in Reference 42.

To determine the critical value of  $\epsilon_{eff}^p$ , we simulated a plate impact experiment in which the flyer and target plates were 3 mm and 20 mm, respectively. The precursor decay was calculated first using a critical value of 0.002 and then a value of 0.0002. Figure 42 compares the decay results obtained in these two cases. The steady state HEL value for C1008 steel obtained from plate impact experiments [1] was around 9 Kbar and this compared well for  $\epsilon_{eff}^p = 0.0002$  as can be seen from Figure 42. We also employed a value of 0.0001 which did not significantly change the results. The value of 0.0002 was thus arbitrarily chosen as the critical value of  $\epsilon_{eff}^p$ .

The experimental HEL points were compared in Figure 43 with the results obtained from STEALTH using the B-P model parameters. The analytical prediction of precursor decay matched extremely well with the experimental results. The proposed definition of HEL was also verified by employing the viscoplastic model of Perzyna [32]. We validated further the proposed mathematical definition of HEL by modeling precursor decay in aluminum 7039-T64. In all cases, a critical value of 0.0002 for  $\epsilon_{eff}^p$  was employed successfully.

The present study demonstrated that (a) the precursor decay phenomenon can be predicted using a state variable based viscoplastic constitutive model, (b) the model parameters need not be calibrated using the precursor decay data, and (c) a mathematical definition of HEL is required to model the decay phenomenon. We also showed the ability of the Bodner-Partom model in modeling material response under a wide range of stress states and strain rates. The model parameters that were determined using SHB and the steady state value of HEL are general.



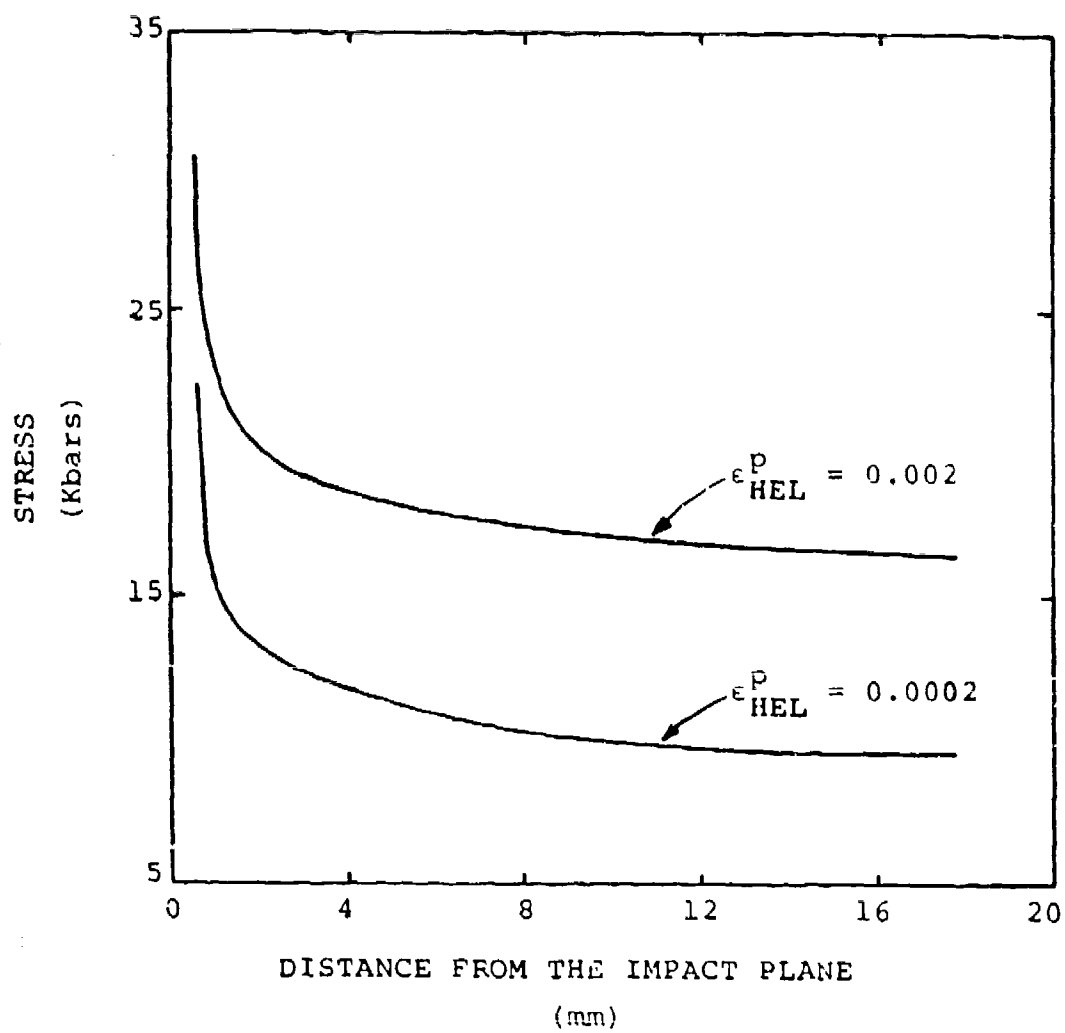


Figure 42. Precursor Decay along the Target Thickness Using  $\epsilon_{eff}^P$  Criterion.

# COMPARISON WITH EXPERIMENTS

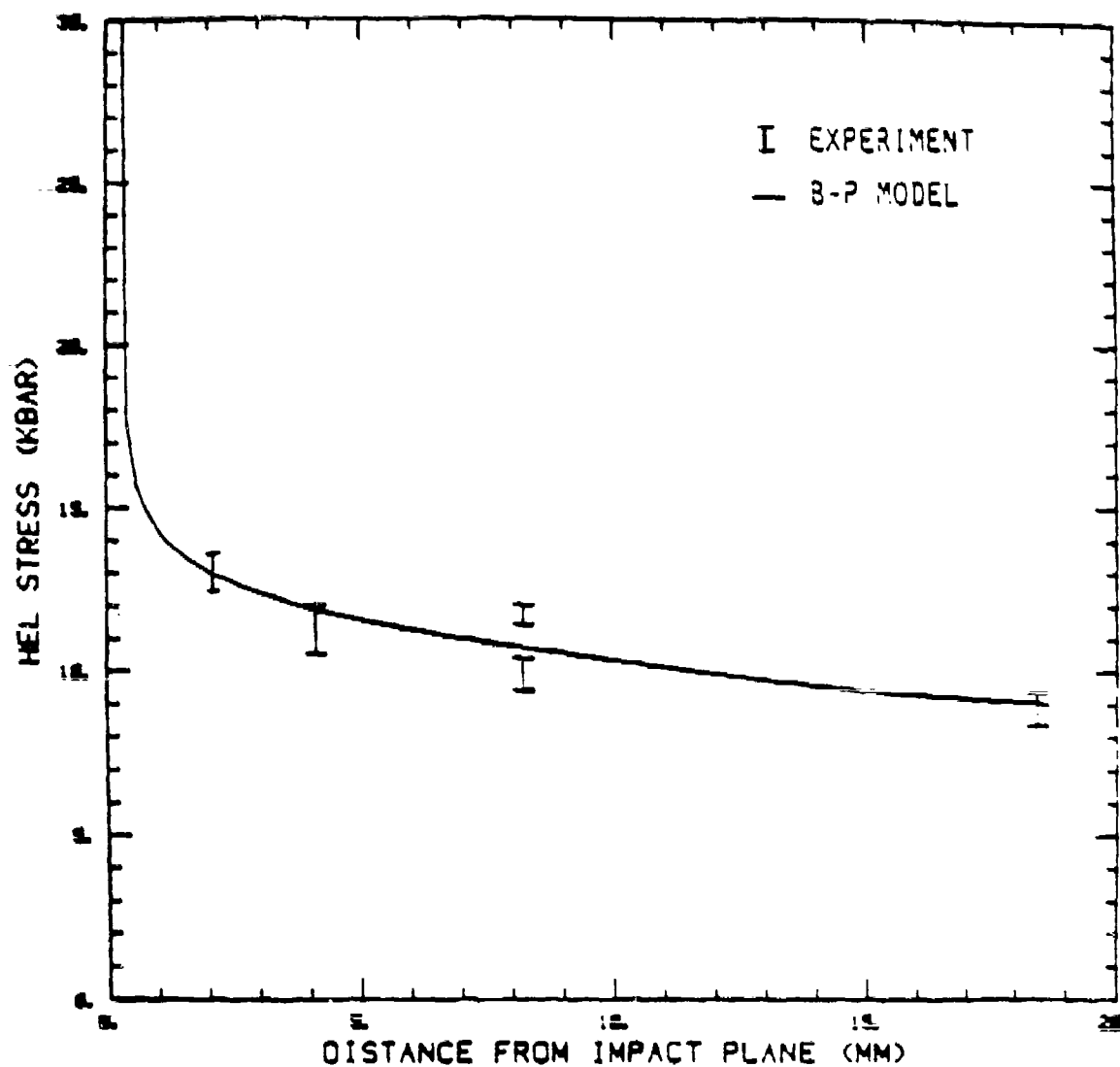


Figure 43. Comparison of the Experimental Data with the Model Prediction.

## SECTION IV

### DYNAMIC FAILURE MODEL

Dynamic failure processes in ductile metals has been a study of interest for the last few decades. There are numerous journal articles, technical reports, and conference proceedings on this subject. Investigators with widely varied background, such as applied mechanists, metallurgists, shock physicists, etc, have been contributing to the understanding of dynamic fracture. The fundamental failure mechanism associated with dynamic fracture in ductile metals is one which considers the failure process as being initiated by the nucleation of voids around inclusions and their subsequent growth and coalescence as suggested by McClintock [43]. During the last two decades, different approaches have been taken by several investigators to apply this mechanism as a means of predicting ductile failure. Among them, Rice and Tracey [44] considered the growth kinetics of a single void in the matrix and developed a model which showed the dependence of void growth rate on the triaxiality of the stress state.

Hancock and MacKenzie [45] provided the experimental evidence to support this dependency on the stress state and used this model to predict failure initiation in notched tensile specimens under quasi-static loading conditions. Their study is under obviously low mean stress levels.

There are other experimental configurations in which this fundamental failure mechanism is frequently observed and reported. One such experiment involves impacting a flyer plate of one material against a target of the same or other material at a higher velocity. Compressive stresses are produced and transmitted immediately from the plane of impact to the adjacent stress-free areas of the material in the form of a stress pulse. Fracture is then induced by tension arising from the interaction of reflected shock waves from the stress free-planes parallel to the plane of impact. The interesting feature is the growth and coalescence of voids under high mean stress levels leading to failure in the target plate; this type of failure is often referred to as

spallation. Earlier spall models were mostly based on a simple criterion in which stress, strain, pressure, or energy is assumed to reach a critical value. Failure had been assumed to occur instantaneously. This type of time independent failure model may work well when the spall is well above the threshold conditions. Later, Tuler and Butcher [46] introduced a time dependent failure criterion. They assumed that failure occurs only after a critical value of damage is reached. This model has three parameters which have to be determined from spall experiments. Several other investigators [47-50] proposed models to predict the spall threshold. They considered the nucleation and growth rates of voids through rigorous mathematical modeling of the failure process. Meyers and Aimone [51] have reviewed the fundamental aspects of spallation and the modeling efforts by the various research workers.

The various approaches can be grouped into three categories: (1) micro-statistical approach, (2) physically motivated empirical approach, and (3) continuum mechanics based approach. The first approach was mainly pursued by Curran and co-workers [52]. Based on the extensive micro-statistical analyses of the void sizes and orientations, they developed models to describe the void nucleation and growth processes. In the second ad hoc approach, the objective was to develop models, not based on any extensive analyses of microstructures or the kinetics of the failure processes, but mainly based on the ability to predict certain measured quantities such as the free surface velocity of the target plate. Under this approach most of the works had been strictly developed and limited to rectilinear motions. In most cases, the generalization of such theories to any other geometry is not possible. The third approach considered a general solution to the problem of spallation. Davison, Stevens, and Kipp [49] presented a theory of spall damage based on a unified and thermodynamically consistent treatment of elastic-viscoplastic deformation. A continuum mechanics approach was employed with a three-dimensional theory.

#### 4.1 MODEL FORMULATION

There are at least four phases in the constitutive modeling of damaged materials that were initially intact. The first phase of the modeling is the description of the intact material behavior. Prior to the development of damage, the aggregate is the fully dense matrix material which is usually modeled by incompressible plastic flow theories. The second phase is the description of the damaged material. We require a model to describe the behavior of the aggregate material which contains microvoids/microcracks. In the third phase, depending on the nucleation mechanism, a mathematical description of the process will be required. This phase will also require a model to describe the growth of damage. The last phase of modeling is the coalescence of damage leading to total failure. The final process occurs quite rapidly when compared to the nucleation and growth processes. Modeling of the fundamentally observed instabilities [53,54] during the final failure process will be cumbersome and tedious. A simplistic approach is to describe this process through a critical criterion based on a single parameter. For example, one such criterion could be based on a critical level of damage. This section describes the modeling efforts on each of the above mentioned phases.

##### 4.1.1 Phase I - Modeling of Matrix Material

The fully dense, void-free matrix material can be modeled through the state variable based viscoplastic constitutive equations of Bodner-Partom [34]. The B-P model will be used in the constitutive model formulation for the porous aggregate in terms of equivalent plastic strain rate  $\dot{D}_m^p$  and effective stress,  $Y_m$ . The equivalent plastic strain rate is defined by,

$$\dot{D}_m^p = \sqrt{\frac{2}{3} \dot{\epsilon}_{ij}^p \dot{\epsilon}_{ij}^p} \quad \text{and} \quad Y_m = \sqrt{3J_2} \quad (37)$$

The equation for  $\dot{D}_m^p$  can be obtained from equation (22) as,

$$\dot{D}_m^p = \frac{2}{\sqrt{3}} D_0 \exp \left\{ - \left( \frac{n+1}{2n} \right) \left( \frac{Z}{Y_m} \right)^{2n} \right\} . \quad (38)$$

B-P model parameters for several metals have been already determined and reported in Section III. The number of parameters for describing matrix material behavior is only four, i.e.,  $m$ ,  $n$ ,  $Z_0$ , and  $Z_1$ .

Until voids nucleate, the aggregate behavior can be described by the B-P model. The plastic flow in the void-free aggregate is incompressible, i.e., the sum of the principal or orthogonally plastic strains is equal to zero. However, the nucleation of voids will introduce dilatation and the plastic yield behavior will depend not only on the second invariant  $J_2$ , but also on the mean stress or pressure. The constitutive model for the aggregate must include these effects. For this purpose, we selected a yield-criterion-based plastic flow rule in which the pressure dependence enters explicitly into the calculations. The following section describes the Phase II of the constitutive model formulation for the porous aggregate.

#### 4.1.2 Phase II - Modeling of Aggregate with Voids

We considered a yield-criterion-based approach in the constitutive model formulation. For randomly distributed voids or microcracks contained in the aggregate, the yield behavior will be influenced by not only the second invariant of the deviatoric stress ( $J_2$ ) but also by the pressure or mean stress ( $I_1$ ). The following form of the yield function has been considered:

$$A(\rho) J_2 + B(\rho) I_1^2 = \delta(\rho) Y_m^2 \quad (39)$$

where  $A$ ,  $B$ , and  $\delta$  are functions of relative density,  $\rho$ .  $Y_m$  is the effective stress in the material. (Note: the subscript 'm' means matrix material and not a tensorial index.) Based on a critical total deformation energy, Doraivelu et al. [55] derived the following expressions for  $A$  and  $B$ :

$$A(\rho) = 2 + \rho^2 \quad (40)$$

and

$$B(\rho) = \frac{1 - \rho^2}{3} \quad (41)$$

The expression for  $\delta(\rho)$  was given by

$$\delta(\rho) = 2\rho^2 - 1 \quad (42)$$

This particular form for  $\delta(\rho)$  was chosen based on the experimental results obtained from sintered or hot pressed powder-metallurgy materials under uniaxial compression at quasi-static strain rates. In general, this function is material dependent while the functions A and B are independent of the matrix material behavior. Thus, the yield condition for the aggregate can be written as:

$$\Phi = (2 + \rho^2) J_2 + \frac{1 - \rho^2}{3} I_1^2 - \delta(\rho) Y_m^2 = 0 \quad (43)$$

The viscoplastic strain rates in the aggregate can be calculated using the flow rule derived as:

$$\dot{\epsilon}_{ij}^p = \dot{\lambda} \frac{\partial \Phi}{\partial \sigma_{ij}} \quad (44)$$

The proportionality factor  $\dot{\lambda}$  can be obtained using the flow rule in conjunction with the following relationship:

$$(1-f) Y_m \dot{D}_m^p = \sigma_{ij} \dot{\epsilon}_{ij}^p \quad (45)$$

where  $f$  is the void volume fraction and related to relative density ' $\rho$ ' through  $f = 1 - \rho$ . The above expression was derived from the definition that the total plastic work in the aggregate is entirely due to the plastic work done by the matrix. By combining equations (44) and (45),  $\dot{\lambda}$  can be expressed by,

$$\dot{\lambda} = \frac{(1-f) Y_m \dot{D}_m^p}{\frac{\partial \Phi}{\partial \sigma_{ij}} \sigma_{ij}} \quad (46)$$

The plastic strains in the aggregate can be written as:

$$\dot{\epsilon}_{ij}^p = \frac{(1-f) Y_m \dot{D}_m^p}{\frac{\partial \Phi}{\partial \sigma_{rl}} \sigma_{rl}} \frac{\partial \Phi}{\partial \sigma_{ij}} . \quad (47)$$

In the constitutive model formulation, the total strain rate is decomposed into elastic and plastic strain rates. The elastic strain rates,  $\dot{\epsilon}_{ij}^e$  are related to the stress through Hooke's law as:

$$\dot{\epsilon}_{ij}^e = D_{ik} \dot{\sigma}_{kj} \quad (48)$$

where  $D_{ik}$  is the inverse of elastic modulus matrix,  $E_{ik}$ .

Using the consistency condition which holds during the plastic flow, we can obtain an expression for  $\dot{Y}_m$  as:

$$\dot{Y}_m = \frac{-\left(\frac{\partial \Phi}{\partial \sigma_{ij}} \dot{\sigma}_{ij} + \frac{\partial \Phi}{\partial f} \dot{f}\right)}{\frac{\partial \Phi}{\partial Y_m}} \quad (49)$$

An expression for  $\dot{\sigma}_{ij}$  can be obtained from Equation (48) by replacing the elastic strain rate as the difference between total and plastic strain rates,

$$\dot{\sigma}_{ij} = E_{il} (\dot{\epsilon}_{lj} - \dot{\epsilon}_{lj}^p) . \quad (50)$$

We now need an evolution equation to calculate  $f$  at any given instance of the loading history. The void volume fraction rate,  $\dot{f}$  contains two parts; one due to the growth of existing voids, and the other due to the nucleation of new voids.

#### 4.1.3 Phase III - Nucleation and Growth Models

The growth law can be directly related to the dilatation due to growth of voids in the aggregate. By definition, the growth rate is given by,

$$\dot{f}_g = (1-f) \dot{\epsilon}_{ii}^p \quad (51)$$



where repeated index means summation and  $\dot{\epsilon}_{ii}^p$  are plastic strain rates in the three principal directions.

The most widely used void nucleation model was the one that was initially used by Needleman and Chu [56] in their analysis of localized necking in biaxially stretched sheets. The model was based on a mechanism in which voids are nucleated due to debonding of inclusions from the matrix. The debonding can occur due to either a stress or a strain criterion or both. The corresponding model is given by,

$$\dot{f}_n = F_o (\dot{\gamma}_m + \dot{p}) + F_\epsilon \dot{D}_m^p \quad (52)$$

where

$$F_o = \frac{f_1}{s_1 \sqrt{2\pi}} e^{-\left(\frac{\gamma_m + p - \sigma_N}{2s_1}\right)^2} \quad (53)$$

and

$$F_\epsilon = \frac{f_2}{s_2 \sqrt{2\pi}} e^{-\left(\frac{D_m^p - \epsilon_N}{2s_2}\right)^2} \quad (54)$$

If the nucleation is due to only the matrix debonding from inclusions, then the total void volume nucleated must be consistent with the volume fraction of second phase particles. Therefore, the values determined for the parameters  $f_1$  and  $f_2$  must meet this requirement.  $\sigma_N$  and  $\epsilon_N$  are the mean equivalent stress and strain, respectively around which the nucleation stress and strain are distributed in a gaussian manner.  $s_1$  and  $s_2$  are the standard deviations of the distributions. These two parameters will control the ranges of stress or strain over which most of the voids can be nucleated.

The evolution equation for the void volume fraction is then given by the sum of  $\dot{f}_g$  and  $\dot{f}_n$  as:

$$\dot{f} = (1-f) \dot{\epsilon}_{11}^P + F_0(\dot{\gamma}_m + \dot{P}) + F_\epsilon \dot{D}_m^P \quad (55)$$

where  $F_0$  and  $F_\epsilon$  are given by Equations (53) and (54). Six model parameters have to be determined to describe the void nucleation process, when the process is due to both stress and strain criteria.

When the stress state is triaxial with  $(P/Y_m) \gg 1$ , the nucleation process seems to be stress-controlled; whereas under uniaxial stress states, such as in a thin ring cylinder or under plane stress condition, the mechanism seems to be strain-controlled. It is fairly well established that under high strain rate and high pressure loading conditions, the void nucleation mechanism is dominated by the pressure (mean stress). To model the spall type failure, void nucleation due to  $F_\epsilon$  in Equation (55) is negligible and in turn, we can set  $F_\epsilon = 0$  in the calculations. Effectively, the void volume fraction model will include only three parameters which can be determined from the plate impact tests data.

Equations (38), (47), (49), (50), and (55) form a set of relationships that has to be solved numerically to describe the stress-strain response of a void contained aggregate material. We developed the corresponding numerical algorithm to describe these equations in the STEALTH finite difference code.

## 4.2 ANALYSES

To describe spallation under a one-dimensional strain impact condition, we modeled a plate impact test #678 in which a 3 mm 1020 steel projectile plate impacts a 6 mm C1008 steel target at a velocity of 178 m/s. We did not consider any void nucleation due to plastic strain. The entire nucleation process was described by the stress threshold based model. The nucleation model parameters that were to be determined were:  $s$ ,  $\sigma_N$ , and  $f_0$ . Since the yield function and the growth law did not contain any model parameters, these are the only three additional parameters that need to be determined to describe the dynamic failure process.

Using the STEALTH code, we modeled the plate impact test, #678. The finite difference simulations of this test with various values for  $f_0$ ,  $\sigma_N$  and  $s$ , failed to generate the observed spall signal. The calculated velocity vs. time (solid line) at the back free surface of the target is shown in Figure 44a. The experimental spall signal (dotted line) could not be simulated. It can be explained by analyzing the calculated stress history in the spall plane as shown in Figure 44b. The points A-E on the stress-time plot correspond to the points A-E on the velocity-time plot. The point A represents the Hugoniot Elastic Limit,  $\sigma_{HEL}$ . At point B, the shock wave reaches its maximum amplitude. The release wave from the flyer unloads in compression at point C and reaches its maximum tensile stress at point D. However, in the stress-time plot, the tensile amplitude (10 kbars) at D is much lower than the shock (compression) amplitude (32 kbar) due to stress relaxation (due to voids nucleation). Note that a value of 20 kbars is assumed for  $\sigma_N$ . Since  $s = 5$ , the nucleation occurs at around 10-15 kbars. Due to void growth, the stress level reduces between the points D and E. This did not produce any spall. Instead, it created a porous material in which the wave speed is small compared to the speed in the intact material. This is the reason for a longer pulse duration under the tensile loading. In the velocity vs. time plot, the spall nucleation can be seen at point D. Since the material in the potential spall plane did not lose its strength entirely, the spall formation is not complete. It is also far below the threshold level and therefore, the velocity continues to decrease between points D and E in Figure 44a.

If we introduce a spall criterion, such as  $\sigma = \sigma_{cr}$  at point D, a spall signal could have been created as shown by the dotted line. However, our objective is to avoid such abrupt failure criterion. Instead we wanted to nucleate and grow voids until the material point loses its strength completely. Theoretically, a value of  $f = 1$  will fail the material completely.

The main problem that we faced with the proposed formulation is due to the growth law. Since, the growth model did not contain any model parameter, the amount of void growth solely depends on

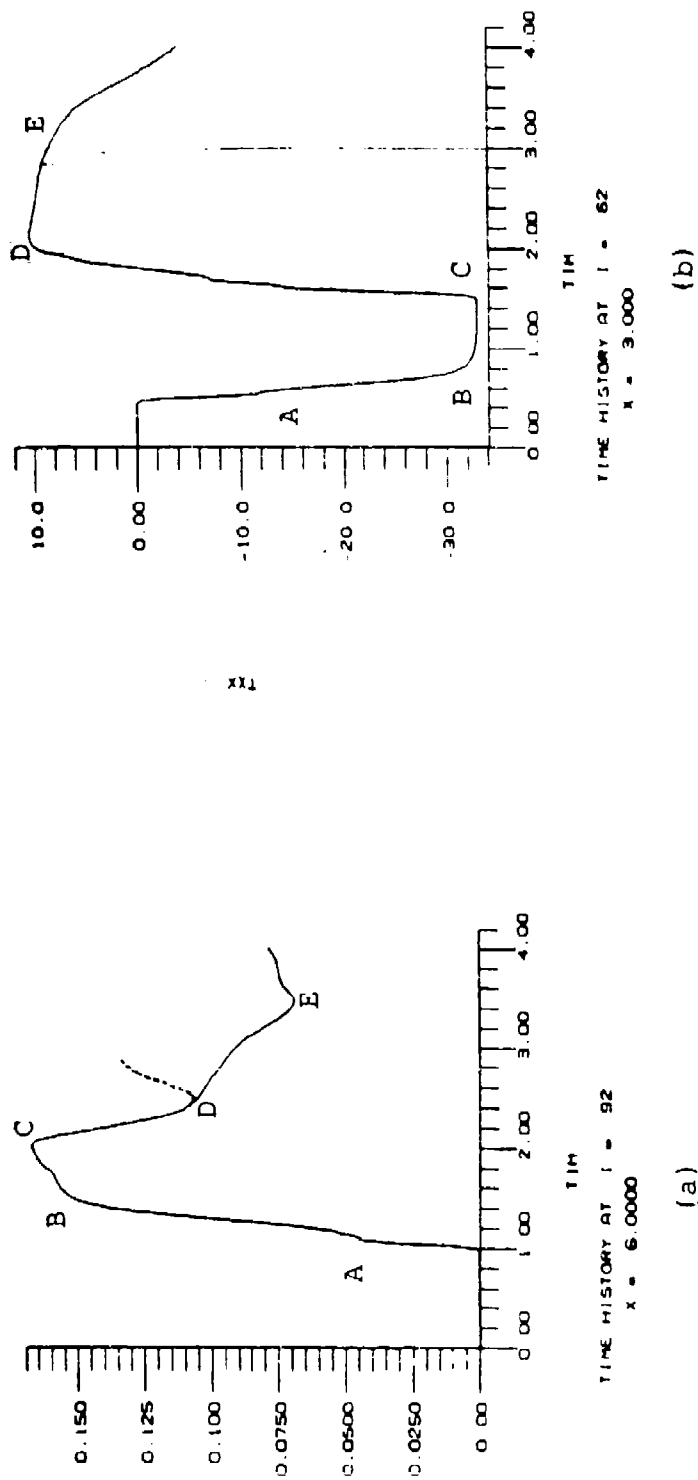


Figure 44. STEALTH Simulation of Test # 678 (a) Velocity vs. Time at the Free Surface and (b) Stress vs. Time at the Spall Plane.

the form of the yield criterion. As we mentioned earlier, the form of  $\delta(\rho)$  in the yield function depends on the material and loading regimes. We decided to modify or introduce a new function for  $\delta(\rho)$ . Any function that describes  $\delta(\rho)$  must satisfy two basic conditions. First, at  $\rho = 1$  (fully dense condition),  $\delta(\rho) = 1$ , and secondly, at  $\rho = \rho_{cr}$ ,  $\delta(\rho) = 0$ , where  $\rho_{cr}$  is a critical value of  $\rho$  at which the material loses its strength completely. Various forms for  $\delta(\rho)$  were considered and the following form was selected after several iterations,

$$\delta(\rho) = e^{-B\left(\frac{1-\rho}{\rho}\right)} \quad (56)$$

where  $B$  is a material parameter. We assumed,  $\rho_{cr} = 0$ , in the above function.

We introduced this equation into the yield function represented by equation (43). Figure 45 shows the effect of  $B$  on the yield function for values of  $\rho = 0.99, 0.85$ , and  $0.75$ . In terms of void volume fraction ( $f = 1 - \rho$ ),  $f = 0.01, 0.15$ , and  $0.25$ . The plots of  $\sqrt{3J_2/Y_m}$  vs.  $P/Y_m$  show that the amount of strength loss due to the presence of voids can be effectively controlled through the parameter,  $B$ .

With the newly introduced function for  $\delta(\rho)$ , the plate impact test on C1008 steel was resimulated. A value of  $0.1$  for  $f_0$  was assumed in our simulations. We chose a standard deviation of  $2$  for  $s$ . A first estimate for  $\sigma_N$  can be made from the experimental velocity vs. time plot. We can assume,

$$\sigma_N = \frac{1}{2} \rho_0 C_0 \Delta V_s \quad (57)$$

where  $\Delta V_s$  is the difference between the measured peak particle velocity and the particle velocity at the spall signal. This is shown in Figure 46.  $\rho_0$  is the material density, and  $C_0$  is the sound speed ( $\sqrt{(K+4/3G)/\rho}$ ). The value of  $B$  was adjusted until the simulated spall signal matched well with the experimental data. Figure 48 compares the model simulated velocity vs. time plot with

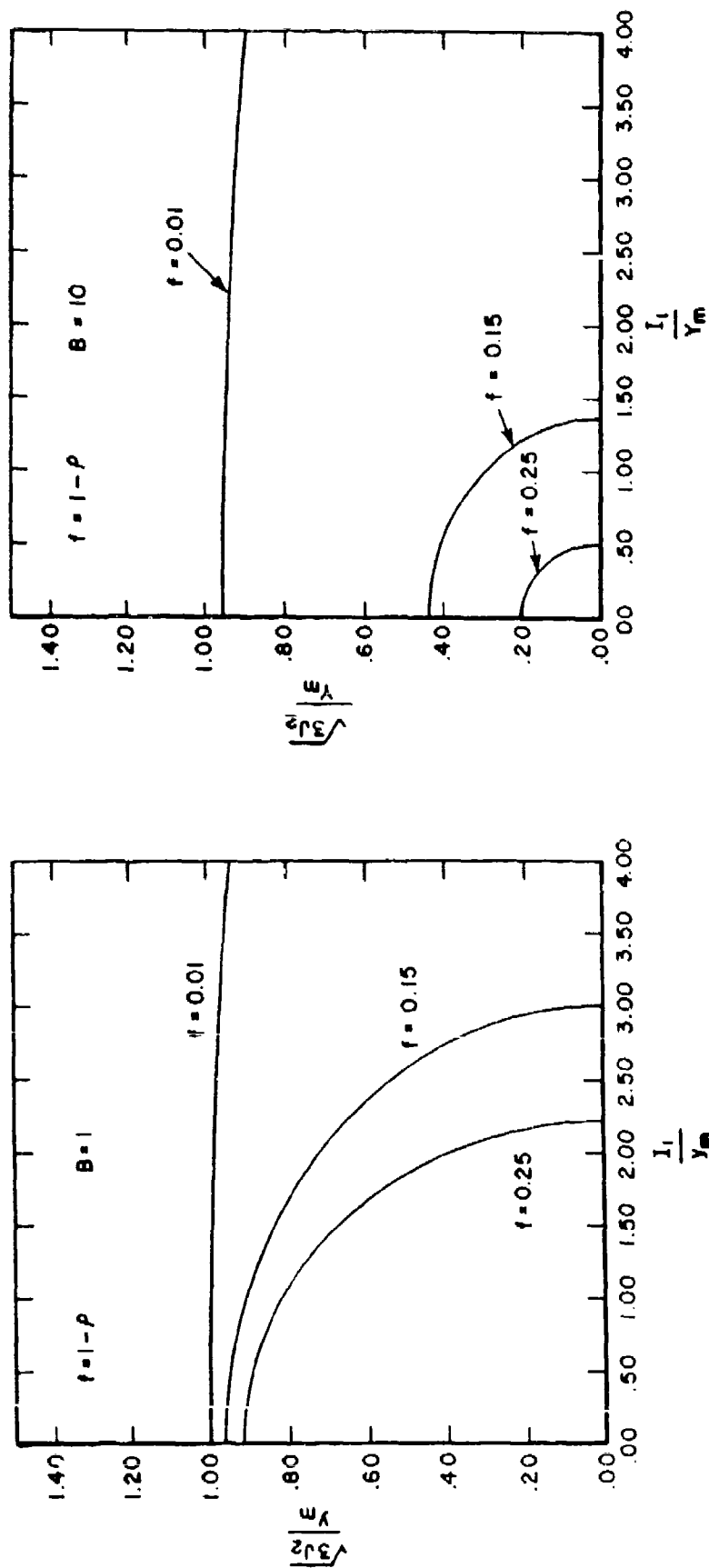


Figure 45. Effect of the Parameter B on the Yield Surfaces.

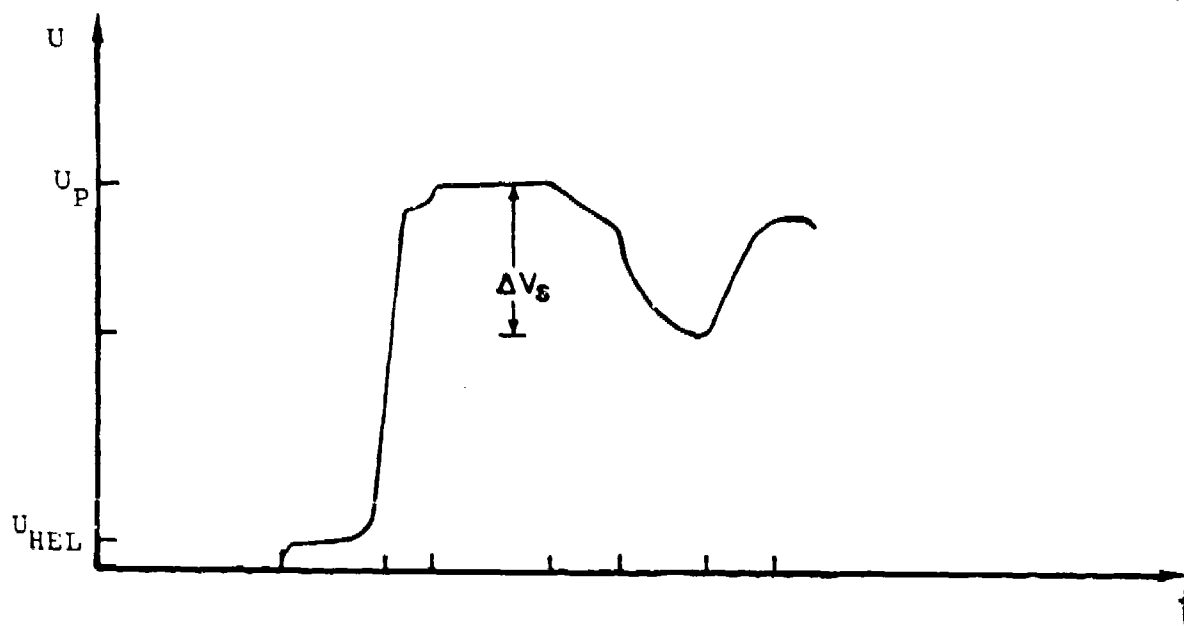


Figure 46. A Typical Spall Signal.

the experimental result. In this simulation, the following values for the model parameters were used:

TABLE 8  
DYNAMIC FAILURE MODEL PARAMETERS

| $D_o$<br>(1/sec) | $n$ | $m$<br>(kbar <sup>-1</sup> ) | $Z_o$<br>(kbar) | $Z_1$<br>(kbar) | $s$<br>(kbar) | $f_o$ | $\sigma_N$<br>(kbar) | $B$ |
|------------------|-----|------------------------------|-----------------|-----------------|---------------|-------|----------------------|-----|
| $10^8$           | 0.4 | 1.5                          | 55              | 70              | 2             | 0.1   | 21.5                 | 20  |

Since the spall signal of test #678 [1] was recorded for a short time duration only, the model simulation was compared only up to point G as shown in Figure 47. The slight kink at point F was due to digitizing of the experimental data. The match between the points A-E was due to the Bodner-Partom model and beyond the point E, it was controlled by the failure model.

To further validate the new model, a plate impact test (#538) in which a copper flyer of 2 mm thick impacted a copper target plate of 9 mm thick at a velocity of 185 m/s was simulated. Using the Bodner-Partom model constants for OFHC copper obtained earlier by Rajendran and Bless [1] and given in Section III of this report, test #538 was simulated. The failure model parameters that could reproduce the experiment are:

| $s$<br>(kbar) | $\sigma_N$<br>(kbar) | $f_o$ | $B$ |
|---------------|----------------------|-------|-----|
| 2             | 16.5                 | 0.05  | 20  |

The velocity vs. time plot obtained using VISAR and the corresponding model simulation plot are shown in Figure 48. Since OFHC copper has a very low value of  $\sigma_{HEL}$  (< 1 kbar), the elastic shock portion of the velocity plot is not well resolved. Beyond the HEL, the simulated plot compared extremely well with the experimental



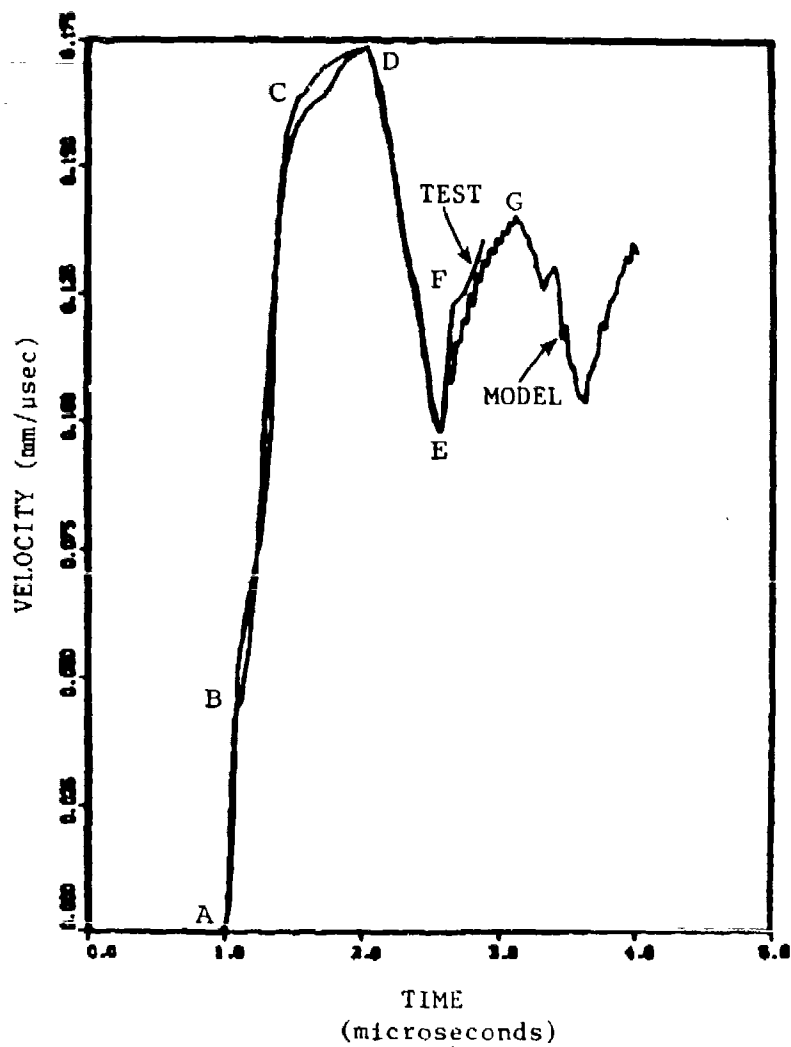


Figure 47. Simulation of Test #678 C1008 Steel Using The Failure Model with New Function for  $\delta(\rho)$ .

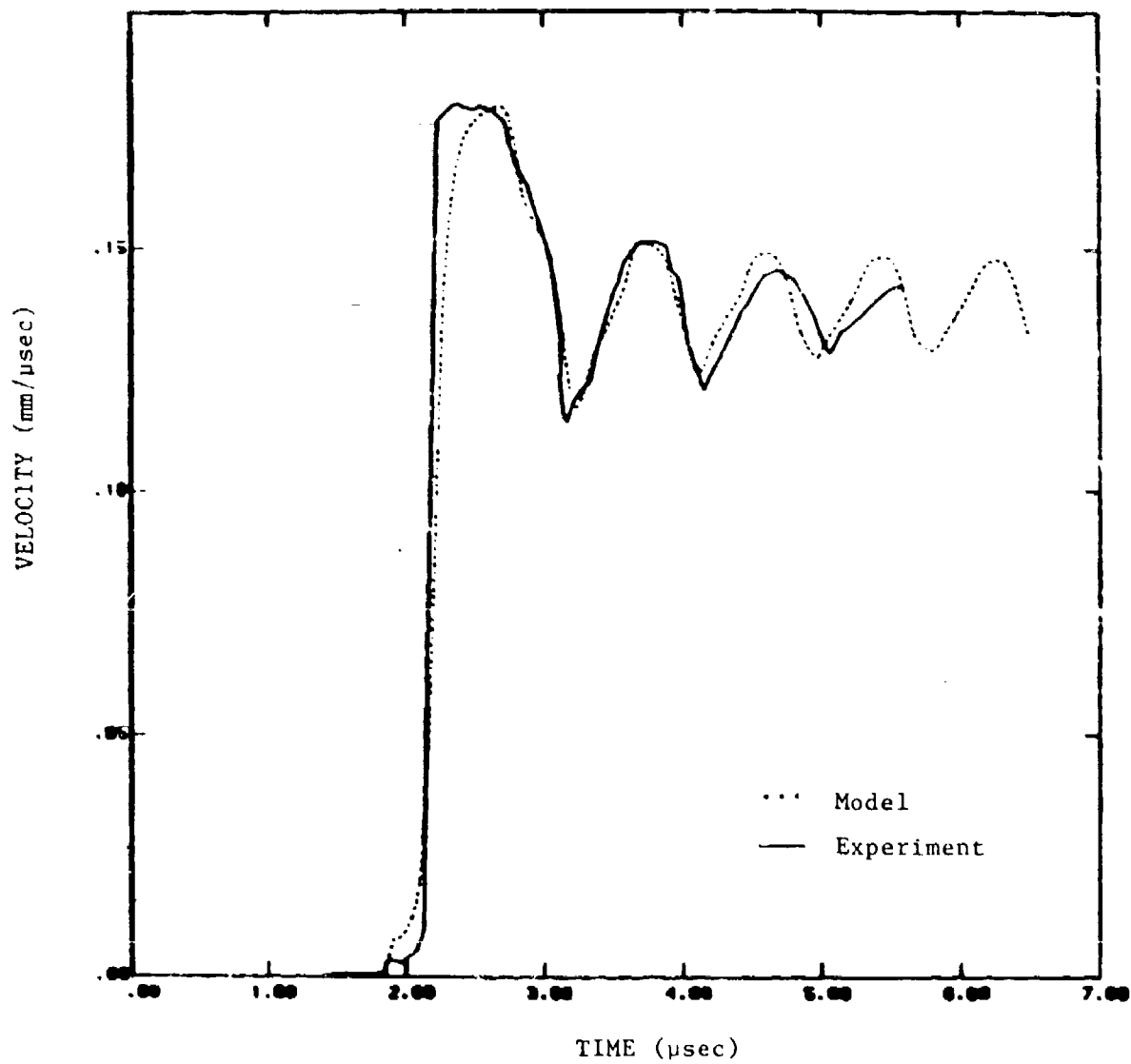


Figure 48. Comparison of Model Simulation with the Experimental Velocity vs. Time Plot for OFHC Copper.

data. But for the slight deviation beyond the second rebound of the spall signal, the velocity vs. time plots compared well.

To demonstrate the ability of the failure model to calculate the stress history at the spall plane, we simulated a plate impact test at different velocities. Various computer runs were made. Figure 49 shows the stress histories at  $V = 75, 100, 150,$  and  $300$  m/s. The assumed model parameters in these runs were,  $s = 1.0$  (kbar)  $\sigma_N = 5.0$  (kbar),  $B = 50.0$ ,  $f_0 = 0.01$ . It can be seen from these figures that the reduction in stress due to void growth increased with increasing velocities (or pressures). From a threshold spall condition at  $V = 75$  m/s, the spall reached a well-above-threshold (excessive spall - the tensile stress relaxed to zero almost instantaneously at  $V = 300$  m/s) condition at a velocity of  $150$  m/s. It is an important feature of this model. The simple failure models, such as a critical stress based model (i.e., failure occurs at  $\sigma = \sigma_{cr}$ ), will not distinguish the difference between above and below threshold spall conditions. Models, in which damage does not degrade the strength (reduction in flow stress), are not capable of modeling the dynamic ductile failure process realistically.

The void volume fraction distribution in the target plan is shown in Figure 50. The flyer plate is between  $x = -3.0$  to  $0$  and the target plate is between  $x = 0$  and  $x = 6$  mm. The void nucleation for low velocity impact is limited to around  $1.75$  mm either side of the spall plane ( $x = 3$  mm). The maximum  $f$  is  $0.0115$ . At higher velocity impacts, the nucleation regions spread more around the spall plane and also the void content,  $f$  increases significantly. For instance, the  $f_{max}$  at  $V = 300$  m/s is several times higher than the  $f_{max}$  at  $V = 75$  m/s. For the same model parameters, a change in the impact velocity showed a physically acceptable changes in the stress history.

We showed that the dynamic failure model, based on void nucleation and growth mechanisms, could model most of the salient features of spall signals obtained from plate impact tests

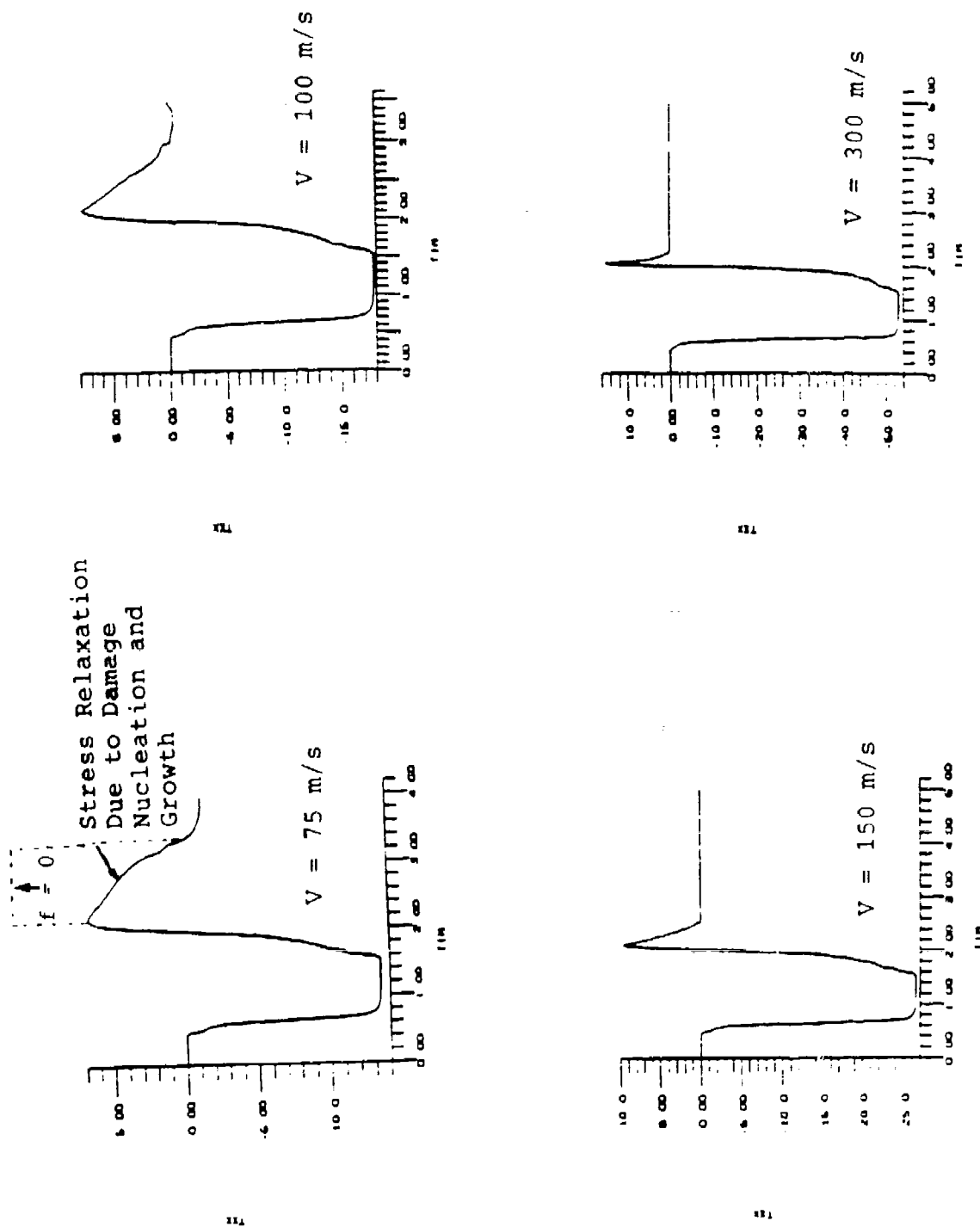
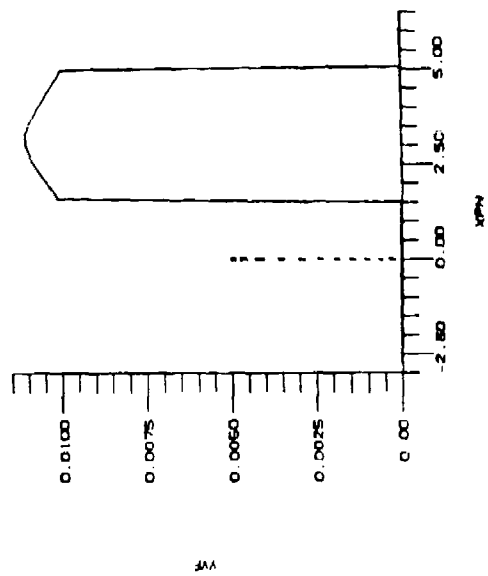
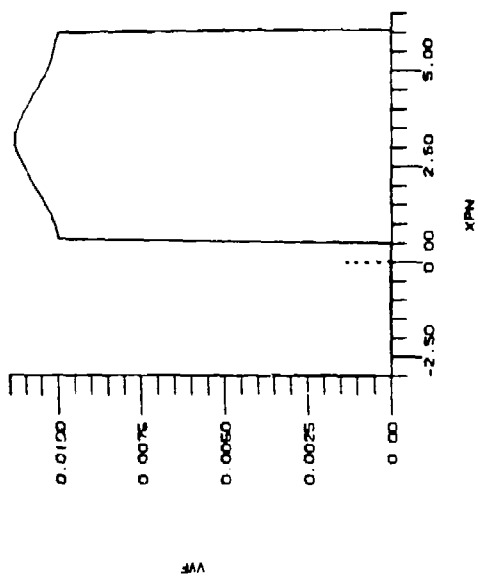


Figure 49. Calculated Stress History at the Spall Plane for Different Impact Velocities.



FLYER ← | → TARGET

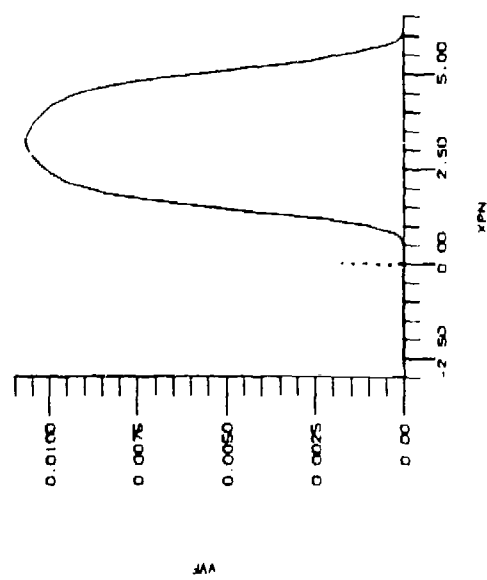
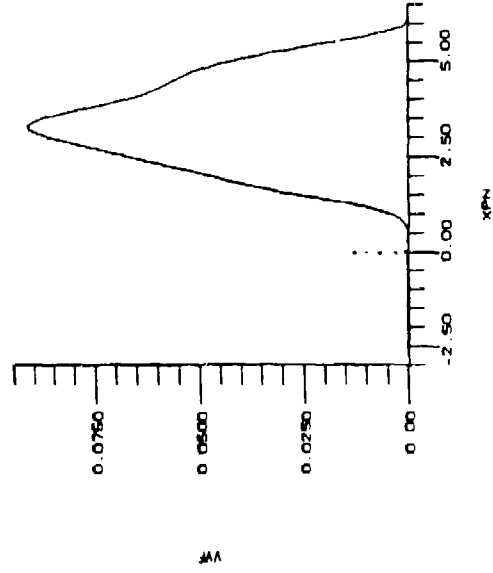


Figure 50. Void Volume Fraction (f) Distribution in the Target Plate at Different Impact Velocities.

reasonably well. We determined the failure model parameters using the VISAR data obtained for C1008 steel and annealed OFHC copper.

## SECTION V

### CONCLUSIONS

#### 5.1 SUMMARY

This report described the high strain rate results for several metals. Data were obtained using (a) the split Hopkinson bar, (b) the long rod impact, and (c) the plate impact tests. Using the induction coil heating technique, stress-strain data at high temperatures were obtained for C1008 steel, Nickel 200, 6061-T6 aluminum, W-2 tungsten, and 52125 steel. The flow stress variation at 10 percent strain with respect to temperature was shown in Figure 3. Several new experimental techniques that were developed for high strain rate measurements are described in this report. Extended details of the new techniques (such as the man-ganin gauge technique, transverse gauges, high pressure measurement) can be found in the cited References 16-30.

We successfully modeled the high strain rate data through the Bodner-Partom model. The B-P model parameters for several metals were presented in Table 7. The spall failure was described by a state-of-the-art failure model. The model was based on microvoid nucleation and growth in materials due to high triaxial tensile stresses. The model contained fewer parameters (only four) than most of the other sophisticated models in which the flow stress was relaxed due to damage. The newly proposed model is continuum mechanics based and is applicable to a general stress state and strain rates. Preliminary model parameters were successfully determined for OFHC copper and C1008 steel.

## 5.2 RECOMMENDATIONS

### 5.2.1 Experiments

Since the exploding wire technique to expand circular thin ring/cylinder geometries is perfected through several improvements in electronics and mechanical design and also can be used routinely, data for several metals must be acquired. The radial expansion of the ring is currently measured using a streak camera - flash lamp optical setup. Preliminary results on 1100-0 aluminum showed a reasonable streak record in which the time scale is well resolved. However, future experiments must consider validating the streak measurements, through the VISAR measurement of the velocity history. The long rod experiments must be conducted on other metals. The strain rates must be varied by performing tests in which the impact face of the rod is conical with the cone angle varying between  $15^{\circ}$ - $60^{\circ}$ .

### 5.2.2 Modeling

The long-rod experiment must be simulated through a two-dimensional finite difference/element code. The validity of the B-P model parameters must be verified. If necessary, the initial yield stress measured from this technique must be included into the B-P model parameter evaluation technique.

The numerical algorithm for the newly developed failure model must be improved. Since the void volume fraction rate increases steeply at the finite difference grid points, it introduces severe constraints on the time step. It was also noticed, that the results from the current numerical scheme seemed to be grid sensitive. These numerical aspects have to be investigated. A well defined failure model parameter evaluation scheme has to be developed. The model must be extended to other metals. The generality of the model parameters must be tested by applying the model to describe failure in other specimen configurations, such as thick cylinders, spall in a right circular conical target impacted by a flyer plate at the base, etc.



## REFERENCES

1. Rajendran, A. M. and Bless, S. J., "High Strain Rate Material Behavior," Report No. AFWAL-TR-85-4009, Wright-Patterson AFB, Ohio, April 1985.
2. Rosenberg, Z., "Analytical Modeling of the Dynamic Response of Piezoresistance Gauges in Shock Wave Experiments," University of Dayton Research Institute, Dayton, OH, UDR-TR-86-104, Aug. 1986.
3. Rosenberg, Z. and Bless, S. J., "Determination of Dynamic Yield Strengths with Embedded Manganin Gauges in Plate-Impact and Long-Rod Experiments," Exp. Mech., Vol. 26, 1986, pp. 279-282.
4. Rosenberg, Z., Dawicke, D., Strader, E., and Bless, S., "A New Technique for Heating Specimens Using Induction-Coil Heaters," Exp. Mech., Vol. 29, No. 3, 1986, pp. 275-278.
5. Nicholas, T., "Tensile Testing of Materials at High Rates of Strain," Exp. Mech., 21, (1981), pp. 177-185.
6. Lindholm, U. S., "Some Experiments with the Split Hopkinson Pressure Bar," J. Mech. Phys. Solids, 12, 1964, pp. 317-335.
7. Cross, L. A., Bless, S. J., Rajendran, A. M., Strader, E. A., and Dawicke, D. S., "New Technique to Investigate Necking in a Tensile Hopkinson Bar," Exp. Mech., Sept. 1984, pp. 184-186.
8. Rajendran, A. M., and Bless, S. J., "Determination of Tensile Stress Beyond Necking at Very High Strain Rate," Exp. Mech., Vol. 26, No. 4, Dec. 1986.
9. Duffy, J., "The Plastic Deformation of Metals-A Review," AFWAL-TR-82-4024, 1982.
10. Bless, S. J., Rajendran, A. M., Dawicke, D. S., and Paisley, D. L., "High Strain Rate Characterization of Materials," AFWAL-TR-83-4038, Aug. 1983.
11. Rosenberg, Z., Mayseless, M., and Partom, Y., "The Use of Manganin Stress Transducers in Impulsively Loaded Long Rod Experiments," J. Appl. Mech., Vol. 51, 1984.
12. Kuschner, G., Hohler, B., and Stilp, A. J., "Non-Linear Propagation of Elasto-Plastic Waves in Rods," 4th APS Topical Conf. on Shock Waves in Condensed Matter, July 1985.
13. Rajendran, A. M. and Fyfe, I. M., "Inertia Effects on the Ductile Failure of Thin Rings," J. of Appl. Mech., Vol. 49, March 1982, p. 31.

14. Karnes, C. H., "The Plate Impact Configuration for Determining Mechanical Properties of Materials at High Strain Rates," in Mechanical Behavior of Materials Under Dynamic Loads, U.S. Lindholm, ed. Springer-Verlag, New York, 1968.
15. Asay, J. R., and Lipkin, J., "A Self Consistent Technique for Estimating the Dynamic Yield Strength of a Shock Loaded Material," J. Appl. Phys., 49, 1978, p. 4242.
16. Rosenberg, Z., "Determination of Dynamic Release Curves of Manganin Stress Gauges from their Resistive Hysteresis," J. Appl. Phys., Vol. 60, 1986, pp. 3369-3371.
17. Rosenberg, Z. and Charest, J., "Accounting for the Response of Dynamically Loaded Annealed Manganin Gauges," J. Appl. Phys., Vol. 60, 1986, pp. 2641-2643.
18. Chen, D. Y., Gupta, Y. M., and Miles, M. H., J. App. Phys, 55, (1984), p. 3984.
19. Partom, Y., Yaziv, D., and Rosenberg, Z., J. App. Phys, 52, (1981), p. 4610.
20. Grady, D. E. and Ginsberg, M. J., J. App. Phys, 48, (1979), p. 2179.
21. Rosenberg, Z, Partom. Y., Mayseless, M., and Falcovitz, J., J. App. Phys., 56, (1984), p. 1434.
22. Barsis, E., Williams, E., and Skoog, C., J. App. Phys., 41, (1970), p. 5155.
23. Rosenberg, Z., Yaziv, D., and Partom, Y., J. Appl. Phys., 51, (1980), p. 3702.
24. Rosenberg, Z. and Partom, Y., "On the Lateral Stress Measurement in Shock Loaded Targets with Transverse Piezoresistance Gauges," Proc. 4th APS Conf. Shock Waves in Condensed Matter, Spokane, WA, July 1985.
25. Gupta, Y. M., J. App Phys., 54, (1983), p. 6256.
26. Rosenberg, Z. and Partom, Y., J. App Phys., 57, (1985), p. 5084.
27. McQueen, R. G and Fritz, J. N., in Proceedings of the AIP Conference, Menlo Park, 1981, pp. 193-207.
28. Rosenberg, Z., "The Use of Manganin Stress Gauges for Determining Release Wave Velocities at High Pressures," Rev. Sci. Instr., 1987.

29. Morris, C. E., Fritz, J. N., and Holian, B. L., in Proceedings of the AIP Conference Menlo Park, 1981, pp. 382-386.
30. Rosenberg, Z. and Bless, S., "On the Possibility of Measuring Shear Waves in Oblique Impact Experiments with In-Material Piezoresistance Gauges," J. Appl. Phys., Vol. 59, 1986, pp. 3928-3930.
31. Chhabildas, L. C. and Swegle, J. W., J. Appl. Phys. 51, (1979), p. 4799.
32. Perzyna, P., "Fundamental Problems in Viscoplasticity," Advances in Applied Mechanics, Vol 9, Academic Press, New York (1966).
33. Malvern, L. E., "The Propagation of Longitudinal Waves of Plastic Deformation in a Bar Exhibiting a Strain-Rate Effect," J. of Applied Mechanics, Trans. ASME, Vol. 18, 1951, p. 203.
34. Bodner, S. R., and Partom, Y., "Constitutive Equations for Elastic-Viscoplastic Strain Hardening Materials," J. Appl. Mech., 42, 1975, pp. 385-389.
35. Bodner, S. R., Partom, I., and Partom, Y., "Uniaxial Cyclic Loading of Elastic-Viscoplastic Materials," ASME Journal of Applied Mechanics, Vol. 46, Dec. 1979, pp. 805-810.
36. Hoffman, R., "STEALTH, Lagrange Explicit Finite-Difference Code for Solids, Structural and Thermohydraulic Analysis," EPRI NP-2080, Nov. 1981.
37. Rajendran, A. M. and Grove, D. J., "Bodner-Partom Viscoplastic Model in STEALTH Finite Difference Code," AFWAL-TR-86-4098, Materials Laboratory, WPAFB, Ohio 45433-6533, Jan 1987.
38. Rajendran, A. M., Bless, S. J., and Dawicke, D.S., "Evaluation of Bodner-Partom Model Parameters at High Strain Rate," J. Eng. Mat. and Tech., 108, 1986, pp. 75-80.
39. Rajendran, A. M. and Geers, E., "BPSOLVE-A Program to Determine Bodner-Partom Model Parameters," UDR-TR-86-95, University of Dayton Research Institute, Dayton, OH, Aug. 1986.
40. Bodner, S. R., "Constitutive Equations for Metals at High Strain Rates," Proceedings, Conference on Fragmentation, Form, and Flow in Fractured Media, (Eds. R. Englmen and Z. Jaeger) Annals of the Israel Physical Society, 1986.
41. Bodner, S. R., and Merzer, A., "Viscoplastic Constitutive Equations for Copper with Strain Rate History and Temperature Effects," ASME Journal of Engineering Materials Technology, Vol. 100, 1978, pp. 388-394.

42. Nicholas, T., Rajendran, A. M., and Grove, D. J., "Analytical Modeling of Precursor Decay in Rate Dependent Materials," to appear in Int. J. of Solids and Structures, 1987.
43. McClintock, F. A., "A Criterion for Ductile Fracture by the Growth of Holes," J. of Applied Mechanics, Vol. 35, (1968), p. 363.
44. Rice, J. R., and Tracey, D. M., "On the Ductile Enlargements of Voids in Triaxial Stress Fields," J. of the Mechanics and Physics of Solids, Vol. 17, 1969, p. 201.
45. Hancock, J. W. and MacKenzie A. C., "On the Mechanisms of Ductile Rupture in High-Strength Steel Subjected to Multi-axial Stress States," J. of Mechanics and Physics of Solids, Vol. 24, (1976), p. 147.
46. Tuler, F. R. and Butcher, B. M., "A Criterion for the Time Dependence of Dynamic Fracture," Int. J. Fracture Mechs., 4, 1968, pp. 431-437.
47. Cochran, S. and Banner, D., "Spall Studies in Uranium," J. of App. Physics, Vol. 48, No. 7, July 1977.
48. Rajendran, A. M., "A Critical Void Growth Failure Criterion Developed for Dynamic and Static Loading Conditions," Doctoral Dissertation, Dept. of Aero and Astro., Univ. of Wash., Seattle, 1980.
49. Davison, L., Stevens, A. L., and Kipp, M. E., "Theory of Spall Damage Accumulation in Ductile Metals," J. Mech. Phys. Solids, Vol. 25, 1977, pp. 11-28.
50. Johnson, J. N., "Dynamic Fracture and Spallation in Ductile Solids," J. Appl. Phys., Vol. 52, No. 4, April 1981, pp. 2812-2825.
51. Meyers, M. A. and Aimone, C. T., "Dynamic Fracture (Spalling) of Metals," Progress in Materials Science, Vol. 28, 1983, pp. 1-96.
52. Curran, D. R., Shockey, D. A., and Seaman, L., "Dynamic Failure in Solids," J. Appl. Phys., Vol. 44, 1973, p. 4025.
53. Argon, A. S., Im, J., and Safoglu, R., "Cavity Formation from Inclusions in Ductile Fracture," Metallurgical Transactions A., Vol. 6A, 1975, p. 825.
54. Gurland, J. and Plateau, J., "The Mechanism of Ductile Rupture of Metals Containing Inclusions," Transactions of the A.S.M., Vol. 56, 1963, p. 443.

55. Doraivelu, S. M., Gegel, H. L., Gunasekara, J. S., Malas, J. C., Morgan, J. T., and Thomas, J. F., "A New Yield Function for Compressible P/M Materials," Int. J. Mech. Sci., Vol. 26, No. 9/10, 1984, pp. 527-535.
56. Chu, C. C. and Needleman, A., "Void Nucleation Effects in Biaxially Stretched Sheets," J. Eng. Mat. Tech., Vol. 102, 1980, pp. 249-256.